Lineare Stabilität der thermokapillaren Strömung in einem Tröpfchen auf einer ebenen temperierten Wand und chaotische Advektion in der überkritischen Strömung

DISSERTATION

zur Erlangung des akademischen Grades

Doktor der Technischen Wissenschaften

eingereicht von

Lukáš Bábor, MSc
Matrikelnummer 11848766

an der Fakultät für Maschinenwesen und Betriebswissenschaften
der Technischen Universität Wien

unter der Leitung von: **Univ.Prof.i.R. Dipl.-Phys. Dr.rer.nat. Hendrik C. Kuhlmann**
Institute für Strömungsmechanik und Wärmeübertragung, E322

Diese Dissertation haben begutachtet:

Prof. Marc Medale, Ph.D.
IUSTI Laboratory, Polytech' Marseille, Aix-Marseille University,
Technopôle de Château-Gombert, 5 rue Enrico Fermi, 13453 Marseille cedex 13, France

Assoc. Prof. Francesco Romanò, Ph.D.
Lille Fluid Mechanics Laboratory, Arts et Métiers,
Av. Paul Langevin, 59650 Villeneuve-d'Ascq, France

Wien, 29. Mai 2023

Lukáš Bábor

Linear stability of the thermocapillary flow in a droplet on a heated wall and chaotic advection in the supercritical flow

DISSERTATION

submitted in partial fulfillment of the requirements for the degree of

Doktor der Technischen Wissenschaften

by

Lukáš Bábor, MSc
Registration Number 11848766

to the Faculty of Mechanical and Industrial Engineering
at the TU Wien

under the supervision of: **Univ.Prof.i.R. Dipl.-Phys. Dr.rer.nat. Hendrik C. Kuhlmann**
Institute of Fluid Mechanics and Heat Transfer, E322

The dissertation has been reviewed by:

Prof. Marc Medale, Ph.D.
IUSTI Laboratory, Polytech' Marseille, Aix-Marseille University,
Technopôle de Château-Gombert, 5 rue Enrico Fermi, 13453 Marseille cedex 13, France

Assoc. Prof. Francesco Romanò, Ph.D.
Lille Fluid Mechanics Laboratory, Arts et Métiers,
Av. Paul Langevin, 59650 Villeneuve-d'Ascq, France

Vienna, 29th May, 2023

Lukáš Bábor

Diese Arbeit wurde von AIC Androsch International Management Consulting GmbH im Rahmen der Forschung auf dem Fachgebiet Strömungsmechanik und Thermodynamik unterstützt.

Ich nehme zur Kenntnis, dass ich zur Drucklegung dieser Arbeit nur mit Bewilligung der Prüfungskommission berechtigt bin.

Eidesstattliche Erklärung

Lukáš Bábor, MSc

Ich erkläre an Eides statt, dass die vorliegende Arbeit nach den anerkannten Grundsätzen für wissenschaftliche Abhandlungen von mir selbstständig erstellt wurde. Alle verwendeten Hilfsmittel, insbesondere die zugrunde gelegte Literatur, sind in dieser Arbeit genannt und aufgelistet. Die aus den Quellen wörtlich entnommenen Stellen, sind als solche kenntlich gemacht.

Das Thema dieser Arbeit wurde von mir bisher weder im In- noch Ausland einer Beurteilerin/einem Beurteiler zur Begutachtung in irgendeiner Form als Prüfungsarbeit vorgelegt. Diese Arbeit stimmt mit der von den Begutachtern beurteilten Arbeit überein.

Ich nehme zur Kenntnis, dass die vorgelegte Arbeit mit geeigneten und dem derzeitigen Stand der Technik entsprechenden Mitteln (Plagiat-Erkennungssoftware) elektronisch-technisch überprüft wird. Dies stellt einerseits sicher, dass bei der Erstellung der vorgelegten Arbeit die hohen Qualitätsvorgaben im Rahmen der geltenden Regeln zur Sicherung guter wissenschaftlicher Praxis "Code of Conduct" an der TU Wien eingehalten wurden. Zum anderen werden durch einen Abgleich mit anderen studentischen Abschlussarbeiten Verletzungen meines persönlichen Urheberrechts vermieden.

Wien, 29. Mai 2023

Lukáš Bábor

Acknowledgements

At this place, I would like to thank Prof. Hendrik C. Kuhlmann for the opportunity to work on the topics presented below under his guidance. Thank you for your professionality and precision and for patiently reminding me of the best practices of scientific writing.

I am grateful to Prof. Wilhelm Schneider for supporting this work and to AIC Androsch International Management Consulting GmbH for partial funding of this thesis.

I also want to thank my colleagues Pierre, Mario, Ariane, Ilya, Dominik M., Dominik K., Javad, Ivo, and Francesca for an excellent atmosphere at our institute. I am grateful to Pierre for sharing his codes with me and for his extensive help setting up the linear stability computations. I also thank Francesco for setting up the computations of the lid-driven cavity flow, Ilya for the consultations of Lagrangian topologies, and Kathy, Birgit, and Christina for their kindness and patience whenever I needed any help with administration.

A special thanks goes to my parents, who have always supported me immensely.

My deepest gratitude goes to my wife Karolína for her care, endless patience and support.

Kurzfassung

Die vorliegende Arbeit ist in drei Teile gegliedert. Im ersten Teil wird die reguläre und chaotische Bewegung von Fluidelementen in einer zweidimensionalen zeitperiodischen Strömung betrachtet. Als Paradebeispiel dient die zweidimensionale Strömung in einem quadratischen Behälter. Die Strömung wird durch einen Deckel angetrieben, der eine harmonische Bewegung mit einem von Null verschiedenem Mittelwert ausführt. Bei einer Erhöhung der mit der Geschwindigkeitsamplitude U gebildeten Reynoldszahl (des Verhältnisses von Trägheits- zu Viskositätskräften $\mathrm{Re} = UL/\nu$, wobei L die Seitenlänge des Behälters und ν die kinematische Viskosität des Fluides sind) wächst der Raumanteil, den chaotische Trajektorien einnehmen. Niedrige Frequenzen (in der Größenordnung von $\mathcal{O}(10^{-2})$) der Deckelbewegung, bezogen auf den Kehrwert U/L der konvektiven Zeitskala, führen zu einer großen Anzahl von langgestreckten Kolmogorov-Arnold-Moser-Tori, deren Struktur sensitiv von der Reynoldszahl abhängt. Für diese Frequenzen entstehen chaotische Trajektorien bei $\mathrm{Re} \sim \mathcal{O}(1)$. Das Gebiet mit chaotischen Trajektorien dehnt sich bei $\mathrm{Re} \sim \mathcal{O}(10)$ auf den größten Teil des Behälters aus. Höhere konvektiv skalierte Frequenzen in der Größenordnung von $\mathcal{O}(1)$ führen hingegen zu einigen wenigen großen KAM-Tori, die nur schwach von der Reynoldszahl abhängen. Chaotischen Trajektorien entstehen in diesem Fall ab $\mathrm{Re} \sim \mathcal{O}(10^2)$. Bei gegebener Reynoldszahl existiert eine bestimmte Frequenz, bei der eine optimale Durchmischung des Fluids erzielt wird. Im Bereich $\mathrm{Re} \in \langle 50, 200 \rangle$ entspricht die optimale Frequenz einer relativen Stokes-Schichtdicke von 0,3 bis 0,4. Im Kontext dieser Arbeit behandelt der erste Teil ein elementares Problem, welches Phänomene veranschaulicht, die das chaotische Mischen in inkompressiblen zeitabhängigen zweidimensionalen Strömungen wie auch in inkompressiblen stationären dreidimensionalen Strömungen bestimmen.

Im zweiten Teil wird die lineare Stabilität der stationären, axisymmetrischen thermokapillaren Strömung in thermokapillaren Tröpfchen mit einer sphärischen Oberfläche untersucht. Die Abhängigkeit der kritischen Reynoldszahl für den Einsatz dreidimensionaler Konvektion vom Kontaktwinkel und von der Prandtlzahl wird berechnet und die Struktur der gefährlichsten Störung wird analysiert. Es werden verschiedene Regime symmetriebrechender Instabilitäten gefunden. Für ein sehr flaches Tröpfchen mit kleinem Kontaktwinkel und hoher Prandtlzahl, das vom Substrat beheizt wird, findet man eine klassische Marangoni-Instabilität nahe der Tröpfchenmitte. Bei einem großen Kontaktwinkel wird die erste Instabilität hingegen durch hydrothermale Wellen (HTW) verursacht. Generell ist die kritische Marangoni-Zahl niedriger, wenn das Tröpfchen von

der Wand beheizt wird als wenn es von der Wand gekühlt wird. Für eine heiße Wand bleibt der hydrothermale Instabilitätsmechanismus sogar bis zu kleinen Prandtlzahlen von $\mathcal{O}(10^{-3})$ dominant. Die kritische Mode und die Struktur des Grundtemperaturfeldes bei der kritischen Marangonizahl unterscheiden sich in den beiden Fällen (heiße/kalte Wand) erheblich. Nur für sehr kleine Prandtlzahlen und große Kontaktwinkel wird eine rein mechanische Instabilität durch Trägheitseffekte beobachtet. In diesem Fall sind die kritischen Parameter und die Struktur der kritischen Mode für kalte und heiße Wände sehr ähnlich.

Schließlich wird im dritten Teil dieser Arbeit die Topologie von Flüssigkeitstrajektorien in einer Modellströmung untersucht, die als lineare Superposition der thermokapillaren Grundströmung mit der kritischen dreidimensionalen Hydrothermalwelle konstruiert wird. Knapp oberhalb der kritischen Schwelle sollte dieses Modell eine gute Näherung der wahren dreidimensionalen Strömung sein, falls die Verzweigung superkritisch ist. Speziell wird der Fall einer beheizter Wand, ein großer Kontaktwinkel und eine hohe Prandtlzahl betrachtet, weil für diese Bedingungen die Bildung von Partikelakkumulationsstrukturen in der Literatur berichtet wurde. Wenn die Stärke der Störströmung circa 10% der Grundströmung beträgt, bilden sich rotierende KAM-Tori nahe der Kontaktlinie und der freien Oberfläche aus. Basierend auf den bekannten Mechanismen der Partikelakkumulation ist zu erwarten, dass sich im Falle einer Suspension aus dichteangepaßten Partikeln mit geringer Konzentration Akkumulationsstrukturen in der Nähe dieser KAM-Tori ausbilden können, wobei Partikel aus dem Gebiet chaotischer Trajektorien durch Kollision mit der Grenzfläche auf den Attraktor transferiert werden.

Abstract

This thesis is divided into three distinct parts. In the first part, the regular and chaotic motion of fluid elements in a two-dimensional time-periodic flow is considered. The two-dimensional flow of an incompressible fluid in a square cavity serves as an excellent example. The flow is driven by a lid that oscillates harmonically in its tangential direction with a zero mean velocity. The emergence and gradual growth of the region occupied by chaotic pathlines upon increasing the Reynolds number (the ratio of the inertial and viscous forces $\mathrm{Re} = UL/\nu$ defined with the velocity amplitude of the lid motion U, the length of the side of the cavity L and the kinematic viscosity of the fluid ν) is resolved. Low frequencies of the lid oscillation (of the order of magnitude $\mathcal{O}(10^{-2})$ relative to the inverse of the convective time-scale U/L) lead to a high number of stretched Kolmogorov–Arnold–Moser tori and high sensitivity to the Reynolds number. For these frequencies, the region occupied by chaotic trajectories (chaotic sea) emerges at $\mathrm{Re} \sim \mathcal{O}(1)$ and spreads to most of the domain at $\mathrm{Re} \sim \mathcal{O}(10)$. On the other hand, higher convective frequencies of the order of 1 lead to a small number of large nested KAM tori and a weak sensitivity to the Reynolds number. The chaotic trajectories then emerge at $\mathrm{Re} \sim \mathcal{O}(10^2)$. An optimal frequency for fast stirring exists for a given Reynolds number. In the range $\mathrm{Re} \in \langle 50, 200\rangle$, the optimal frequency corresponds to the relative Stokes layer thickness of 0.3 to 0.4. In this thesis's overall context, the first part employs the lid-driven cavity flow as a minimalist toy problem illustrating the phenomena that govern stirring in oscillating two-dimensional and steady three-dimensional flows.

The second part investigates the linear stability of the steady axisymmetric thermocapillary flow in a droplet with a spherical free surface adhering to a heated or cooled wall. The dependence of the critical Reynolds number on the contact angle and the Prandtl number is computed, and the structure of the most dangerous perturbation is described. Different regimes of symmetry-breaking instability are observed. For a heated wall, a low contact angle, and a high Prandtl number, the Marangoni instability is observed near the center of the droplet. On the other hand, a hydrothermal wave (HTW) instability is found for high Prandtl number and contact angle. For a hot wall, the critical Marangoni number is lower than for a cold wall, and the thermal instability mechanism remains dominant even down to Prandtl numbers as small as $\mathcal{O}(10^{-3})$. The structures of the basic temperature field and of the most dangerous perturbation differ significantly between the two cases (hot or cold wall). A purely inertial instability is observed in the case of a

vanishing Prandtl number and large contact angle. In that case, the critical parameters and the perturbation structure are quite similar for cold and hot walls.

Finally, the third part of this thesis investigates the topology of fluid trajectories in a model flow constructed as a superposition of the aforementioned basic thermocapillary flow and the most dangerous three-dimensional rotating perturbation mode. The conditions with a heated wall and higher contact angles and Prandtl numbers are considered, for which the formation of particle accumulation structures has been reported in the literature. For the relative magnitude of perturbation of $\mathcal{O}(10\%)$, we find tori approaching close to the free surface near the contact line. Based on the known mechanisms of particle accumulation, it can be expected that in the case of a dilute suspension of density-matched particles, accumulation structures can build near these tori when the collisions of the particles with the free surface transfer them onto the attractor.

Contents

Kurzfassung ix

Abstract xi

Contents xiii

1 General introduction 1
- 1.1 Mixing and stirring . . . 1
- 1.2 Scope of this thesis . . . 2
- 1.3 Mathematical model . . . 2
- 1.4 Numerical methods . . . 3

2 Chaotic advection in a two-dimensional time-periodic lid-driven cavity 9
- 2.1 Introduction . . . 9
- 2.2 Problem formulation . . . 15
- 2.3 Methods of investigation . . . 15
- 2.4 Results . . . 25
- 2.5 Discussion . . . 37

3 Linear stability analysis of thermocapillary convection in droplets adhering to a wall 41
- 3.1 Introduction . . . 41
- 3.2 Problem formulation . . . 47
- 3.3 Numerical solution methods . . . 57
- 3.4 Results . . . 65
- 3.5 Summary . . . 85

4 The onset of chaotic advection in a thermocapillary-driven droplet on a wall 89
- 4.1 Motivation . . . 89
- 4.2 Methodology . . . 90
- 4.3 Results . . . 92
- 4.4 Discussion . . . 100

5 Conclusions **103**

Bibliography **107**

CHAPTER 1

General introduction

1.1 Mixing and stirring

The importance of mixing is obvious[1]. By mixing, we understand the homogenization of concentration of miscible fluids or mechanical emulsification of immiscible liquids. When the fluids are immiscible or their diffusivity is low, it is desirable to promote the mixing by stirring. Stirring is the transport of the fluids by advection, which increases the interface area between them. For weakly diffusive or non-diffusive fluids, the initial mixing stage is dominated by stirring if present. In the case of immiscible fluids, we restrict attention to those with passive interfaces, meaning that the surface tension is too weak to affect the flow. Once the interfacial area is sufficiently large, and at least one of the fluids is stretched into thin filaments, even a weak diffusivity becomes sufficient to homogenize the concentration, or even a weak surface tension is sufficient to atomize the liquid into small droplets.

The most reliable way to achieve a time-efficient stirring is to maximize the Reynolds number to reach a turbulent flow. This is, however, not always possible, for example, when the size of the flow domain is limited (lab-on-chip, e.g. Petkovic et al., 2017) or when the fluid is highly viscous (polymer processing). When such low-Reynolds-number flow is steady and two-dimensional, the stirring is poor as interfacial areas increase only linearly in time. However, if at least one of the translation invariances in the spanwise direction or time breaks, *chaotic advection* can be achieved even in a Stokes flow. The chaotic advection stretches fluid interfaces exponentially, providing an efficient stirring mechanism.

[1] but if in doubt, the reader is referred to the introductions of (Speetjens et al., 2021; Aref et al., 2017; Haller, 2015, and many others)

1.2 Scope of this thesis

This thesis is divided into three parts. In the first part, the emergence of chaotic advection is illustrated numerically in a minimalist setup - the two-dimensional time-periodic lid-driven cavity. In the second part, the transition of a thermocapillary flow in a droplet adhering to a wall from a steady axisymmetric into an oscillating two-dimensional or steady (in a co-rotating reference frame) three-dimensional state is investigated through a linear stability analysis. Such transition is necessary for the onset of chaotic advection, and thus it significantly affects the mixing properties of the flow. The mixing in adhering droplets is of direct practical interest, e.g., in medical diagnosis (Li et al., 2015; Brutin, Sobac, Loquet and Sampol, 2011; Sefiane, 2010). Furthermore, both the two-dimensional oscillating and the three-dimensional steady state admit the existence of specific Lagrangian coherent structures called Kolmogorov–Arnold–Moser tori (as described in the first part), which are the primary candidates for the explanation of the particle accumulation structures (Romanò, Wu and Kuhlmann, 2019) observed in hanging non-isothermal droplets by Takakusagi and Ueno (2017); Watanabe et al. (2018). Thus, the third part of this thesis predicts the structure of the fluid trajectories in conditions comparable to Watanabe et al. (2018). A superposition of the basic flow and the most dangerous three-dimensional rotating perturbation mode is employed as a minimalist model.

1.3 Mathematical model

The flow of an incompressible Newtonian fluid[2] of constant density ρ and dynamic viscosity μ is governed by the famous Navier–Stokes system of equations consisting of the conservation of linear momentum

$$\rho(\partial_{\tilde{t}}\tilde{\boldsymbol{u}} + \tilde{\boldsymbol{u}} \cdot \tilde{\nabla})\tilde{\boldsymbol{u}} = -\tilde{\nabla}\tilde{p} + \mu\tilde{\nabla} \cdot (\underbrace{\tilde{\nabla}\tilde{\boldsymbol{u}} + \tilde{\nabla}\tilde{\boldsymbol{u}}^{\mathrm{T}}}_{\tilde{\boldsymbol{s}}}) + \tilde{\boldsymbol{f}} \tag{1.1a}$$

and conservation of volume

$$\nabla \cdot \tilde{\boldsymbol{u}} = 0 \tag{1.1b}$$

in differential form. $\tilde{\boldsymbol{u}}$ and $\tilde{p}$ are the velocity and pressure field of the fluid, $\nu\tilde{\boldsymbol{s}}$ is the shear stress tensor and $\tilde{\boldsymbol{f}}$ incorporates possible additional bulk forces acting on the fluid as acceleration fields. The validity of the incompressibility constraint (1.1b) requires a small Mach number $\mathrm{Ma}^2 = U^2/c^2 \ll 1$, where U is a characteristic velocity scale of the flow and c is the speed of sound. Using the identity

$$\nabla \cdot (\nabla\tilde{\boldsymbol{u}})^{\mathrm{T}} \equiv \nabla\,(\nabla \cdot \tilde{\boldsymbol{u}}) \overset{(1.1b)}{=\!=} 0 \tag{1.2}$$

[2] This terminology automatically implies the continuum assumption $\mathrm{Kn} \equiv \lambda_{\mathrm{m}}/L \ll 1$, where λ_{m} is the mean free path of molecules and L is the characteristic length of the flow domain. Further common assumptions beyond this level of detail are not explicitly mentioned.

the divergence of the shear-stress tensor in the momentum equation (1.1a) is typically simplified as

$$\tilde{\nabla} \cdot \left(\tilde{\nabla} \tilde{\boldsymbol{u}} + \cancel{\tilde{\nabla} \tilde{\boldsymbol{u}}^{\mathrm{T}}} \right) = \tilde{\nabla}^2 \tilde{\boldsymbol{u}}. \tag{1.3}$$

The system (1.1) is of parabolic type, i.e., its solution on some flow domain Ω requires initial conditions on the entire domain and boundary conditions on the entire boundary $\partial\Omega$. The boundary conditions can in general be prescribed either for the velocity vector $\tilde{\boldsymbol{u}}$, or for the stress vector $\boldsymbol{n} \cdot (\tilde{\boldsymbol{s}} - \tilde{p}\mathbf{I})$ acting on the boundary, where $\boldsymbol{n}$ is the outward-pointing normal. They are typically projected to the normal and tangential directions with respect to the boundary, where different boundary conditions can be prescribed in each of these independent directions.

1.3.1 Scaling

It is advantageous to scale lengths $\boldsymbol{x} = \tilde{\boldsymbol{x}}/L$, velocities $\boldsymbol{u} = \tilde{\boldsymbol{u}}/U$ and time $t = \tilde{t}/t^*$ with some characteristic length L, velocity U and time t^* of the flow problem, in order to obtain a generalizable result. The pressure $p = \tilde{p}/p^*$ is scaled with some convenient factor p^*. Since p^* does not affect the results presented in this thesis, it will not be specified explicitly.

A common approach is to find the representative length and velocity scales L and U of the problem and define the characteristic time scale as their ratio $t^* = L/U$. L is typically determined by a characteristic size of the flow geometry. When the boundary conditions determine a characteristic (maximum or mean) velocity of the flow, it is natural to use this as the velocity scale. Such scaling is called *convective*. The dimensionless momentum equation then reads

$$\partial_t \boldsymbol{u} + (\boldsymbol{u} \cdot \nabla)\boldsymbol{u} = -\nabla p + \frac{1}{\mathrm{Re}} \nabla^2 \boldsymbol{u} + \boldsymbol{f}. \tag{1.4}$$

Alternatively, the velocity scale can be defined as $U = \nu/L$, where $\nu = \mu/\rho$ is the kinematic viscosity, leading to a *viscous* scaling

$$\partial_t \boldsymbol{u} + (\boldsymbol{u} \cdot \nabla)\boldsymbol{u} = -\nabla p + \nabla^2 \boldsymbol{u} + \boldsymbol{f}. \tag{1.5}$$

When a typical time scale of the flow is imposed, for example, by the boundary conditions or by the bulk forces $\tilde{\boldsymbol{f}}$, it may be appropriate to use this to scale time independently of length and velocity. The time derivative term in (1.4) or (1.5) is then multiplied by the Strouhal number $\mathrm{Str} = L/(Ut^*)$ or by the Stokes number $\mathrm{St} = L^2/(\nu t^*)$, respectively.

1.4 Numerical methods

The analytical solution of the Navier–Stokes equations (1.1) is only possible for a few simple flows. Several well-established numerical methods are, however, available. Thus, the flow problems are solved numerically in this thesis. The continuous Galerkin method described below is employed for spatial discretizations throughout this thesis. The particular implementations of this method and other numerical methods applied specifically for a given problem are described in the corresponding chapters.

1.4.1 Nodal continuous Galerkin method

The flow domain Ω is divided into a mesh of finite elements. An approximate numerical solution $\boldsymbol{u}_h, p_h$ of the governing equations is sought in the form

$$\boldsymbol{u}_h(\boldsymbol{x},t) = \sum_{i=1}^{N_u} \boldsymbol{u}_i(t)\phi_i^u(\boldsymbol{x}), \quad p_h(\boldsymbol{x},t) = \sum_{i=1}^{N_p} p_i(t)\phi_i^p(\boldsymbol{x}). \tag{1.6}$$

As the name of the method suggests, the basis functions ϕ_i^u and ϕ_i^p (and thus also the numerical solution) are continuous across Ω. They are constructed with element-wise Lagrange polynomials, such that each function is equal to one at its corresponding grid point, while on all other grid points it vanishes. The unknown coefficients $\boldsymbol{u}_i, p_i$ are the nodal values of the numerical solution. The velocity and pressure are approximated within each element with different polynomial order. Thus, their values can be stored on different nodes.

Next, a system of equations must be obtained to determine the coefficients $\boldsymbol{u}_i, p_i$. To that end, the residual of the momentum and continuity equations is defined. The equations are multiplied, respectively, with test functions $\boldsymbol{v}$ and q from some function spaces $\boldsymbol{V}$ and Q, and integrated over the computational domain Ω

$$\int_\Omega \Big[\rho(\partial_{\tilde{t}} + \boldsymbol{u}_h \cdot \tilde{\nabla})\boldsymbol{u}_h + \tilde{\nabla} p_h - \mu \tilde{\nabla} \cdot \boldsymbol{s}_h\Big] \cdot \boldsymbol{v} \mathrm{d}\Omega = \int_\Omega \rho \tilde{\boldsymbol{f}} \cdot \boldsymbol{v} \mathrm{d}\Omega, \tag{1.7a}$$

$$\int_\Omega (\nabla \cdot \boldsymbol{u}_h)\, q \mathrm{d}\Omega = 0, \tag{1.7b}$$

where $\boldsymbol{s}_h = \tilde{\nabla}\boldsymbol{u}_h + \tilde{\nabla}\boldsymbol{u}_h^{\mathrm{T}}$. For simplification, we define the following notation:

$$\begin{aligned} (\boldsymbol{a},\boldsymbol{b}) &= \int_\Omega \boldsymbol{a}\cdot\boldsymbol{b}\mathrm{d}\Omega, \quad (\boldsymbol{A},\boldsymbol{B}) = \int_\Omega \boldsymbol{A} : \boldsymbol{B}\mathrm{d}\Omega, \\ \langle \boldsymbol{a},\boldsymbol{b}\rangle &= \int_{\partial\Omega} \boldsymbol{a}\cdot\boldsymbol{b}\mathrm{d}S. \end{aligned} \tag{1.8}$$

The viscous dissipation term is integrated *per partes* to eliminate second derivatives, using the product rule

$$\tilde{\nabla}\cdot(\boldsymbol{s}_h\cdot\boldsymbol{v}) = \boldsymbol{s}_h : \tilde{\nabla}\boldsymbol{v} + (\tilde{\nabla}\cdot\boldsymbol{s}_h)\cdot\boldsymbol{v} \tag{1.9}$$

and the Gauss–Ostrogradsky theorem

$$\int_V \tilde{\nabla}\cdot(\boldsymbol{s}_h\cdot\boldsymbol{v})\mathrm{d}V = \int_S (\boldsymbol{s}_h\cdot\boldsymbol{v})\cdot\boldsymbol{n}\mathrm{d}S. \tag{1.10}$$

Furthermore, we use the identity $(\boldsymbol{s}_h\cdot\boldsymbol{v})\cdot\boldsymbol{n} = (\boldsymbol{n}\cdot\boldsymbol{s}_h)\cdot\boldsymbol{v}$. The weak form of the viscous term then reads

$$-\mu\left(\tilde{\nabla}\cdot\boldsymbol{s}_h,\boldsymbol{v}\right) = \mu\left(\boldsymbol{s}_h,\tilde{\nabla}\boldsymbol{v}\right) - \mu\left\langle \boldsymbol{n}\cdot\boldsymbol{s}_h,\boldsymbol{v}\right\rangle. \tag{1.11}$$

The pressure gradient term is integrated *per partes* as well

$$\left(\tilde{\nabla} p_h, \boldsymbol{v}\right) = -\left(p_h, \tilde{\nabla} \cdot \boldsymbol{v}\right) + \langle p_h \boldsymbol{n}, \boldsymbol{v} \rangle \tag{1.12}$$

to bring it to the same form as the continuity equation. The linear combination of both equations defines a scalar expression for the residual of the Navier–Stokes system

$$\mathcal{R} := \rho \left((\partial_{\tilde{t}} + \boldsymbol{u}_h \cdot \tilde{\nabla}) \boldsymbol{u}_h, \boldsymbol{v} \right) + \mu \left(\boldsymbol{s}_h, \tilde{\nabla} \boldsymbol{v} \right) - \left(p_h, \tilde{\nabla} \cdot \boldsymbol{v} \right) - (\nabla \cdot \boldsymbol{u}_h, q) \\ + \langle \boldsymbol{n} \cdot (p_h \mathbf{I} - \boldsymbol{s}_h), \boldsymbol{v} \rangle . \tag{1.13}$$

The formulation of the problem then reads

$$\text{Find } (\boldsymbol{u}_i, p_i) \text{ such that} \qquad \mathcal{R} = 0 \qquad \forall (\boldsymbol{v}, q) \in \boldsymbol{V} \times Q. \tag{1.14}$$

The essence of the Galerkin methods is to use the basis functions as the test functions, $\boldsymbol{V} \ni \boldsymbol{u}_h$ and $Q \ni p_h$. Each test function $\boldsymbol{v}$ then generates the discrete conservation of momentum on the corresponding velocity node, while each q generates the conservation of volume on the corresponding pressure node. The integrals from the inner products (1.8) are expressed numerically based on the nodal values on the given element.

In the case of time-dependent flow problems ($\partial_t \boldsymbol{u} \neq 0$) the resulting system of equations (1.14) still requires numerical discretization in time. A semi-implicit multi-step third-order scheme is employed in chapter 2, as described in section 2.3.6.

Boundary conditions can be imposed in either strong or weak form. Dirichlet boundary conditions for velocity are typically imposed in the strong form - i.e., by modification of the function spaces. The velocity values at the boundary nodes are prescribed. Thus, they do not count as unknowns. Formally we write

$$\boldsymbol{u}_h \in \boldsymbol{V}_b \qquad \text{such that} \qquad \boldsymbol{u}_h = u_{\mathrm{D}} \text{ on } \Gamma_{\mathrm{D}}, \tag{1.15}$$

where $\Gamma_{\mathrm{D}} \subseteq \partial\Omega$ is the part of the boundary where the Dirichlet condition is imposed and $\boldsymbol{V}_b$ is a modified functions space where the Dirichlet condition is satisfied independently of the unknown coefficients $\boldsymbol{u}_i$. The velocity test functions are set to zero on the Dirichlet boundary

$$\boldsymbol{v} \in \boldsymbol{V}_0 \qquad \text{such that} \qquad \boldsymbol{v} = 0 \text{ on } \Gamma_{\mathrm{D}}. \tag{1.16}$$

The boundary integral in (1.13) then vanishes on Γ_{D}. Dirichlet boundary conditions for pressure can be imposed in the same way.

On the other hand, a prescribed boundary stress

$$\boldsymbol{n} \cdot (p_h \mathbf{I} - \boldsymbol{s}_h) = \boldsymbol{g}_{\mathrm{N}} \qquad \text{on } \Gamma_{\mathrm{N}} \tag{1.17}$$

is typically imposed in the weak form. The prescribed stress vector acting on those faces of finite elements which belong to Γ_{N} is substituted directly into the boundary integral, while no modifications of the functions spaces are needed on Γ_N. This thesis does not employ other boundary conditions (e.g., Robin or periodic).

The strong boundary condition can also be imposed for selected components of the velocity vector. The boundary stress is then imposed only in the remaining coordinate directions. The division of the boundary $\partial\Omega$ into Γ_D and Γ_N can therefore differ for each field variable (velocity components and pressure), but it must always hold

$$\Gamma_\mathrm{D} \cup \Gamma_\mathrm{N} = \partial\Omega \qquad \wedge \qquad \Gamma_\mathrm{D} \cap \Gamma_\mathrm{N} = \emptyset. \tag{1.18}$$

Alternatively, the boundary integral can be projected to arbitrary perpendicular directions (typically normal and tangential to the boundary), in which independent boundary conditions can be imposed.

1.4.2 Newton–Raphson method

For steady flow problems ($\partial_t \boldsymbol{u} = 0$, as in chapters 3 and 4), (1.14) leads to a system of non-linear algebraic equations

$$\boldsymbol{\mathcal{R}}(\boldsymbol{q}_0) \stackrel{!}{=} 0 \tag{1.19}$$

for the vector of nodal values $\boldsymbol{q}_0 = (\boldsymbol{u}_i, p_i)$. This is solved iteratively with the Newton–Raphson method (algorithm 1.1). The method is also employed in chapter 2 for finding closed fluid trajectories in the time-dependent flow, as described in section 2.3.2. The concept of the method is briefly presented below for completeness. Some readers might prefer to skip the rest of this section.

Algorithm 1.1: The Newton–Raphson method for the iterative solution of a system of non-linear algebraic equations

Data: initial guess for $\boldsymbol{q}_0$
Result: $\boldsymbol{q}_0$ such that $\|\boldsymbol{\mathcal{R}}(\boldsymbol{q}_0)\| \leq$ tolerance

```
while ‖𝓡(q0)‖ > tolerance do
    compute Jacobian matrix A_ij ← ∂_{q0,j} 𝓡_i(q0) ;
    q0 ← q0 − A^{-1} 𝓡(q0) ;
end
return q0
```

The method can be derived from the Taylor expansion

$$\boldsymbol{\mathcal{R}}\left(\boldsymbol{q}_0^{(k)} + \boldsymbol{\delta q}\right) = \boldsymbol{\mathcal{R}}\left(\boldsymbol{q}_0^{(k)}\right) + \nabla\boldsymbol{\mathcal{R}}\left(\boldsymbol{q}_0^{(k)}\right) \cdot \boldsymbol{\delta q} + \mathcal{O}\left(\boldsymbol{\delta q}^2\right) \tag{1.20}$$

of the non-linear vector function $\boldsymbol{\mathcal{R}}(\boldsymbol{q}_0)$ about an initial guess for $\boldsymbol{q}_0$. The correction $\boldsymbol{\delta q}$ of the initial guess $\boldsymbol{q}_0^{(k)}$ is sought such that

$$\boldsymbol{\mathcal{R}}\left(\boldsymbol{q}_0^{(k)} + \boldsymbol{\delta q}\right) \stackrel{!}{=} 0. \tag{1.21}$$

An assumption is made that between the initial guess and the solution of (1.19), the function $\boldsymbol{\mathcal{R}}$ is approximated sufficiently well with linear dependence. Under this assumption the higher order terms $\mathcal{O}\left(\boldsymbol{\delta q}^2\right)$ are neglected, which corresponds to linearization of the problem (1.21) about the initial guess

$$\boldsymbol{\mathcal{R}}\left(\boldsymbol{q}_0^{(k)}+\boldsymbol{\delta q}\right) \approx \boldsymbol{\mathcal{R}}\left(\boldsymbol{q}_0^{(k)}\right)+\nabla\boldsymbol{\mathcal{R}}\left(\boldsymbol{q}_0^{(k)}\right)\cdot\boldsymbol{\delta q} \stackrel{!}{=} 0. \tag{1.22}$$

The linearized problem is then solved for the correction

$$\boldsymbol{\delta q} = -\left[\nabla\boldsymbol{\mathcal{R}}\left(\boldsymbol{q}_0^{(k)}\right)\right]^{-1}\cdot\boldsymbol{\mathcal{R}}\left(\boldsymbol{q}_0^{(k)}\right), \tag{1.23}$$

and a new approximation of the solution is obtained as

$$\boldsymbol{q}_0^{(k+1)} = \boldsymbol{q}_0^{(k)} + \boldsymbol{\delta q}. \tag{1.24}$$

The more non-linear the system (1.19) is, the closer should the initial guess be to its solution in order to satisfy the underlying assumption of the method. Therefore, for a given geometry, we typically first compute a low-Reynolds-number flow, using a zero vector as an initial guess. Since low-Reynolds-number flows are dominated by the linear terms of the Navier–Stokes equations, an arbitrary initial guess is usually good enough for convergence. The solution is then used as an initial guess for the computation of flows at higher Reynolds numbers.

CHAPTER 2

Chaotic advection in a two-dimensional time-periodic lid-driven cavity

The results presented in this chapter have been published in:
Babor, L. and Kuhlmann, H. C. (2023a), 'Lagrangian transport in the time-periodic two-dimensional lid-driven square cavity', *Phys. Fluids* **35**, 033611 (21pp).

2.1 Introduction

2.1.1 Lid-driven cavity flow

A lid-driven cavity is a closed box where at least one of the walls (the lid) slides tangentially (fig. 2.1). Such sliding lid can be realized, for example, by a belt, or it can be approximated for laboratory purposes by a rotating cylinder with a sufficiently large radius. The motion of the lid drives a flow inside the cavity. If the cavity is elongated in the direction normal to the lid's motion, then in the central section of the cavity, the effect of the front and the back wall diminishes, and the flow is two-dimensional up to a certain Reynolds number.

The lid-driven cavity flow is a classical benchmark in computational fluid mechanics thanks to the simplicity of the geometry. Furthermore, it is a convenient setup for the investigation of several fundamental fluid-dynamics phenomena as, e.g., the centrifugal instability (Albensoeder et al., 2001*b*; Kuhlmann and Albensoeder, 2014, and others), multiplicity of states (Albensoeder et al., 2001*a*), an infinite sequence of corner vortices (Moffatt, 2019, 1964; Kalita et al., 2018) and chaotic advection (Romanò et al., 2020) to

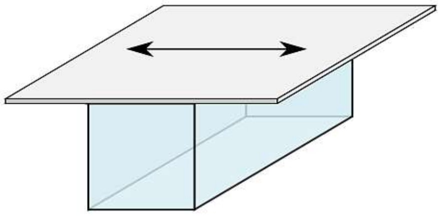

Figure 2.1: Illustration of a lid-driven cavity

name a few (see Shankar and Deshpande, 2000; Kuhlmann and Romanò, 2018, for an extensive review).

When the velocity of the lid is modulated harmonically in time, an oscillatory boundary layer appears near the lid, as in the second problem of Stokes. In the limit of an infinitely wide[1] cavity, the oscillatory flow consists of a Stokes layer near the lid and a pressure-driven flow in the rest of the cavity due to conservation of volume (O'Brien, 1975). The thickness of the Stokes layer λ scales as $L\mathrm{St}^{-1/2}$, where the Stokes number $\mathrm{St} = L^2/(\nu T)$, L is the height of the cavity, ν the kinematic viscosity and T the period of oscillation. When the relative thickness of the Stokes layer $\lambda/L \ll 1$ is small, it is pronounced even in cavities with a finite width-to-height ratio. A detailed description of the instantaneous flow in a cavity with a width-to-height ratio of 2 driven by a harmonic motion of a single lid is due to Zhu et al. (2020).

2.1.2 Chaotic advection

The term *chaotic advection* has been introduced by Aref (1984). He shows that the trajectories of infinitesimal fluid elements in two-dimensional time-periodic closed laminar flows can be either regular or chaotic (see fig. 2.2 for illustration). Regular trajectories, also called *integrable*, can be qualitatively described over an unbounded time interval with a function employing a finite number of constants. For example, the trajectories in steady two-dimensional flows are always regular. The chaotic trajectories, on the other hand, are characterized by a positive Lyapunov exponent

$$\sigma(\boldsymbol{X}, \boldsymbol{M}) = \lim_{\substack{t\to\infty \\ |\mathrm{d}\boldsymbol{X}|\to 0}} \left[\frac{1}{t} \ln\left(\frac{|\mathrm{d}\boldsymbol{x}|}{|\mathrm{d}\boldsymbol{X}|}\right)\right], \tag{2.1}$$

which is the exponential stretching rate of an infinitesimal line segment $\mathrm{d}\boldsymbol{X}$ with an initial orientation $\boldsymbol{M} = \mathrm{d}\boldsymbol{X}/|\mathrm{d}\boldsymbol{X}|$ advected along the trajectory from an initial location $\boldsymbol{X}$. $|\mathrm{d}\boldsymbol{x}|$ is the length of the segment at time t. The Lyapunov exponent quantifies the sensitivity of a trajectory to the initial condition $\boldsymbol{X}$.

[1] In the absence of buoyancy, it is a standard convention to consider the lid as the top boundary. The width and height are then the extents of the cavity in the direction parallel and perpendicular to the lid, respectively.

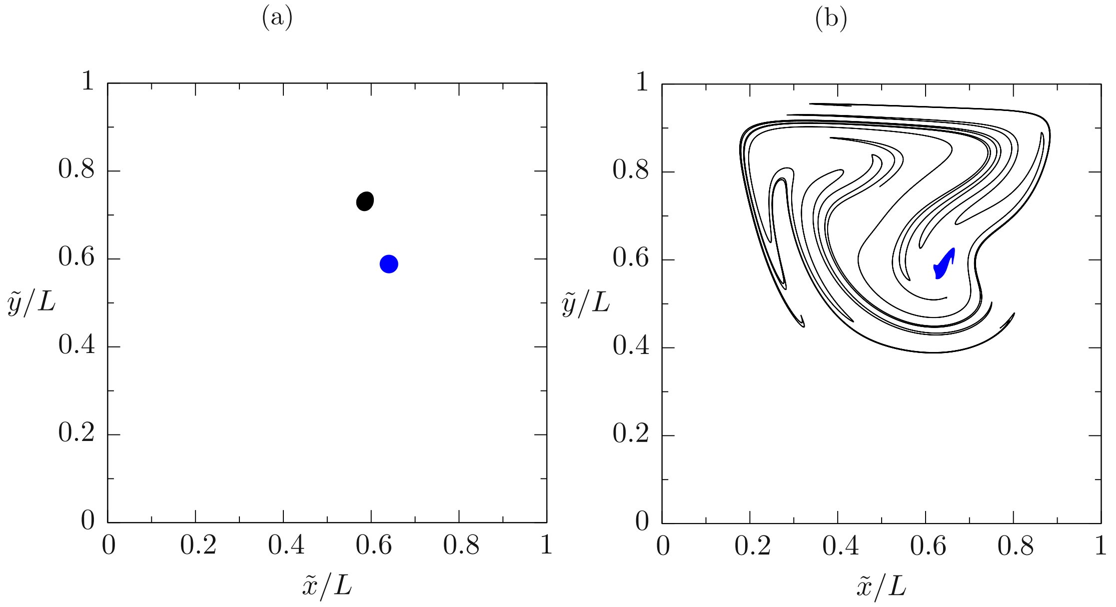

Figure 2.2: Illustration of advection of two different blobs of marked fluid in a two-dimensional time-periodic lid-driven cavity. (a) shows the initial state where two blobs in different locations in the cavity are marked by black and blue color. (b) shows the final shape of the colored portions of fluid after some natural number of periods of the flow. The black portion of fluid is located in a region of chaotic trajectories, while the blue fluid is located in a region of regular trajectories.

The possibility of the co-existence of regular and chaotic trajectories can be deduced by an inspection of the advection equation

$$\frac{\mathrm{d}\tilde{\boldsymbol{x}}}{\mathrm{d}\tilde{t}} = \tilde{\boldsymbol{u}}(\tilde{\boldsymbol{x}}, \tilde{t}). \tag{2.2}$$

In the case of an incompressible two-dimensional flow, a stream function can be defined as

$$\tilde{\boldsymbol{u}} = \begin{pmatrix} \partial\psi/\partial\tilde{y} \\ -\partial\psi/\partial\tilde{x} \end{pmatrix}. \tag{2.3}$$

Substitution of (2.3) in (2.2) yields a Hamiltonian dynamical system where the stream function ψ is the Hamiltonian and the spatial coordinates $\tilde{x}$ and $\tilde{y}$ take the role of the generalized position and momentum. The fluid trajectories are thus equivalent to trajectories in a phase space of the Hamiltonian system, and the well-established Hamiltonian dynamics apply. For a steady flow $\psi = \psi(\tilde{x}, \tilde{y})$, the system has 1 degree of freedom since the Hamiltonian depends on 1 "position" and 1 "momentum", which are not independent (analogously to the most famous Hamiltonian system - the frictionless pendulum). Thus, only regular trajectories are allowed. Time dependence of the Hamiltonian $\psi = \psi(\tilde{x}, \tilde{y}, \tilde{t})$ adds an additional half degree of freedom, admitting the existence of chaotic trajectories.

Of particular relevance are the time-periodic flows $\psi(\tilde{x}, \tilde{y}, \tilde{t}) = \psi(\tilde{x}, \tilde{y}, \tilde{t} + T)$, where T is the period. In order to relate the advection to the Hamiltonian dynamics, it is common to understand time as an azimuthal coordinate (fig. 2.3) by mapping the time interval of one period $[0, T]$ to the azimuthal interval $[0, 2\pi]$. In this viewpoint, the dynamics are generalizable to steady three-dimensional flows.

Regular trajectories lie on Kolmogorov–Arnold–Moser (KAM) tori. In the case of a steady two-dimensional flow, the tori coincide with the streamlines extended in time. The mapping between the time and the azimuthal angle is arbitrary in this case. All trajectories in such flow are regular since all fluid elements move along streamlines. The tori form dense nested sets, as each vortex in the flow corresponds to a dense set of nested streamlines. A common center of each set of tori is a closed elliptic trajectory, which in this analogy corresponds to a center of a steady two-dimensional vortex. When the flow becomes time-periodic or three-dimensional, some of the tori can remain, but in the former case, they no longer coincide with the instantaneous streamlines.

Chaotic trajectories fill the remaining space between the KAM tori. They typically emerge from a homoclinic or heteroclinic connection - a set of hypothetical trajectories[2] which separate different sets of tori and connect either two different hyperbolic trajectories (heteroclinic connection) or a single hyperbolic trajectory with itself forming a closed loop (homoclinic connection). When such connection is perturbed by the time-dependence or three-dimensionality of the flow, the set of pathlines leaving a hyperbolic trajectory along one of its most-repelling directions (unstable manifold) no longer coincides with the set of pathlines approaching either the same or another hyperbolic trajectory along one of its most-attracting directions (stable manifold). Instead, the stable and unstable manifolds intersect transversally, which is one of the signatures of chaos. The perturbed unstable manifold folds as it approaches the (other) hyperbolic trajectory along the stable manifold. The folds are stretched along both unstable manifolds (of the latter trajectory) until they return to their original trajectory, where they are folded and stretched again by the same mechanism. This way, the perturbed unstable manifolds are repeatedly stretched and folded, which leads to an exponential growth of their area. The reader is referred to the book of Ottino (1989) for excellent illustrations.

The type of a closed trajectory (elliptic/parabolic/hyperbolic) is defined by the behavior of trajectories in its close vicinity, as already follows from the previous paragraphs. Elliptic trajectories are Lyapunov stable. This means that trajectories near the elliptic trajectory remain in its neighborhood for all times. They orbit about it. On the other hand, hyperbolic trajectories are characterized by the stable and unstable manifolds. These are curves or surfaces (in 2D or 3D, respectively) along which the nearby trajectories exponentially approach or depart from the hyperbolic trajectory. In the case of the parabolic type, the distance of the nearby trajectories from the closed trajectory depends linearly on time. A mathematical criterion for classification of the type of a closed trajectory is provided in section 2.3.2.

[2] Such separation trajectory cannot be observed in its entirety since it takes an infinitely long time to approach a hyperbolic trajectory along its stable manifold

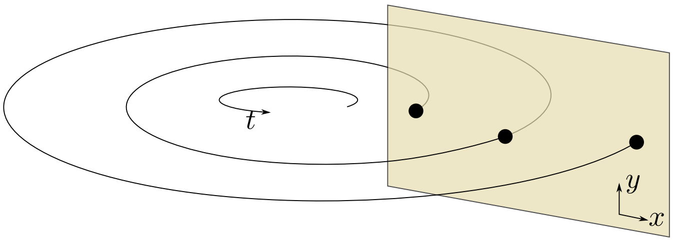

Figure 2.3: The stroboscopic projection of fluid trajectories in a two-dimensional flow illustrated in a figurative cylindrical coordinate system, where a radial and axial coordinate represent the two spatial dimensions x and y of the flow, and the time is mapped to the azimuthal coordinate. The stroboscopic projection plane is shown in yellow. The black spiral curve illustrates a fluid trajectory, and the black dots represent the intersections of the trajectory with the projection plane.

The regular and chaotic trajectories can be distinguished using a Poincaré section. Poincaré section is a plane in the parameter space of a Hamiltonian system that is periodically intersected by the trajectories, where the positions of the intersection points are recorded. In the case of a time-periodic flow, the Poincaré section is equivalent to a stroboscopic projection (fig. 2.3) where the period of strobing is (a natural multiple of) the period of the flow. The intersections of regular trajectories with the Poincaré plane outline closed curves, which are the intersections of their parent tori with the plane. The intersections of chaotic trajectories are chaotically distributed within the region between the KAM tori, often called the *chaotic sea*.

The KAM tori are specific cases of Lagrangian coherent structures - barriers of convective material transport. The fluid inside a torus cannot exchange with the fluid outside the torus except through molecular diffusion. The tori can deform as they are advected by the flow, but their intersections with the Poincare plane recover the initial shape and position after $n \in N$ periods of the flow (or n revolutions about the axis of the torus in case of a steady three-dimensional flow). n is called the periodicity of the torus.

Regular trajectories wind about the centerlines of KAM tori. The winding time τ_{w} describes the duration of one winding with respect to the period of the torus nT. When the winding time is rational, i.e., $\tau_{\mathrm{w}} = p/q$ and $(p, q \in \mathbb{N})$, all trajectories on the torus are closed (of parabolic type) and each intersects the Poincaré plane at p distinct points. Tori consisting of closed trajectories are called *resonant*. On the other hand, trajectories with irrational τ_{w} are not closed, and their intersections with the Poincaré plane cover the outline of their parent torus densely. The Kolmogorov–Arnold–Moser theorem (Kolmogorov, 1954*b*,*a*; Arnold, 1963; Möser, 1962; Rüssmann, 1970) claims that the non-resonant tori survive a perturbation of the Hamiltonian system. The Poincaré–Birkhoff theorem (Birkhoff, 1934; Helleman, 1980) explains that resonant tori tend to break into sub-harmonic tori around one of the parabolic closed trajectories with periodicity pnT. The closed trajectory thus becomes elliptic. Furthermore, a hyperbolic trajectory is created with heteroclinic connections separating different parts of the subharmonic torus from the non-resonant tori of period nT. A layer of chaotic trajectories bounded by two nested tori can emerge from these heteroclinic connections.

When the winding time infinitely close to the closed trajectory at the center of the tori becomes rational, the trajectory itself is called resonant. This occurs, for example, when different sections of a subharmonic torus approach the closed trajectory of lower periodicity between them and eventually touch it. The closed trajectory then changes type from elliptic to hyperbolic. When the different sections of the subharmonic torus merge into a single torus of lower periodicity, the central closed trajectory changes type back to elliptic. Such resonances of closed trajectories were observed, for example, in two-dimensional lid-driven cavity flow with a non-zero mean velocity of the lid oscillation (Poumaëre, 2020), or in a steady three-dimensional cavity (Ishii et al., 2012).

2.1.3 Historical context

Low-Reynolds-number ($\lesssim \mathcal{O}(1)$) flows in cavities driven by two opposing walls have been extensively investigated in terms of the topology of fluid trajectories, for example by Chien et al. (1986); Ottino et al. (1988); Leong and Ottino (1989); Franjione et al. (1989). They consider the effect of the temporal driving protocols of the lids. The mean velocities of the lids are typically non-zero. In such conditions, there is a net advection even at Stokes flow. For specific driving protocols Leong and Ottino (1989) observe that a larger distance (relative to the cavity size) traveled by the lid per period of the flow favors the chaotic advection. Also, they show that when the time dependence of the velocity of both lids is even symmetric about some instances in time, the locations of fluid elements which follow closed trajectories tend to organize at these time instances into some pattern that inherits symmetries from the instantaneous streamlines of the flow.

Takasaki et al. (1994) and Anderson et al. (2000) consider cavities driven by a harmonic motion with a non-zero mean velocity of a single lid at Reynolds numbers of $\mathcal{O}(10)$. Takasaki et al. (1994) find an optimal dimensionless frequency (in convective scaling) of the lid oscillation for efficient stirring in the range $[0.7, 1]$ within the investigated Reynolds numbers and ratios of the oscillation amplitude to the mean component of the lid velocity. Anderson et al. (2000) find a KAM torus of period one near the center of the instantaneous Eulerian vortex orbited by a subharmonic torus of period three for the dimensionless frequency of 0.67 and the Reynolds number based on the mean velocity component of 50. These regular tori almost completely vanish in the sea of chaotic trajectories when the Reynolds number based on the amplitude of the lid velocity oscillation increases from 25 to 75. Furthermore, they investigate the effect of a small, steady motion of the bottom wall (the one opposing the lid). When the bottom wall moves in the opposite direction than the mean velocity of the lid, a layer of regular trajectories near the bottom wall is eliminated, but the size of the KAM tori in the bulk of the cavity increases. Also, the structure of the KAM tori then becomes more complex for some parameters. On the other hand, when the bottom wall moves in the same direction as the average motion of the lid, the region of regular trajectories near the bottom wall extends. Subharmonic tori of several periodicities are observed in this region.

Most studies above consider driving with a non-zero mean velocity and low Reynolds number. This chapter investigates fluid transport in a cavity flow driven by a single lid with zero mean velocity. This setup is more practical as the lid can be realized by a solid plane wall with linear driving. However, any net advection relies on fluid inertia, and thus a higher Reynolds number is required.

2.2 Problem formulation

We consider the flow inside a two-dimensional square cavity (fig. 2.4) of side length L, driven by a harmonic tangential oscillation of a single lid with velocity amplitude U and period of oscillation T. Scaling the lengths, velocities, and time by L, U, and T respectively, the dimensionless form

$$\mathrm{Str}\frac{\partial \boldsymbol{u}}{\partial t} + \boldsymbol{u}\cdot\nabla\boldsymbol{u} = -\nabla p + \frac{1}{\mathrm{Re}}\nabla^2\boldsymbol{u}, \tag{2.4a}$$

$$\nabla\cdot\boldsymbol{u} = 0. \tag{2.4b}$$

of the governing equations (1.1) is obtained. The solution of (2.4) is required to satisfy the boundary conditions

$$\boldsymbol{u}(x = \pm 1/2) = 0, \tag{2.5a}$$

$$\boldsymbol{u}(y = -1/2) = 0, \tag{2.5b}$$

$$\boldsymbol{u}(y = 1/2) = \cos(2\pi t)\boldsymbol{e}_x. \tag{2.5c}$$

on the domain $\Omega = [-0.5, 0.5] \times [-0.5, 0.5]$. A fully developed time-periodic flow is considered, i.e., after the effect of the initial condition vanishes. The two independent dimensionless parameters governing the problem are the Reynolds number $\mathrm{Re} = LU/\nu$ and the Strouhal number $\mathrm{Str} = L/(UT)$ which quantifies the oscillation frequency with respect to the convective time scale. Alternatively, the Stokes number $\mathrm{St} = \mathrm{ReStr} = L^2/(\nu T)$ may be employed to express the frequency with respect to the viscous time scale. The dimensionless advection equation reads

$$\frac{\mathrm{d}\boldsymbol{x}}{\mathrm{d}t} = \mathrm{Str}^{-1}\boldsymbol{u}(\boldsymbol{x}, t). \tag{2.6}$$

2.3 Methods of investigation

2.3.1 Stroboscopic projection

The positions of fluid elements are recorded every time the lid's motion reaches a given phase. We select the phase of maximum positive velocity, corresponding to the times $t = k$, $k \in \mathbb{N}$. At these times, as well as for $t = k + 1/2$, the positions of KAM tori are

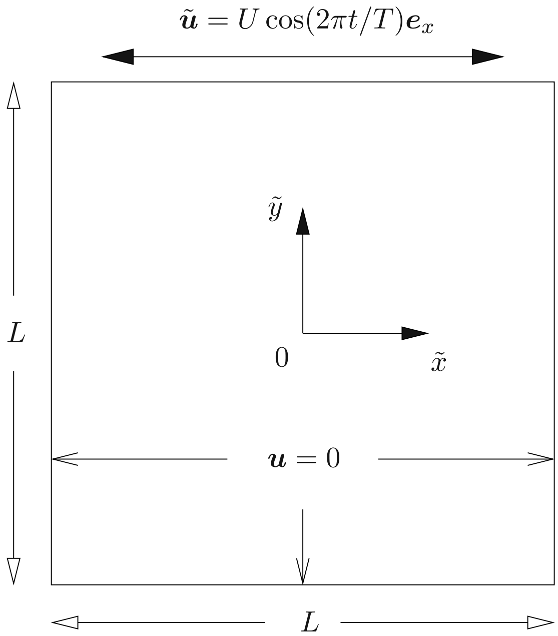

Figure 2.4: Sketch of a two-dimensional square cavity with a harmonic tangential motion of the lid

the least sensitive to Str, and they can be easily grouped into pairs. For each torus in the left half of the cavity, a counter-part exists in the right half. This property will be illustrated in more detail.

The trajectories used for the stroboscopic projection are started from a set of uniformly distributed points. Initially, a grid of 10×10 points is used. When at least some of the trajectories are chaotic, their stroboscopic projection gradually covers the entire chaotic sea. Regions not visited by the chaotic trajectories then typically correspond to KAM tori. The resolution of the initial points is increased up to 25×25 when the structure of KAM tori is complicated. The trajectories are integrated for at least 100 periods. When the Reynolds number is low, and the frequency is high, the winding time is typically very long, $\tau_{\mathrm{w}} \gg 1$. It is then necessary to compute the trajectories for up to 1000 periods to obtain complete outlines of at least some of the tori.

2.3.2 Visualization of heteroclinic connections

Only regular heteroclinic connections, i.e., those that separate two sets of nested KAM tori, are visible directly in the stroboscopic projection. In order to visualize the transverse heteroclinic connections within the chaotic sea, closed hyperbolic trajectories must first be found. In the stroboscopic projection, they can be observed as hyperbolic fixed points $\boldsymbol{X}_{\mathrm{F}}$. These are computed iteratively with the Newton–Raphson method

$$\boldsymbol{X}_{\mathrm{F}}^{(k+1)} = \boldsymbol{X}_{\mathrm{F}}^{(k)} - \left[\nabla \boldsymbol{F}(\boldsymbol{X}_{\mathrm{F}}^{(k)})\right]^{-1} \cdot \boldsymbol{F}(\boldsymbol{X}_{\mathrm{F}}^{(k)}) \tag{2.7}$$

as zero points of the displacement function

$$\boldsymbol{F}(\boldsymbol{X}) := \boldsymbol{f}^n(\boldsymbol{X}) - \boldsymbol{X} \stackrel{!}{=} 0, \tag{2.8}$$

where $\boldsymbol{x}(n) = \boldsymbol{f}^n(\boldsymbol{x}(0))$ maps an initial point $\boldsymbol{X} \equiv \boldsymbol{x}(0)$ of a trajectory $\boldsymbol{x}(t)$ started at time $t = 0$ to its final point $x(n)$ after n periods of the flow. n must match the periodicity of the searched closed trajectory. The Jacobian

$$\nabla \boldsymbol{F}(\boldsymbol{X}) = \nabla \boldsymbol{f}^n(\boldsymbol{X}) - \boldsymbol{I} \tag{2.9}$$

is approximated with centered finite differences

$$\nabla \boldsymbol{f}^n(\boldsymbol{X}) \approx \left(\frac{\boldsymbol{f}^n(\boldsymbol{X}+\delta \boldsymbol{e}_x) - \boldsymbol{f}^n(\boldsymbol{X}-\delta \boldsymbol{e}_x)}{2\delta} \quad \frac{\boldsymbol{f}^n(\boldsymbol{X}+\delta \boldsymbol{e}_y) - \boldsymbol{f}^n(\boldsymbol{X}-\delta \boldsymbol{e}_y)}{2\delta} \right) \tag{2.10}$$

following Farazmand and Haller (2012). The type of the closed trajectory is related to the eigenvalues $\lambda_{1,2}$ of $\nabla \boldsymbol{f}^n(\boldsymbol{X}_\mathrm{F})$ as follows (Ottino, 1989):

Hyperbolic	$\lvert\lambda_1\rvert > 1 > \lvert\lambda_2\rvert \wedge \lambda_1\lambda_2 = 1$
Parabolic	$\lambda_{1,2} = \pm 1$
Elliptic	$\lvert\lambda_{1,2}\rvert = 1 \wedge \lambda_{1,2} \neq 1.$

In the hyperbolic case, the eigenvectors corresponding to λ_1 and λ_2 point in the most repelling and attracting direction, respectively.

Once a hyperbolic trajectory is found, 50 initial points are uniformly distributed along a small circle about its starting point. They represent an outline of a small blob of marked fluid, discretized into connected line segments. As the flow advects the initial points, the blob is stretched into a thin filament along the most repelling directions of the hyperbolic trajectory. The outline of the blob houses the unstable manifold. Due to a rapid increase of the perimeter of the outline, its discretization must be refined during the advection to accurately represent its shape. Therefore we apply the adaptive refinement algorithm of Meunier and Villermaux (2010). After every 10^{-3} convective time units the curvature $\kappa(s)$ parametrized with the arc-length coordinate s is approximated by cubic spline interpolation of its points $x_o(s_i), y_o(s_i)$ and using the formula

$$\kappa = \frac{\lvert x_o' y_o'' - y_o' x_o'' \rvert}{(x_o'^2 + y_o'^2)^{3/2}}. \tag{2.11}$$

The length of an i-th line segment is then restricted by

$$\lvert s_{i+1} - s_i \rvert < \frac{\Delta l}{1 + \alpha \kappa(s_{i+1/2})}, \tag{2.12}$$

where $\Delta l = 10^{-3}$ is the maximum segment length for zero curvature and $\alpha = 30\Delta l/\pi$ controls the sensitivity of the segment length to the curvature. s_{i+1}, s_i and $s_{i+1/2}$ are the values of s at the segment endpoints and at its center respectively. Those segments which exceed the length restriction are split in two parts connected at a new point $[x_o(s_{i+1/2}), y_o(s_{i+1/2})]$, obtained by evaluating the spline interpolation at the segment center.

A stable manifold of a hyperbolic trajectory can be obtained similarly, integrating the fluid trajectories backward in time. This is equivalent to a forward integration of the problem

$$\frac{\mathrm{d}\boldsymbol{x}}{\mathrm{d}t} = -\mathrm{Str}^{-1}\boldsymbol{u}(\boldsymbol{x}, -t). \tag{2.13}$$

In order to illustrate a transverse heteroclinic connection, we compute an unstable manifold of one hyperbolic trajectory and a stable manifold of the other trajectory.

2.3.3 Visualization of the temporal evolution of KAM tori

The stroboscopic projection shows the outlines of KAM tori at a single phase of the lid motion. These outlines can move and deform significantly throughout the oscillation cycle as they are advected by the flow. In order to visualize the entire spatio-temporal structure of a torus, we collect pieces of a regular trajectory from subsequent flow periods into a single three-dimensional plot in the parameter space $(x, y, t) \in \Omega \times [0, 1]$. This is equivalent to plotting a set of trajectories started from the points outlining the torus in the stroboscopic projection. We order these points based on their polar angle

$$\theta_\mathrm{F} = \arctan\frac{Y - Y_\mathrm{F}}{X - X_\mathrm{F}} \tag{2.14}$$

with respect to the center of the torus $\boldsymbol{X}_\mathrm{F}$. The outline of a torus is then approximated by connecting these ordered points. The advection of this outline along the regular trajectory reconstructs the surface of the torus in the parameter space (x, y, t). Only the largest torus of each set of nested tori is selected for visualization.

2.3.4 Winding times of regular trajectories

In order to quantify the winding time τ_w, we compute the cumulative winding angle $\theta_\mathrm{F}(t)$ over the same number of periods $K \in \mathbb{N}$ as used for the stroboscopic projection. The winding time is then computed as

$$\tau_w = \frac{2\pi K}{\theta_\mathrm{F}(K) - \theta_\mathrm{F}(0)}. \tag{2.15}$$

2.3.5 Quality of stirring

The stirring ability of a flow can be quantified in many ways. Chapter VII of Aref et al. (2017) gives a summary of possible methods. We follow the concept of *coarse-grained density*. A portion of marked fluid is initiated in some unmixed state - i.e., the perimeter of the outline should be small compared to the area of the marked fluid. The requirement on the stirring is to uniformly distribute the marked fluid across the flow domain on some global scale, such that on a small scale, the mixing can be completed, e.g., by diffusion. To that end, the domain is divided into N_δ sub-regions with the same areas S_δ. The proportion of marked fluid

$$D_i(t) = \frac{S_b^{(i)}(t)}{S_\delta} \tag{2.16}$$

within each sub-region i (fig. 2.5b) can then be evaluated over time, where $S_b^{(i)}(t)$ is the area of the marked fluid inside that sub-region. D_i is also called a *coarse-grained density*. The overall proportion of the marked fluid inside the domain

$$\langle D \rangle = \frac{\sum_{i=1}^{N_\delta} S_b^{(i)}}{N_\delta S_\delta} \tag{2.17}$$

and the mean of the squared local proportions

$$\left\langle D^2 \right\rangle (t) = \frac{1}{N_\delta} \sum_{i=1}^{N_\delta} D_i^2(t) \tag{2.18}$$

then define the variance $\langle D^2 \rangle - \langle D \rangle^2$. By scaling the variance with its largest possible value, one obtains the coarse-grained intensity of segregation

$$I(t) = \frac{\langle D^2 \rangle - \langle D \rangle^2}{\langle D \rangle (1 - \langle D \rangle)} \qquad \in [0, 1]. \tag{2.19}$$

We initialize the marked fluid as a square of side length 1/2 in the center of the cavity (fig. 2.5a) and divide the domain into $N_\delta = 400$ squared sub-regions of side length $\delta_S = 0.05$. This configuration was selected such that the initial outline of the marked fluid overlaps with the boundaries of the sub-regions. The initial intensity of segregation is then $I(0) = 1$, corresponding to a perfectly unmixed state. The outline of the marked fluid is again discretized into connected fluid elements, which are advected by the flow, and it is adaptively refined with the aforementioned algorithm. Each side of the initial square is refined as a separate curve because the curvature would diverge at the edges. The same parameters Δl and α are used as for the visualization of stable and unstable manifolds, although this typically leads to a large number of fluid elements for the representation of the outline. The computation is terminated when at least one of the sides of the initial square is discretized into more than 50 000 fluid elements, which indicates a well-stirred state, or when the convective time t/Str from the start of the advection reaches 100.

The intensity of segregation $I(t)$ was evaluated only every half-period of the flow to filter out transient stretching of the marked fluid within a single oscillation cycle. These data points (fig. 2.5c) were then fitted by an exponential decay $\exp[-t/(\tau_m \mathrm{Str})]$ with the characteristic decay time τ_m expressed in convective scaling.

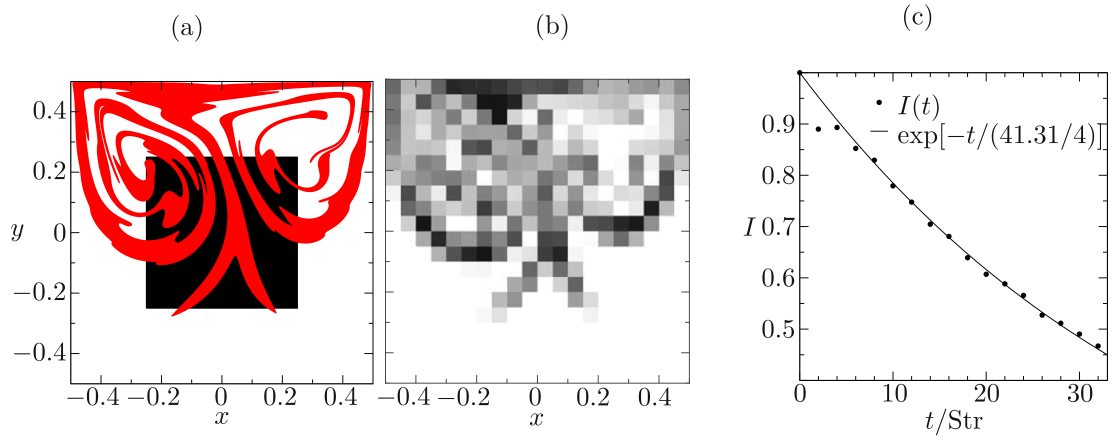

Figure 2.5: Quantification of the stirring ability of a flow for $\mathrm{Re} = 50, \mathrm{Str} = 0.25$. (a) Initial (black) and final (red) shape of a portion of marked fluid advected for eight periods of the flow; (b) The distribution of the coarse-grained density $D_i(8)$ at the final state; (c) Exponential fit of the intensity of segregation $I(t)$

2.3.6 Numerical methods

Velocity field

The velocity field $\boldsymbol{u}(\boldsymbol{x}, t)$ is computed with an open-source spectral-element solver NEK5000 (Fischer et al., 2008), based on FORTRAN 77. Internally, the default convective scaling of the problem (2.4, 2.5) is used, i.e., the time is scaled with L/U instead of T. The problem is discretized in space with the continuous Galerkin method on a uniform Cartesian grid of 20×20 square elements. The velocity and pressure fields are represented element-wise with 7^{th} and 5^{th} order Lagrange polynomials on Gauss-Legendre-Lobatto and Gauss-Legendre nodes, respectively ($\mathbb{P}_N - \mathbb{P}_{N-2}$ method). The same nodes are used to approximate the integrals arising in the weak formulation of the Navier–Stokes equations with an element-wise Gauss(-Lobatto) quadrature. An exception is the convective term, which is integrated with a 12-point Gauss-Lobatto quadrature. The *over-integration* of the convective term on $3(N+1)/2$ points, where N is the polynomial order of velocity, is recommended by Mengaldo et al. (2015) in order to suppress numerical instabilities due to aliasing.

A third-order Adams–Moulton method is used for the discretization in time. The typical difficulty with an implicit discretization of the Navier–Stokes equations lies in the presence of the convective term, which makes the resulting system of algebraic equations non-linear. It could be solved iteratively for every time step, which would, however, significantly increase the computational demand. Instead, the convective term at the unknown time step is approximated by extrapolating the known time steps with the third-order Adams-Bashforth method. This conserves the overall third-order accuracy in time.

The third-order Adams-Moulton and Adams-Bashforth methods require the last three time steps to be available in memory. Lower order discretization is employed when the computation starts from initial conditions or a saved velocity field until the first three steps have been computed. If it is desired to restart the computation without the drop in the accuracy of the initial steps, the Checkpointing routines from the KTH Framework (github.com/KTH-Nek5000) can be employed. These were, however, not used in the present study.

The coupling between the evolution of velocity and pressure through the incompressibility constraint is further approximated with the Fractional Step Method (also known as the projection method or splitting method):

1. The velocity at the next time step is first predicted using the pressure field from the known time step. The predicted velocity field is generally not incompressible unless the flow is steady.
2. Using the predicted velocity, a correction of pressure is computed such that it enforces incompressibility.
3. The velocity and pressure at the next time step are then corrected using the pressure correction.

The second and third steps can be understood as a projection of the predicted velocity onto a space of divergence-free vector fields. This method is advantageous from the point of view of computational efficiency. It, however, introduces a so-called *splitting error* of the discretization in time. Thanks to Perot (1993), a Fractional Step Method of arbitrary order of accuracy can be designed. The one implemented in NEK5000 is of third-order, matching the overall accuracy of the temporal discretization.

In order to validate the implementation and assess the grid convergence, a steady two-dimensional lid-driven cavity flow is first computed and compared to the benchmark data of Botella and Peyret (1998) in table 2.1. The lid moves with constant speed in the positive x direction. The flow is started from rest

$$\boldsymbol{u}(\boldsymbol{x}, t=0) = 0 \tag{2.20}$$

and the convergence to a steady state is indicated by the criterion

$$\max_{i,j} \frac{|u_i(\boldsymbol{x}_j, t) - u_i(\boldsymbol{x}_j, t-\Delta t)|}{\Delta t} \leq 10^{-7}, \tag{2.21}$$

where i and j enumerate the velocity components and the grid points, respectively.

The flow governed by (2.4, 2.5) is as well started from rest, and the initial evolution towards a fully-developed time-periodic flow is monitored by the maximum change of any velocity component at any grid point from one period to the other

$$R_k = \max_{i,j} |u_i(\boldsymbol{x}_j, k) - u_i(\boldsymbol{x}_j, k-1)|, \qquad k \in \mathbb{N} \tag{2.22}$$

	$-u_{\min}$	$y_{\min}$	$v_{\max}$	$x_{\max}$	$-v_{\min}$	$x_{\min}$
101 × 101	0.2140434	−0.0419	0.1795745	−0.2630	0.2538089	0.3104
141 × 141	0.2140423	−0.0419	0.1795727	−0.2630	0.2538031	0.3104
B & P	0.2140424	−0.0419	0.1795728	−0.2630	0.2538030	0.3104

Table 2.1: The minimum of the horizontal velocity along the vertical center-line $u_{\min}(0, y_{\min})$ and the extrema of the vertical velocity along the horizontal center-line $v_{\max}(x_{\max}, 0)$, $v_{\min}(x_{\min}, 0)$ in a steady lid-driven cavity for Re = 100 computed with 5^{th} and 7^{th} order element-wise polynomial approximation of velocity, leading to a total number of 101 × 101 and 141 × 141 nodes for velocity. B & P indicates the results of Botella and Peyret (1998).

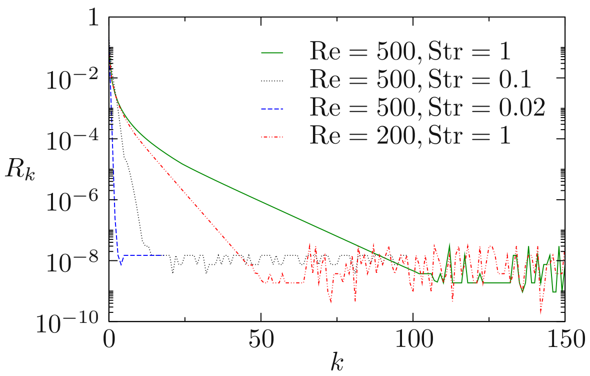

Figure 2.6: The evolution of R_k (2.22) with the number of periods k from the start of the lid motion

for a given phase of the lid motion. The higher the Stokes number, the more periods are required for reaching a time-periodic state (fig. 2.6). Within this investigation, St ≤ 500 and the time-periodic state, indicated by the criterion $R_k < 10^{-7}$, is reached after less than 100 periods. The velocity and pressure of the last time step are then saved to a file, and the computation is terminated. Afterward, the flow is restarted from the saved file, and the velocity field at 1000 uniformly distributed time steps over one flow period is saved. Further flow evolution is constructed as a periodic extension of this one period.

Fluid trajectories

The integration of (2.2) requires evaluation of the velocity $\boldsymbol{u}$ along the trajectory $\boldsymbol{x}(t)$. The nodal values obtained from the spectral-element solver are thus interpolated element-wise with Lagrange polynomials

$$\boldsymbol{u}(x, y, t) = \sum_{i,j=1}^{N+1} \boldsymbol{u}_{i,j}(t) l_i(x) l_j(y), \qquad l_i(x) = \prod_{\substack{k=1 \\ k \neq i}}^{N+1} \frac{x - x_k}{x_i - x_k} \tag{2.23}$$

i	1	2	3	4	5	6	7
e_i	71/57600	0	-71/16695	71/1920	-17253/339200	22/525	-1/40

Table 2.2: Coefficients for the error estimate (2.27) of the RK5(4)7M method

where $N = 7$ is the polynomial order. The trajectories started from a set of initial conditions $\boldsymbol{X} = \boldsymbol{x}(0)$ are obtained by integrating (2.2) with the adaptive-time-step 5$^{\text{th}}$ order Runge-Kutta method RK5(4)7M of Dormand and Prince (1980)

$$\boldsymbol{k}_{i,j} = \boldsymbol{u}\left(t_n + c_i\Delta t,\ \boldsymbol{x}_j(t_n) + \Delta t(a_{i,1}\boldsymbol{k}_{1,j} + \cdots + a_{i,i-1}\boldsymbol{k}_{i-1,j})\right) \tag{2.24a}$$

$$\boldsymbol{x}_j(t_{n+1}) = \boldsymbol{x}_j(t_n) + \Delta t \sum_{i=1}^{7} b_i \boldsymbol{k}_{i,j} + \mathcal{O}\left(\Delta t^6\right) \tag{2.24b}$$

implemented in the MATLAB function `ode45`. The subscript j enumerates the computed trajectories. At each step, the positions of fluid elements $\boldsymbol{x}_j(t_{n+1})$ are computed with RK5, and the relative error is estimated by comparison to the result of RK4

$$\epsilon \approx \frac{\|\boldsymbol{x}_j(t_{n+1}) - \hat{\boldsymbol{x}}_j(t_{n+1})\|_2}{\|\boldsymbol{x}_j(t_{n+1})\|_2}. \tag{2.25}$$

Although the computation of RK5 with seven intermediate directions $\boldsymbol{k}$ is sub-optimal, the method is designed such that the RK4 reuses them

$$\hat{\boldsymbol{x}}_j(t_{n+1}) = \boldsymbol{x}_j(t_n) + \Delta t \sum_{i=1}^{7} \hat{b}_i \boldsymbol{k}_{i,j}. \tag{2.26}$$

The coefficients $a_{i,1\ldots6}, b_i, \hat{b}_i, c_i$ are given in table 2 of Dormand and Prince (1980). The error estimate can also be expressed directly

$$\epsilon \approx \frac{\left\|\sum_{j}^{7} e_j \boldsymbol{k}_{i,j}\right\|_2}{\|\boldsymbol{x}_j(t_{n+1})\|_2} \tag{2.27}$$

without the explicit computation of $\hat{\boldsymbol{x}}_i(t_{n+1})$. The coefficients e_j used in `ode45` are given in tab. 2.2. The step size for the next step is then adapted according to

$$\Delta t \leftarrow 0.8\Delta t \left(\frac{\texttt{tol}}{\epsilon \Delta t}\right)^{1/5}. \tag{2.28}$$

The relative tolerance is set to $\texttt{tol} = 10^{-8}$. A custom version of `ode45` has been implemented for the advection of adaptively refined curves, where the number of trajectories changes over time.

The times at which the velocity is evaluated are not restricted to those saved from the flow solver. It is, therefore, necessary to interpolate $\boldsymbol{u}$ in time as well. The nodal Fourier

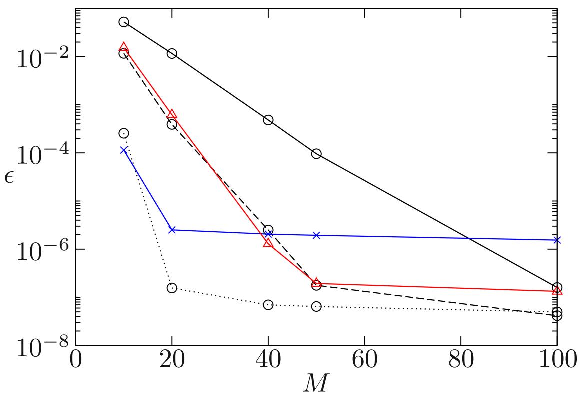

Figure 2.7: Convergence of the nodal Fourier interpolation (2.29) for Str = 0.01

interpolation

$$\boldsymbol{u}_{i,j}^{(M)}(t) = \sum_{k=1}^{M} \frac{\boldsymbol{u}_{i,j}(t_k)}{M} \sin\left[\frac{M}{2}(t-t_k)\right] \cot\left[\frac{1}{2}(t-t_k)\right] \tag{2.29}$$

is employed (Kopriva, 2009), where k enumerates M uniformly distributed time steps over one period. The accuracy of the interpolation is assessed by comparison to all 1000 steps saved from the solver

$$\epsilon_M = \frac{\left\|\boldsymbol{u}_{i,j}^{(M)}(t_k) - \boldsymbol{u}_{i,j}(t_k)\right\|_2}{\|\boldsymbol{u}_{i,j}(t_k)\|_2}, \qquad k = 1, \ldots, 1000. \tag{2.30}$$

The flow is well represented by less than $M \leq 100$ steps (fig. 2.7). The saturation of ϵ_M at $\mathcal{O}(10^{-6})$ for Str $= 1$ and $\mathcal{O}(10^{-8})$ for Str $= 0.01$ is related to the restarting of the flow solver after a time-periodic state is reached. As described in the previous section, the first two time steps after the restart are computed with lower-order discretization in time. Due to the higher discretization error at these steps, the computed velocity is only periodic up to the level at which ϵ_M saturates. This accuracy was considered sufficient for the present study. The velocity field (2.29) used for the computation of trajectories is time-periodic by definition.

Interpolation of the velocity field near a discontinuous boundary condition

The velocity field obtained from the spectral-element flow solver suffers from Gibbs undulations (fig. 2.8) close to the corners where the moving lid meets the steady walls. This causes stiffness of the advection problem (2.2) as accurate computation of trajectories passing close to one of these corners requires a much smaller time-step size than in the rest of the domain. The computation of trajectories with the Dormand–Prince algorithm in such velocity field then typically becomes prohibitively computationally demanding.

Thus, we propose an ad-hoc modification

$$\boldsymbol{u}(x,y,t) = \boldsymbol{u}_a(x,y,t) + \sum_{i,j=1}^{N+1} \left[\boldsymbol{u}_{i,j}(t) - \boldsymbol{u}_a(x_i,y_j,t)\right] l_i(x) l_j(y) \tag{2.31}$$

of the interpolation (2.23) on the spectral elements containing the discontinuous boundary condition. $\boldsymbol{u}_a$ is some function that matches the prescribed discontinuous boundary conditions at the corner points, but is continuous in the rest of the domain. The Lagrange polynomials then interpolate only the remainder field, for which the boundary conditions are continuous. $\boldsymbol{u}_a$ should be a good approximation of $\boldsymbol{u}$ close to the discontinuity, without the artificial oscillation. The analytical Stokes flow near the corner

$$\psi_0(r,\theta) = \frac{4ru(y=1/2)}{\pi^2-4}\left(\frac{\pi^2+2\pi\theta}{4}\sin\theta - \theta\cos\theta\right) \tag{2.32}$$

due to Gupta et al. (1981) is employed in the following way

$$\boldsymbol{u}_a = \begin{pmatrix} \partial_y\psi_0\left(r^{\mathrm{A}},\theta^{\mathrm{A}}\right) + \partial_y\psi_0\left(r^{\mathrm{B}},\theta^{\mathrm{B}}\right) \\ -\partial_x\psi_0\left(r^{\mathrm{A}},\theta^{\mathrm{A}}\right) - \partial_x\psi_0\left(r^{\mathrm{B}},\theta^{\mathrm{B}}\right) \end{pmatrix} \tag{2.33}$$

$$\theta^{\mathrm{A,B}} = -\operatorname{sign}\left(x^{\mathrm{A,B}}\right)\arctan\frac{y-y^{\mathrm{A,B}}}{x-x^{\mathrm{A,B}}} \qquad r^{\mathrm{A,B}} = \|\boldsymbol{x}-\boldsymbol{x}^{\mathrm{A,B}}\|_2$$

$$\boldsymbol{x}^{\mathrm{A}} = \left[x^{\mathrm{A}},y^{\mathrm{A}}\right] = \left[-\frac{1}{2},\frac{1}{2}\right] \qquad \boldsymbol{x}^{\mathrm{B}} = \left[x^{\mathrm{B}},y^{\mathrm{B}}\right] = \left[\frac{1}{2},\frac{1}{2}\right].$$

Figure 2.8 shows that this *a posteriori* treatment removes the undulation in the interpolated velocity field.

The velocity at the corner points is set to zero, i.e., the no-penetration condition has a priority over the no-slip condition. This is to ensure that no fluid trajectories enter or leave the domain. If, on the other hand, the no-slip condition was enforced at the corner, the Stokes flow solution of Riedler and Schneider (1983) could be employed to take a leakage of fluid between the lid and the sidewalls into consideration.

2.4 Results

2.4.1 Instantaneous velocity field

It is confirmed by an inspection of the Fourier spectrum of velocity (fig. 2.9) that the flow is strictly periodic with the period of lid oscillation within the investigated parameter space $\mathrm{Re} \in [1,500], \mathrm{Str} \in [0.01,1]$. Furthermore, it is invariant under translation by half a period together with a reflection about the vertical axis $x=0$

$$\begin{pmatrix} u \\ v \end{pmatrix}(x,y,t) = \begin{pmatrix} -u \\ v \end{pmatrix}(-x,y,t+1/2), \tag{2.34}$$

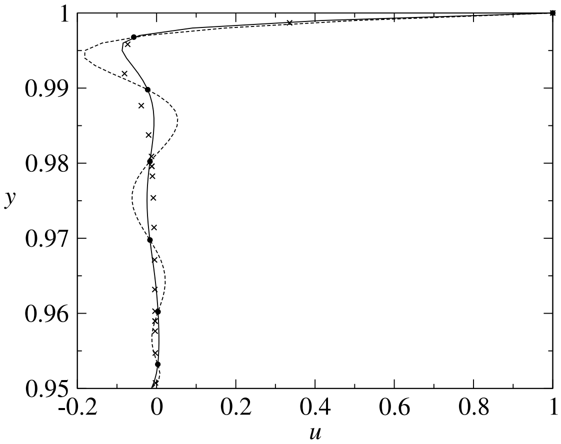

Figure 2.8: Modified interpolation of the velocity field near the corners with a discontinuous boundary condition. Black dots are the nodal values, dashed line is their Lagrange interpolation (2.23), while the solid line is the modified interpolation (2.31). Nodal values computed with a refined mesh are plotted by crosses for reference.

as shown by Vogel et al. (2003). Figure 2.10 shows an example of instantaneous streamlines and a vertical profile of the horizontal velocity during and acceleration phase of the lid in the positive x direction. The Stokes number $\mathrm{St} = 500$ corresponds to the Stokes layer thickness $\lambda/L = 0.04$. During the initial stage of the lid acceleration, most of the cavity is occupied with an anti-clockwise vortex which survives from the previous half-period with negative lid velocity. An undular boundary layer is observed not only at the lid but also along most of the stationary walls. Four elliptic points are observed within this layer - one near the left wall, one near the bottom wall, and two near the top right corner. They gradually merge into a single center of a clockwise vortex which grows and replaces the anti-clockwise vortex. The anti-clockwise vortex eventually vanishes near the downstream corner. As the lid velocity reaches a maximum and enters the deceleration phase, the center of the clockwise vortex moves from the vicinity of the upper right corner into the bulk of the cavity. The reader is referred to Zhu et al. (2020) for a detailed description of the instantaneous vortical structure in a harmonically driven cavity with a width-to-height ratio of 2.

When the Reynolds number is low $\mathrm{Re} \sim \mathcal{O}(1)$ (fig. 2.11a,d), the streamlines of the instantaneous flow are close to symmetric about the vertical axis $x = 0$ and they do not vary significantly during the oscillation cycle. Most of the cavity is occupied by a single large vortex which changes its sense of rotation when the lid changes the direction of motion. The spatial distribution of the variance $\sigma^2(|\boldsymbol{u}|)$ of velocity magnitude is similar to the distribution of the velocity magnitude itself. In case of a low frequency of the lid oscillation $\mathrm{Str} \ll 1$, the time derivative term in (2.4a) becomes comparatively small, and the flow can be considered quasi-steady. This means that at every time instance, the instantaneous flow resembles a steady lid-driven cavity flow, even when the Reynolds number is increased (fig. 2.11b,c). The instantaneous streamlines, however, become

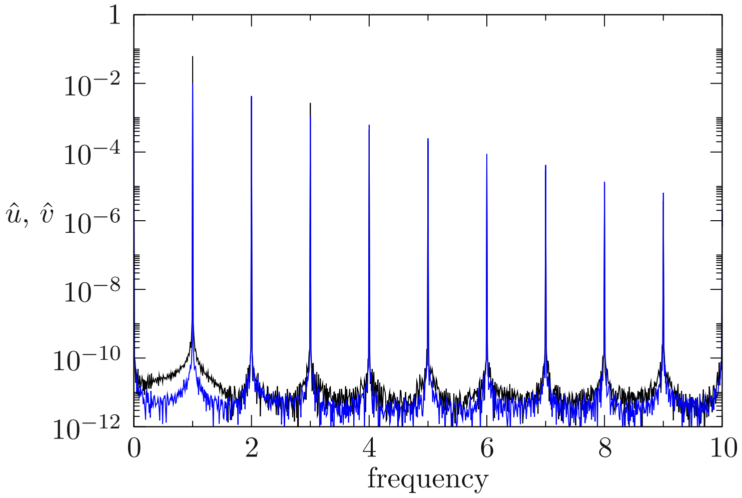

Figure 2.9: Fourier spectra $\hat{u}$ (black) and $\hat{v}$ (blue) of the horizontal and vertical velocity, respectively, at the point $(x, y) = (1/4, 1/4)$ for Re = 500 and Str = 0.1.

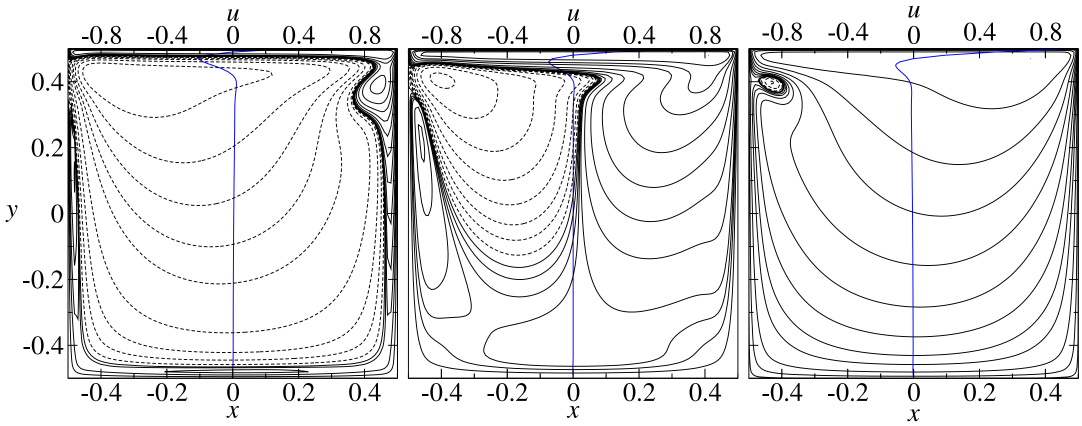

(a) $\phi = 1.625\pi$ (b) $\phi = 1.75\pi$ (c) $\phi = 1.9\pi$

Figure 2.10: Streamlines (black) and velocity profile $u(x = 0)$ (blue) on the vertical centerline for Str = 1 and Re = St = 500 shown during the acceleration phase of the lid in the positive x direction. Full and dashed lines indicate negative (clockwise rotation) and positive stream function (counter-clockwise rotation), respectively. The streamlines are distributed logarithmically.

asymmetric for higher Reynolds numbers, and thus they vary more significantly in time. The peaks of the variance then identify the areas with the largest velocity magnitude over the cycle. For large Stokes number, St $\sim \mathcal{O}(10^2)$ (fig. 2.11e,f), most of the variation of the flow in time occurs in the Stokes layer near the lid.

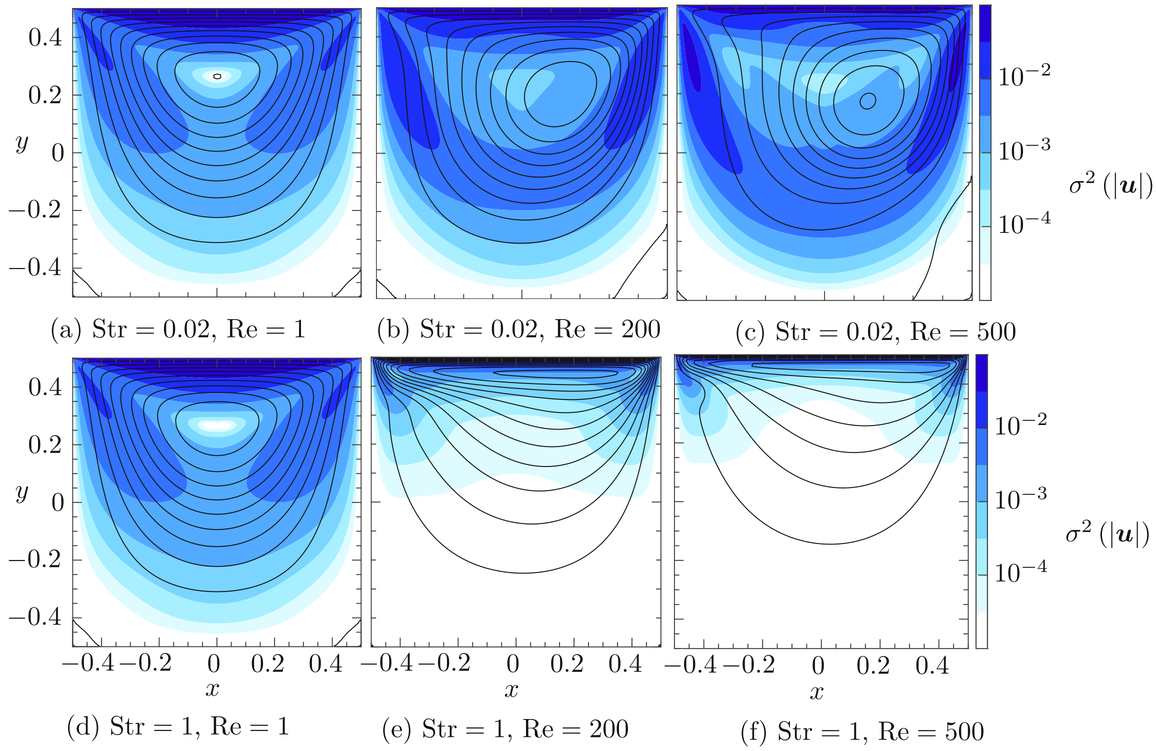

Figure 2.11: Time-variance (color) of the velocity magnitude $\sigma^2(|\boldsymbol{u}|)$ and streamlines (black) of the instantaneous flow at the largest positive velocity of the lid. Re and Str as indicated.

2.4.2 Mean flow

It was shown in the previous section that when the Reynolds number is not small, Re $\gtrsim 1$, the instantaneous streamlines are asymmetric with respect to the centerline $x = 0$. This induces a non-zero time-averaged velocity field $\bar{u}$ (fig. 2.12) and makes the flow irreversible. The mean flow can naturally affect net fluid transport after a complete period of the lid motion. The structure of the mean flow is the same within the investigated parameter range. It consists of one larger pair of vortices that occupy most of the domain and one smaller pair near the bottom corners. Both vortex pairs are mirror-symmetric with respect to the axis $x = 0$. The strength of the mean flow increases with the Reynolds number, as expected. For higher Stokes numbers, it concentrates near the upper corners of the cavity. The size of the bottom vortices typically increases with the Reynolds number up to a certain threshold, beyond which they shrink again upon a further increase of Re. The threshold decreases when the convective frequency Str is increased.

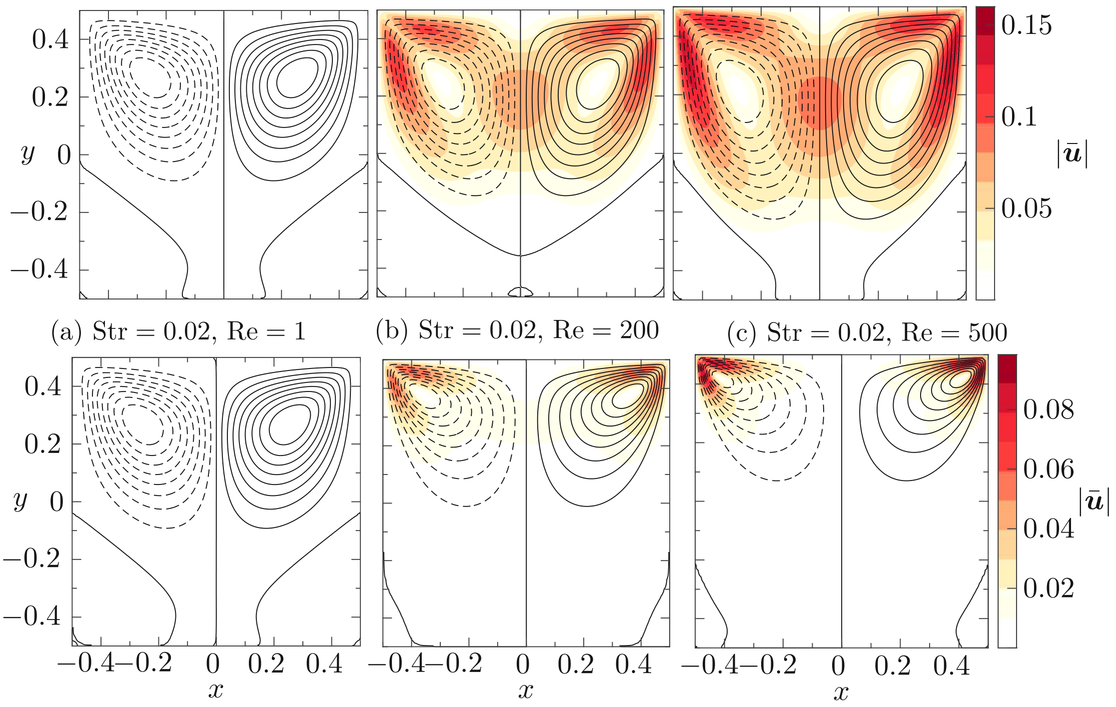

(a) Str = 0.02, Re = 1 (b) Str = 0.02, Re = 200 (c) Str = 0.02, Re = 500

(d) Str = 1, Re = 1 (e) Str = 1, Re = 200 (f) Str = 1, Re = 500

Figure 2.12: Magnitude (color) and streamlines (black) of the time-averaged velocity field $\bar{\boldsymbol{u}}$. Re and Str as indicated in the sub-captions.

2.4.3 Kolmogorov–Arnold–Moser tori

When the Reynolds number is low Re $= 1$ (fig. 2.13), only regular trajectories are observed for all investigated frequencies Str $\in [0.01, 1]$. The periodicity of all tori is $n = 1$. In the stroboscopic projection to $t = k$, $k \in \mathbb{N}_0$, the sets of tori are clearly divided into two groups of equal size by a separatrix that connects the center of the bottom wall with the center of the lid. Each torus from one group has a matching counterpart in the other group, i.e., all tori are paired. Each pair is symmetric with respect to the reflection-translation (RT) transformation

$$(x, y, t) \to \left(-x, y, t + \frac{1}{2}\right). \tag{2.35}$$

The separatrix, formed by a (sequence of) heteroclinic connection(s), is rather straight in the bottom part of the cavity but becomes undular near the lid. It, of course, deforms in time as it is advected by the flow. Interestingly, the wavelength of the undulation does not correlate with the Stokes layer thickness St$^{-1/2}$.

For a high frequency of the lid oscillation Str $> 5.9 \times 10^{-2}$, the intersections of KAM tori with the projection plane $t = k$ (fig. 2.13a) resemble the streamlines of the mean flow for the same parameters (fig. 2.12d), except the small pair of tori below the lid.

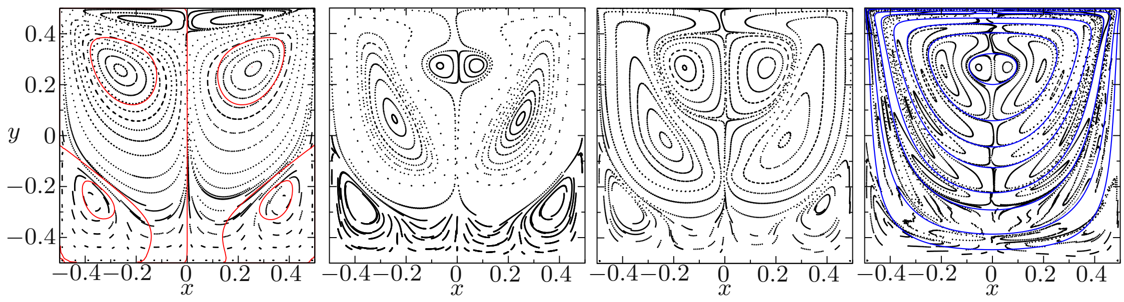

(a) Str = 1 (b) Str = 0.059 (c) Str = 0.05 (d) Str = 0.01

Figure 2.13: Stroboscopic projection (dots) of fluid trajectories to $t = k$, $k \in \mathbb{N}$ for Re = 1 and different frequencies of the lid oscillation indicated in the sub-captions. The red curves in (a) are the streamlines of the mean flow $\bar{\boldsymbol{u}}$ and the blue lines in (d) are the streamlines of the instantaneous velocity field at $t = k$.

Thus, we conclude that the mean flow dominates the net fluid transport. A heuristic explanation can be constructed using the convective scaling of time $t_c = t/\mathrm{Str}$, under which the duration of a flow is proportional to the length of fluid trajectories. The final position of a fluid element after one period is given by an integral of velocity along its trajectory

$$\boldsymbol{x}\left(t_c = \mathrm{Str}^{-1}\right) = \int_0^{\mathrm{Str}^{-1}} \boldsymbol{u}\left(\boldsymbol{x}(t_c), t_c\right) \mathrm{d}t_c. \tag{2.36}$$

When the convective period Str^{-1} of the flow is short, the trajectory of a fluid element is also short, and thus it stays close to its initial position during the entire flow cycle. The integral of velocity along its trajectory is then similar to the integral of velocity at its initial position

$$\int_0^{\mathrm{Str}^{-1}} \boldsymbol{u}\left(\boldsymbol{x}(t_c), t_c\right) \mathrm{d}t_c \xrightarrow{\mathrm{Str}^{-1}\to 0} \int_0^{\mathrm{Str}^{-1}} \boldsymbol{u}\left(\boldsymbol{x}(0), t_c\right) \mathrm{d}t_c \tag{2.37}$$

which approximates advection by the mean flow

$$\int_0^{\mathrm{Str}^{-1}} \boldsymbol{u}\left(\boldsymbol{x}(0), t_c\right) \mathrm{d}t_c \equiv \mathrm{Str}^{-1}\bar{\boldsymbol{u}} \approx \int_0^{\mathrm{Str}^{-1}} \bar{\boldsymbol{u}}\left(\boldsymbol{x}(t_c), t_c\right). \tag{2.38}$$

This argument only holds when the velocity field does not vary significantly in space at the length scale of the short trajectory, i.e., when $\boldsymbol{u} \cdot \nabla \boldsymbol{u} \lesssim \mathcal{O}(1)$.

When the frequency is decreased, the small tori below the lid vanish, and for Str $\leq 5.9 \times 10^{-2}$ a new pair of KAM tori appears near the center of the instantaneous Eulerian vortex for $t \in \mathbb{N}$ (fig. 2.13b). These new tori grow upon a further decrease of frequency,

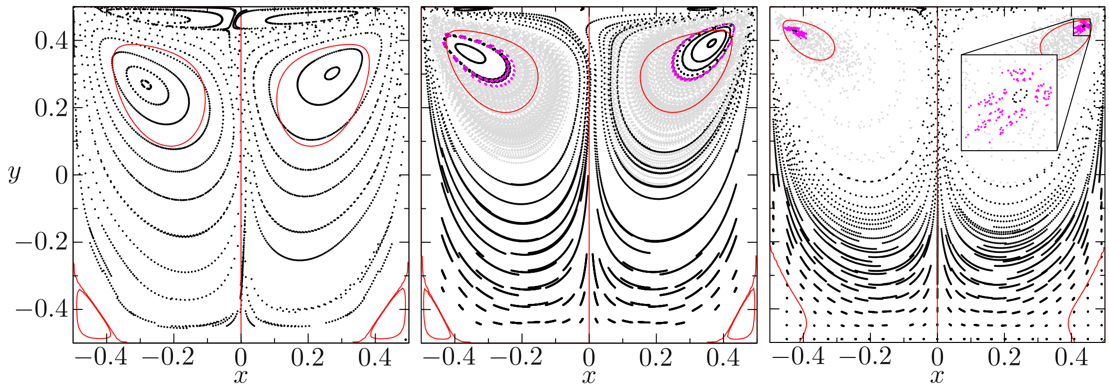

(a) Re = 10 (b) Re = 100 (c) Re = 500

Figure 2.14: Stroboscopic projection to $t = k$ for Str = 1 and various Reynolds numbers as indicated in the sub-captions. Black and magenta dots indicate synchronous and subharmonic regular trajectories, while grey dots indicate chaotic trajectories. Red curves are the streamlines of the mean flow for the same parameters.

displacing the other tori towards the walls. Another tori eventually appear at a similar position, and the same process repeats several times. This leads to a complex structure of multiple sets of stretched tori for low frequencies. We note that for Str ≤ 0.01, most of the tori are stretched along the instantaneous streamlines.

Above, we have considered the structure of fluid trajectories (also called *Lagrangian topology*) for Re = 1. Next, we investigate how it responds to an increase in the Reynolds number. At a certain threshold, the sea of chaotic pathlines emerges, and some of the regular tori with periodicity one break into subharmonic tori. The threshold increases with increasing frequency (fig. 2.21a).

For Str = 1 the Lagrangian topology (fig. 2.14) is not very sensitive to the increase of the Reynolds number. The centers of the largest tori move towards the upper corners, and the smaller tori near the bottom corners and below the lid shrink. This is a similar trend as observed for the time-averaged velocity field. The trajectories remain regular for Re < 100. At Re = 100 we start to observe subharmonic tori of high periodicity and layers of chaotic trajectories between regular tori.

For Re = 500 chaotic trajectories are observed in the upper part of the cavity. On the other hand, the net fluid transport almost vanishes in the lower part. This is expected as the flow in the bottom part of the cavity becomes insignificant (fig. 2.11f). Small tori with period 1 remain around the closed trajectories near the upper corners, surrounded by subharmonic tori of period 5.

For the frequency Str = 0.25 (fig. 2.15), the regular tori in the bulk of the largest nested sets break into subharmonic tori at Re = 20. The periodicity of the subharmonic tori ranges from $p = 5$ near the synchronous ($n = 1$) trajectory up to $p = 9$ further away from the center of the set. It is instructive to consider the dependence of the winding time τ_w of

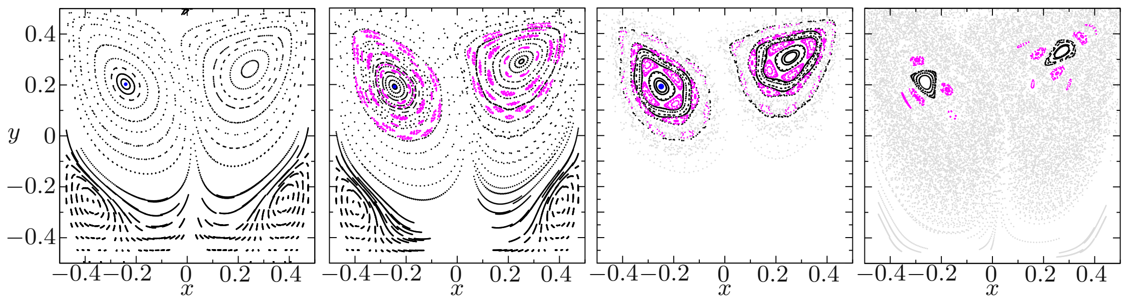

(a) Re = 10 (b) Re = 20 (c) Re = 29 (d) Re = 50

Figure 2.15: Stroboscopic projection to $t = k$ for Str = 0.25. Re as indicated in the sub-captions. Black, magenta and grey dots as in fig. 2.14. The blue dot indicates the closed synchronous elliptic trajectory in the center of the set of tori. The tori at the bottom corners are not shown in (c) and (d).

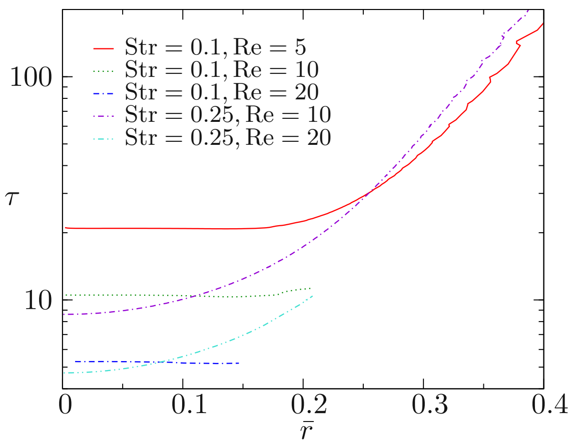

Figure 2.16: Dependence of the winding time τ_w of regular trajectories about the central closed trajectory as a function of the mean radius of cross-section $\bar{r}$ of their KAM tori. The parameters are given in the legend. The cases shown are distinguished by line type and color corresponding to the color of the sub-captions of figs. 2.15(a,b) and 2.17(a–c).

the synchronous tori on the distance from the closed synchronous trajectory (fig. 2.16) in order to identify which resonances lead to the creation of the subharmonic tori. It is seen that for Re = 20 and Str = 0.25 the winding times of the synchronous tori from the largest set vary in the range $\tau_\mathrm{w} \in (4, 10)$. It is thus clear that the subharmonic tori emerged by breaking of the synchronous tori with integer winding times $\tau_\mathrm{w} = p/q = 5/1, \ldots, 9/1$. This means they only wind once about the synchronous closed trajectory before returning to their starting position in the stroboscopic projection plane.

It would be tempting to conclude that resonant tori with integer winding times are more likely to break than those with other rational values of τ_w. We must, however, be aware that the latter might be difficult to observe. The resulting subharmonic tori would have

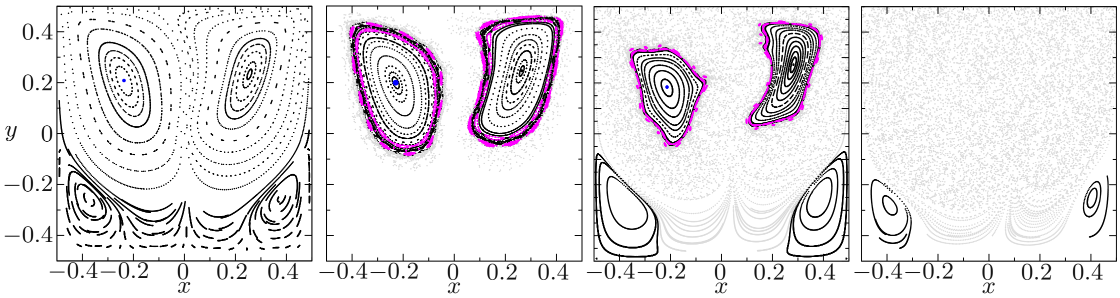

(a) Re = 5 (b) Re = 10 (c) Re = 20 (d) Re = 50

Figure 2.17: Stroboscopic projection to $t = k$ for Str = 0.1. Re as indicated in the sub-captions. Black, magenta and grey dots as in fig. 2.14. The blue dot indicates the closed synchronous elliptic trajectory in the center of the set of tori. The tori at the bottom corners are skipped in (b).

q-times higher periodicity p. Since all of their p parts must fit into the circumference of the resonant torus, the cross-sections of the subharmonic tori might be too small to be captured with the given grid of fluid elements. We will show that resonances with non-integer winding times can be observed when τ_w is sufficiently small and when the circumference of the resonant torus is sufficiently large. It shall be noted that τ_w diverges as $\mathrm{Re} \to 0$ as well as when the tori approach walls (fig. 2.16). The former is due to the reversibility of the Stokes flow and the latter due to the no-slip condition.

When the Reynolds number is further increased, the sea of chaotic trajectories emerges from the synchronous heteroclinic connections, destroying the outermost KAM tori, but also from the subharmonic heteroclinic connections of higher periodicity. The latter create layers of chaotic trajectories separated by the remaining synchronous tori. The subharmonic tori of higher periodicity vanish in these chaotic layers, while new tori of smaller periodicity appear close to the synchronous trajectory. Some of these appreciably grow in size.

For $\mathrm{Str} = 0.1$ (fig. 2.17) the chaotic trajectories emerge from the synchronous heteroclinic connection at even lower Reynolds number $\mathrm{Re} = 10$. In contrast to $\mathrm{Str} = 0.25$, only the outer tori tend to break into subharmonic ones, while those in the bulk of each set survive the increase of the Reynolds number. This is related to the winding time, which is almost constant in the bulk of the set and only starts to increase significantly in the outer part of the set. We do not expect observable resonances in the region where the tori are small, the winding time is still rather high, and it does not cross integer values. For $\mathrm{Str} = 0.1$, $\mathrm{Re} = 10$ (fig. 2.17b) the resonant tori with $\tau_\mathrm{w} = 11$ and 12 break into subharmonic tori with the same period. When the Reynolds number is increased to $\mathrm{Re} = 20$ (fig. 2.17c), the outer tori with non-integer rational winding times $\tau_\mathrm{w} = 21/4$ and $16/3$ break into subharmonic tori with period 21 and 16. As mentioned before, these tori with a long period are rather small, and thus they might be difficult to capture. For $\mathrm{Re} = 50$ (fig. 2.17d) only the tori at the bottom corners survive.

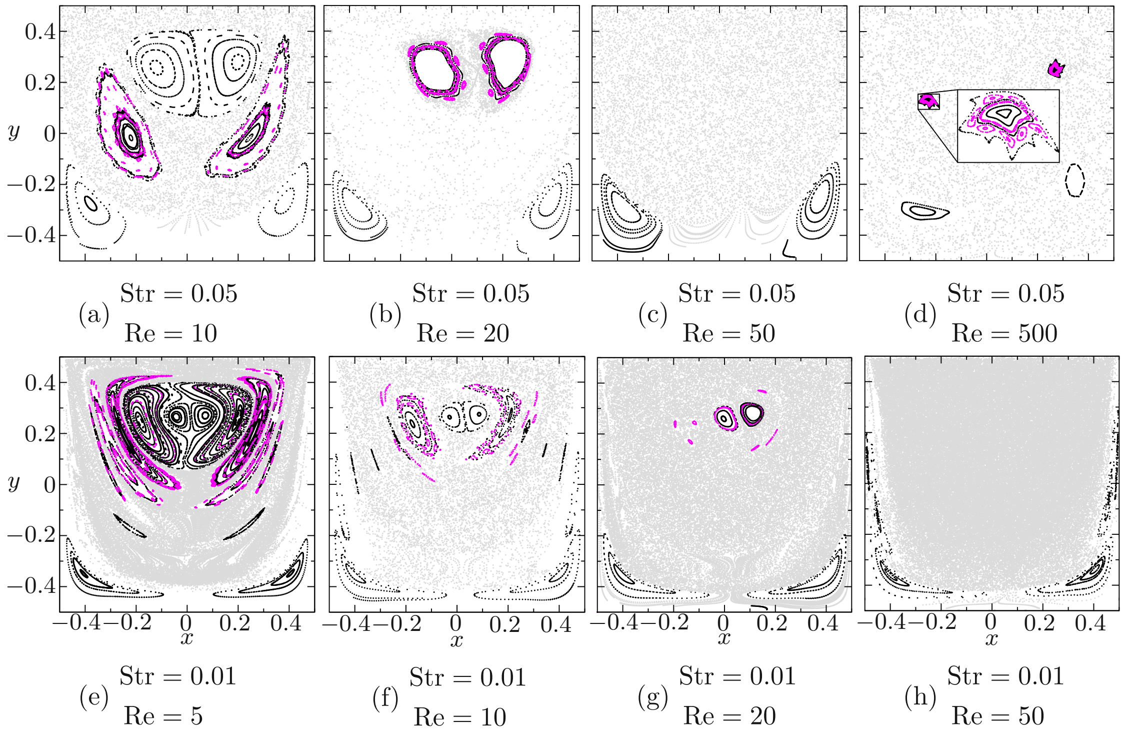

Figure 2.18: Stroboscopic projection to $t = k$. Parameters as indicated. Black, magenta and grey dots as in fig. 2.14. The initial distribution of fluid elements in (b) is concentrated near the boundaries of the upper tori, and some artifacts of the initial distribution may be visible in the chaotic sea.

As the number of sets of tori increases for Str < 0.059, we observe that the chaotic sea tends to emerge from the heteroclinic connections outlining the most stretched sets (fig. 2.18). Highly stretched tori vanish at low Reynolds numbers Re $\sim \mathcal{O}(1)$, while the "newest" tori near the center of the Eulerian vortex survive to higher Reynolds numbers Re $\sim \mathcal{O}(10)$.

Typically, the regular tori are destroyed as the Reynolds number increases. However, for Str $= 0.05$ (fig. 2.18a–d) new regular tori are born in the bulk of the chaotic sea as Re increases from 340 to 345. The structure of these tori in space and time differs qualitatively from those observed at lower Reynolds numbers, as shown in the next section.

2.4.4 Spatio-temporal structure of KAM tori

For low Reynolds numbers Re $\sim \mathcal{O}(10)$ (fig. 2.19a-c) the KAM tori have an oscillatory helical shape. For higher frequencies Str > 0.1 (fig. 2.19a,b) they only travel short distances during the oscillation cycle. The figure 2.19(a) illustrates well the reflection-translation symmetry (2.35) of the upper tori (cyan and brown). Figure 2.19(b) shows

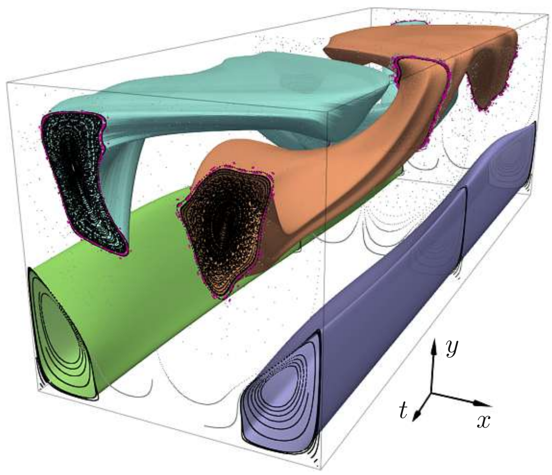

(a) Str = 0.1, Re = 20

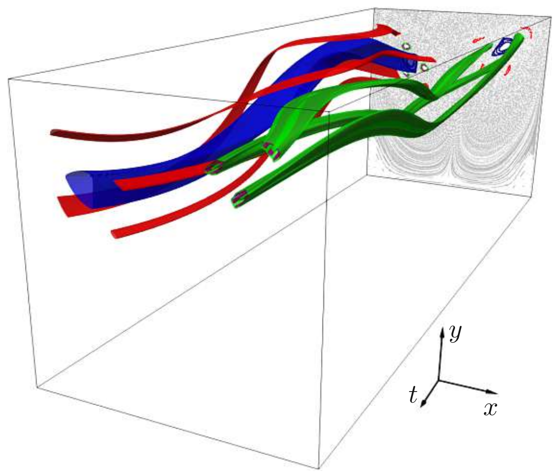

(b) Str = 0.25, Re = 50

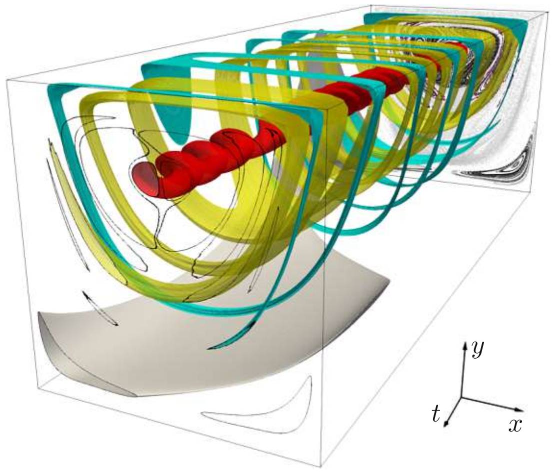

(c) Str = 0.01, Re = 5

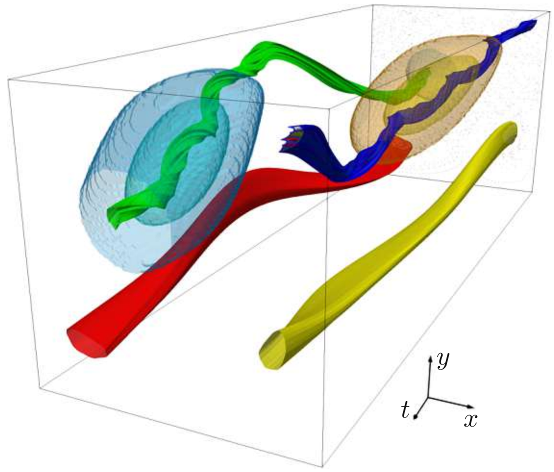

(d) Str = 0.05, Re = 500

Figure 2.19: Stroboscopic projections (dots) and outermost KAM tori (surfaces) of selected sets, for the parameters indicated in sub-captions, shown over one full period of the driving. The low-opacity surfaces in (d) represent isosurfaces of the instantaneous stream function for $\psi = \pm 0.4$ and ± 0.6. The front faces of the wire-frames correspond to the phase of the lid motion at $t = k$, $k \in \mathbb{N}$ in (a–c) and at $t = 3/2 + k$ in (d).

subharmonic tori of periods 3 (green) and 4 (red) as they wind about the synchronous tori (blue). Only one of each pair of tori is plotted for simplicity.

For low frequencies Str $\lesssim \mathcal{O}(10^{-2})$ (fig. 2.19c), the tori can make multiple revolutions about the center of the Eulerian vortex during a half-period of unidirectional lid motion. The tori close to the vortex center make more revolution than those further away. Tori get stretched when they pass close to the moving lid. Only few tori are plotted in fig. 2.19(c), which demonstrate this general behavior.

The tori observed for $\mathrm{Str} = 0.05, \mathrm{Re} = 500$ have a different structure. This is related to the different structure of the flow, which is dominated by two Eulerian vortices with opposite senses of rotation, which alternately appear and disappear in the upper part of the cavity. They are visualized by isosurfaces of the instantaneous stream function (low opacity surfaces in fig. 2.19d). They are generated near the upstream upper corner of the cavity after the lid motion changes direction and gradually move towards the center of the cavity. They vanish soon after the lid changes the direction of motion again, being replaced by the counter-rotating vortex, which is created near the opposite upper corner. Each of the upper KAM tori in fig. 2.19(d) spirals close to the center of its respective vortex for a half-period of unidirectional lid motion, and afterward, it is advected back to its starting position during the second half-period.

2.4.5 Heteroclinic connections

Next, we illustrate the emergence of chaotic trajectories by perturbation of a heteroclinic connection. Figure 2.20(a) shows an example of a regular heteroclinic connection for $\mathrm{Str} = 0.05$ and $\mathrm{Re} = 5$. A small circle of fluid elements is initiated around a hyperbolic trajectory P, approximating an outline of a blob of fluid. The outline (blue curve) is advected by the flow and adaptively refined as described in section 2.3.2. It is stretched along the unstable manifold $\mathcal{W}^{\mathrm{u}}(P)$ of the trajectory P, which coincides with the stable manifold $\mathcal{W}^{\mathrm{s}}(Q)$ of another hyperbolic trajectory Q. The outline approaches close to the trajectory Q along its stable manifold and gets stretched along the unstable manifold $\mathcal{W}^{\mathrm{u}}(Q)$. Eventually, it arrives back to the trajectory P along its stable manifold $\mathcal{W}^{\mathrm{s}}(P)$. Another small circle (outline shown in cyan) is initiated around the trajectory Q, and it is advected backward in time in order to visualize the stable manifold $\mathcal{W}^{\mathrm{s}}(Q)$. It is clear that the heteroclinic connection between P and Q is unperturbed, since $\mathcal{W}^{\mathrm{u}}(P)$ is indistinguishable from $\mathcal{W}^{\mathrm{s}}(Q)$.

Figure 2.20(b), on the other hand, shows an example of a transverse heteroclinic connection for different parameters $\mathrm{Str} = 0.02, \mathrm{Re} = 10$. Again, a small circle is initiated around a hyperbolic trajectory P. It stretches along the unstable manifold of P, which develops undulations in its upper part. The undulations are magnified when they approach another hyperbolic trajectory Q, being stretched in the directions of its unstable manifold. This example clearly illustrates the folding and stretching of fluid interfaces near the hyperbolic trajectory Q, which leads to an exponential growth of their area. The folds eventually penetrate the entire sea of chaotic trajectories.

We consider another example of transverse heteroclinic connections between different parts of a hyperbolic trajectory of higher periodicity. For $\mathrm{Str} = 0.25$ and $\mathrm{Re} = 50$ (fig. 2.20c) we find closed hyperbolic trajectories of periodicities 3 and 4 embedded in the chaotic sea. Their stable and unstable manifolds form a labyrinth called *heteroclinic tangle*. A subharmonic hyperbolic trajectory of periodicity n intersects the stroboscopic projection plane at n points, and heteroclinic connections exist between its different parts. We consider the trajectory of period 4. Its subsequent intersections with the stroboscopic projection plane $t = k$ form hyperbolic points which are denoted $\mathrm{P}_1, \ldots, \mathrm{P}_4$. The blue

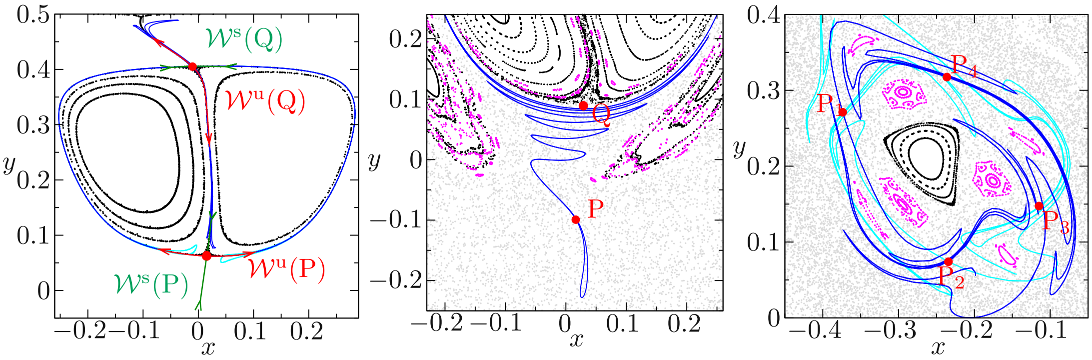

(a) Str = 0.05, Re = 5 (b) Str = 0.02, Re = 10 (c) Str = 0.25, Re = 50

Figure 2.20: Examples of heteroclinic connections. Dots are the stroboscopic projection of fluid trajectories to $\phi_0 = 0$. The blue lines in each figure represent an initially small circle about the hyperbolic point P (or P_1 in (c)) being advected and shown after 42 (a), 6 (b) and 20 (c) periods of lid motion. Cyan lines represent an initially small circle about the point Q (or P_2 in (c)) advected backward in time. In (a), stable and unstable manifolds are indicated by green and red arrows, respectively.

outline is obtained by initiating a blob at P_1, which is advected forward in time. It is stretched towards the hyperbolic points P_2 and P_4 where the outline folds. One side of the folds is stretched back to P_1 and the other towards P_3 where they fold again. The cyan outline is initiated around P_2 and advected backward in time.

2.4.6 Mixing

In the high-frequency regime $\mathrm{Str} \in \langle 0.2, 1\rangle$, there exists an optimum Reynolds number $\mathrm{Re} \in \langle 50, 100\rangle$ for fast mixing (fig. 2.21b). When the optimum value is exceeded, the thickness of the Stokes layer becomes too small, and the flow is then mostly concentrated in this thin layer close to the lid. For lower frequencies, the mixing improves with an increase of the Reynolds number. For a given Reynolds number there exists an optimum frequency, which is identified from fig. 2.21 as $\mathrm{Str} \approx 0.25$ for $\mathrm{Re} = 20$ and $\mathrm{Str} \approx 0.05$ for $\mathrm{Re} = 200$. This corresponds, respectively, to the Stokes numbers $\mathrm{St} = \mathrm{ReStr}$ of 5 and 10 and the Stokes layer thicknesses $\lambda = \mathrm{St}^{-1/2}$ of 0.45 and 0.32. The best mixing does not correlate with the largest extent of the chaotic sea, which increases when the driving frequency is decreased (fig. 2.21a).

2.5 Discussion

A lid-driven cavity with zero mean velocity of the lid is easy to construct since a rigid plate with linear driving can be employed as the lid. The simplicity of the geometry is believed to be advantageous for microfluidic applications. The structure of fluid trajectories and the mixing ability of the flow were investigated for a range of driving frequencies and

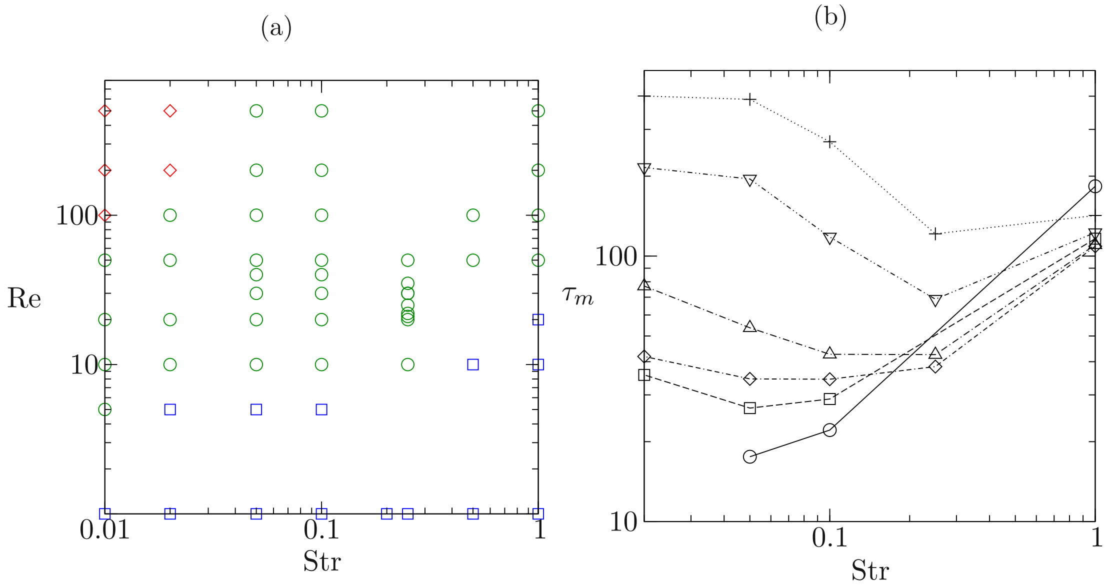

Figure 2.21: (a) Regimes of the Lagrangian topology in which only regular trajectories exist (blue squares), regular and chaotic trajectories coexist (green circles), and in which regular regions occupy less than 1% of the domain (red diamonds). (b) Dependence of the convective mixing time τ_m on the Strouhal number for different Reynolds numbers Re = 10 (···+···), Re = 20 (-·▽·-), Re = 50 (-·△-·), Re = 100 (-–◇–-), Re = 200 (- -□- -), Re = 500 (—○—) .

Reynolds numbers. The results can be utilized to design a laminar mixing device based on this setup.

Compared to the two-dimensional lid-driven cavity flow with a non-zero mean velocity of the lid oscillation (Poumaëre, 2020) we do not observe resonances of synchronous closed trajectories associated with the emergence of homoclinic connections and bifurcation of elliptic trajectories. On the other hand, we observe many heteroclinic connections for low driving frequencies, which promote the stretching of fluid.

Chaotic advection can be achieved with the present setup even for low Reynolds numbers Re $\sim \mathcal{O}(1)$ when the driving frequency is sufficiently low Str $\sim \mathcal{O}(10^{-2})$. For such low driving frequencies, the sea of chaotic trajectories spans the entire cavity when the Reynolds number is increased to Re $\sim \mathcal{O}(10^2)$. However, the large extent of the chaotic sea does not guarantee fast mixing because, for the low frequencies, long convective time is needed to complete one flow cycle. Therefore, an optimal driving frequency exists for a given Reynolds number when fast mixing is required.

When the driving frequency is too high, Str $\sim \mathcal{O}(1)$, the flow has a poor mixing ability. In the range of lower Reynolds numbers Re $\sim \mathcal{O}(10)$ the fluid trajectories tend to remain regular, while for higher Reynolds numbers Re $\sim \mathcal{O}(100)$ the flow is concentrated in a thin Stokes layer below the lid, with very weak fluid transport in the rest of the cavity. In the high-frequency regime, the Kolmogorov-Arnold-Moser tori resemble the streamlines of the mean flow. This phenomenon is attributed to short fluid trajectories within an oscillation cycle. The effect of spatial variation of the velocity field on the net transport of a fluid element after one period of oscillation decays as the frequency increases, since the element remains close to its initial location. The transport then becomes dominated by the mean velocity in this close neighborhood of the initial location.

CHAPTER 3

Linear stability analysis of thermocapillary convection in droplets adhering to a wall

The results presented in this chapter are reproduced from a manuscript
Babor, L. and Kuhlmann, H. C. (2023b), 'Linear stability of thermocapillary flow in a droplet attached to a hot or cold substrate', submitted to *Phys. Rev. Fluids* on April 26, 2023.

3.1 Introduction

3.1.1 Thermocapillarity

An interface between two immiscible or partially miscible fluids experiences a surface tension σ (see, e.g., Levic, 1962; Davis, 1987). The interface between a liquid and a gas is often called a free surface. The surface tension depends on several aspects as the local chemical concentration of both fluids, temperature, electrical fields or contamination of the interface. In this work it is assumed that both fluids, the liquid inside the droplet and the ambient gas, are chemically pure (i.e., their chemical concentrations are homogeneous), the free surface is not contaminated, and electrical field is excluded. Thus, only the temperature dependence of the surface tension $\sigma(T)$ is considered. A temperature gradient tangential to the free surface induces a gradient of surface tension

$$\nabla\sigma = -\gamma(\mathbf{I} - \boldsymbol{n} \otimes \boldsymbol{n}) \cdot \nabla\tilde{T} \tag{3.1}$$

which can drive a flow.

$$\gamma = -\frac{\mathrm{d}\sigma}{\mathrm{d}\tilde{T}} \tag{3.2}$$

is the temperature coefficient of surface tension. The thermocapillary driving of fluid flow is particularly appealing for applications in microfluidics (Karbalaei et al., 2016) and in the conditions of microgravity Salgado Sánchez et al. (2020). It can also give rise to various instabilities (Davis, 1987; Schatz and Neitzel, 2001).

For many flows of practical interest, γ can be assumed constant within a given interval of temperature variations. Thus, a linear dependence of surface tension on temperature

$$\sigma(T) = \sigma_0 - \gamma(T - T_0) \tag{3.3}$$

is assumed in the standard framework of thermocapillary flows, and the heat capacity of the free surface per unit area

$$c_\sigma = T\frac{\mathrm{d}\gamma}{\mathrm{d}T}. \tag{3.4}$$

(Schneider, 2013) is commonly neglected. This is consistent with the common assumption that other thermophysical fluid properties are constant as well. Such assumptions are typically valid for moderate temperature variations and normal fluids at temperatures sufficiently far below their critical temperature[1].

The free surface can be viewed as a heat engine that can drive a flow by converting part of the normal heat flux density into mechanical power per unit area. When no mechanical work is extracted from the flow, it is dissipated back to heat by viscosity in the bulk of the fluid. It is common to neglect both the bulk heat production per unit volume due to the viscous dissipation of momentum as well as the normal heat flux density jump at the free surface. For thermocapillary flows they both scale with $\gamma^2\Delta T^2/(\mu L^2)$, where ΔT and L are the characteristic scales of temperature variations and lengths, respectively. This is typically sufficiently small compared to the scales of convective ($\rho c_p \gamma \Delta T^2/\mu$) or conductive ($\lambda \Delta T/L$) heat flux densities, where c_p is the specific heat capacity and λ the heat conductivity of the fluid.

Under these assumptions, the normal heat flux is continuous across the free surface. The conditions of validity in terms of independent dimensionless power products are provided in sec. 3.2.1.

3.1.2 Coffee-stain effect

When a droplet on a wall evaporates in a non-equilibrium pinned-contact-line regime, a Stefan flow is induced in the bulk of the droplet, which compensates for the evaporation

[1] In this context, the *critical temperature* is defined as the temperature at which the latent heat of evaporation vanishes. The fluid cannot form a sharp interface above the critical temperature, since there is no distinction between the liquid and the gaseous phase. Even below but close to the critical temperature, thermocapillary flows cannot be analyzed by standard means due to several complications. However, in most practical situations fluids hardly achieve such high temperatures in liquid state. For example, the free surface of water would, under the standard continuum assumption, experience a negative heat capacity per unit area (Schneider, 2015) in the temperature range from 528.0 K to 647.1 K (Kalová and Mareš, 2018), where the upper bound is the critical temperature.

mass loss near the contact line to keep it pinned. The flow can transport suspended particles towards the contact line where they accumulate. This leads to non-uniform deposition of the particles during drying of the droplet known as the classical *coffee-stain effect* (Deegan et al., 1997; Larson, 2017). The coffee-stain effect is of interest in numerous fields of science and industry. While it is typically undesired in ink-jet printing (Park and Moon, 2006) and spray coating, it is finding new applications in medical diagnostics (Guha et al., 2017; Li et al., 2015) and manufacturing of conductive layers (Lian et al., 2020). A review of these and other applications is due to Zang et al. (2019).

When a temperature gradient tangential to the free surface is present, either due to the evaporation heat flux (see e.g. Bhardwaj, 2018; Kelly-Zion et al., 2018; Kumar and Bhardwaj, 2018; Semenov et al., 2017; Hu and Larson, 2002, or others) or due to a non-isothermal ambient environment, a thermocapillary flow is induced, which modifies the deposition pattern after the drying of the droplet. While the effect of a basic steady axially symmetric thermocapillary convection on the deposit has been investigated (Hu and Larson, 2006; Li et al., 2019), many experimental studies (e.g. Sefiane et al., 2008, and others) show that such flow can be unstable to three-dimensional or oscillating perturbation.

The transition to three-dimensional or time-dependent flow can be expected to affect the deposition strongly. It can even induce de-mixing and clustering of neutrally buoyant particles into accumulation structures in the bulk of the droplet, as observed by Takakusagi and Ueno (2017). The formation of particle accumulation structures (see e.g Romanò, Wu and Kuhlmann, 2019, for a review of the mechanism) is by itself a phenomenon with large practical potential. It is therefore essential to understand for which parameters the instability of the basic flow occurs.

3.1.3 State of the research

In droplets on a wall under steady axially symmetric thermocapillary driving, a steady axisymmetric basic state exists, consisting of either one or more toroidal vortices. The basic state can become unstable to three-dimensional and/or time-dependent perturbations for high Reynolds numbers due to various instability mechanisms. The richness of mechanisms is partly caused by the oblique temperature gradient with respect to the free surface, which can be dominant in either normal or tangential direction at different positions on the free surface. Thermocapillary-driven instabilities of the flow in droplets have been reported in the literature. In this study, we also find purely hydrodynamic instability of the basic axisymmetric toroidal vortex, which is very similar to that observed in low-Prandtl-number liquid bridges.

The flow instabilities driven by thermocapillarity rely on the following self-amplification (positive feedback) mechanism: The perturbation of the free-surface temperature induces a perturbation of the thermocapillary stress which drives a perturbation flow. The perturbation flow, in turn, amplifies the temperature perturbation. This type of instability therefore requires a non-zero Prandtl number, such that the perturbation flow can generate the temperature perturbation from the basic temperature gradient by convection.

Such instabilities have been originally analyzed in liquid pools (Smith and Davis, 1983; Koschmieder and Prahl, 1990; Schwabe et al., 1992; Schatz et al., 1995; Riley and Neitzel, 1998; Burguete et al., 2001; Garnier and Chiffaudel, 2001, and others). They are typically divided into two sub-classes: *thermocapillary* and *Marangoni* instabilities (Schatz and Neitzel, 2001; Davis, 1987). The former rely on the tangential, and the latter on the normal direction of the basic temperature gradient with respect to the free surface. The Marangoni instability requires the temperature gradient to be directed from the free surface into the bulk of the droplet. It manifests itself in form of Marangoni cells (Pearson, 1958), which are typically observed near the center of shallow droplets heated from the wall (Gavrilina and Barash, 2021; Shi et al., 2017; Karapetsas et al., 2012), or radial rolls, which have been observed near the contact line of shallow droplets on heated substrates with large (but finite) conductivity (Zhu and Shi, 2021, 2019; Sefiane et al., 2010). The Marangoni cells and rolls can be either steady or traveling.

The hydrothermal wave (HTW) instability, observed in droplets with higher contact angle (Watanabe et al., 2018), falls into the class of thermocapillary instabilities. It requires a thermocapillary basic flow which modifies the internal temperature gradient in the bulk of the fluid by convection. The perturbation flow generates a temperature perturbation with internal extrema. This also leads to some perturbation of the surface temperature which drives the perturbation flow by thermocapillarity. The HTW instability manifests itself in the form of a standing or traveling wave. It has been thoroughly investigated not only in liquid pools, but also in liquid bridges (Xu and Davis, 1984; Kuhlmann and Rath, 1993; Wanschura et al., 1995; Leypoldt et al., 2000; Nienhüser and Kuhlmann, 2002; Stojanović et al., 2022, and others). On the other hand, in the case of a thermocapillary droplet on a wall, the structure of the HTW is not yet fully understood.

Apart from the aforementioned instability mechanisms, which rely on the perturbation of the free-surface temperature, the basic thermocapillary flow can also lose stability due to inertia, as in isothermal flows. The inertial symmetry breaking mechanisms are operational also in the limit of vanishing Prandtl number. Inertial instabilities in low-Prandtl-number thermocapillary flows have been reported, e.g., by Kuhlmann and Rath (1993); Wanschura et al. (1995) in a liquid bridge, or by Kuhlmann and Schoisswohl (2010) in a liquid pool. To the best of the author's knowledge, inertial instabilities have not yet been reported in a droplet on a wall.

3.1.4 Stability of fluid flows

The homogeneous Navier–Stokes equations (1.1) can be viewed as a dynamical system

$$\partial_{\tilde{t}} \underbrace{\begin{pmatrix} 1 & 0 \\ 0 & 0 \end{pmatrix}}_{\boldsymbol{\mathcal{M}}} \underbrace{\begin{pmatrix} \tilde{\boldsymbol{u}} \\ \tilde{p} \end{pmatrix}}_{\boldsymbol{q}} = \underbrace{\begin{pmatrix} -(\tilde{\boldsymbol{u}} \cdot \tilde{\nabla})\tilde{\boldsymbol{u}} + \nu \tilde{\nabla} \cdot \tilde{\boldsymbol{s}} - \rho^{-1} \tilde{\nabla} \tilde{p} \\ \tilde{\nabla} \cdot \tilde{\boldsymbol{u}} \end{pmatrix}}_{\boldsymbol{\mathcal{N}}(\boldsymbol{q})}, \tag{3.5}$$

together with the boundary conditions. When the boundary conditions satisfy some symmetries, e.g., translation invariance in time ($\partial_{\tilde{t}} = 0$) or in some spatial direction, there exists a solution $\boldsymbol{q}_0$ to (3.5) which satisfies the same symmetries. $\boldsymbol{q}_0$ is called *the basic state*. In the case of time invariance $\partial_{\tilde{t}}\boldsymbol{q}_0 = 0$, the basic state is the fixed point of the dynamical system,

$$\boldsymbol{\mathcal{N}}(\boldsymbol{q}_0) = 0. \tag{3.6}$$

In what follows, we only consider the case of a steady basic state. The problem (3.6) is easier to solve numerically than (3.5). The basic state can be either *stable* or *unstable*. The stability is defined by the evolution of an initial perturbed state $\boldsymbol{q}(\tilde{t}=0) = \boldsymbol{q}_0 + \boldsymbol{q}'(\tilde{t}=0)$ according to the dynamical system (3.5) (i.e., when $\boldsymbol{q}(\tilde{t}=0)$ is used as an initial condition for (3.5)). $\boldsymbol{q}'(\tilde{t}=0)$ is a small initial perturbation. The basic state is called *stable* if the perturbed state $\boldsymbol{q}(\tilde{t})$ remains close to $\boldsymbol{q}_0$ as $\tilde{t} \to \infty$. On the other hand, it is called *unstable* when $\boldsymbol{q}(\tilde{t})$ departs from $\boldsymbol{q}_0$ and evolves into a different state. In that case, some of the symmetries of $\boldsymbol{q}_0$ can be lost in the new state. The stability of the basic state is further subdivided into several types, namely

Asymptotic stability		$\boldsymbol{q}(\tilde{t}) \to \boldsymbol{q}_0$	as $\tilde{t} \to \infty$
Lyapunov stability		$\lvert\boldsymbol{q}'(\tilde{t})\rvert \lesssim \lvert\boldsymbol{q}'(\tilde{t}=0)\rvert$	as $\tilde{t} \to \infty$
Conditional stability	$\lvert\boldsymbol{q}'(\tilde{t}=0)\rvert \le \epsilon_c \implies$	$\lvert\boldsymbol{q}'(\tilde{t})\rvert \lesssim \lvert\boldsymbol{q}'(\tilde{t}=0)\rvert$	as $\tilde{t} \to \infty$
Monotonic stability	$\dfrac{\mathrm{d}\lvert\boldsymbol{q}'(\tilde{t})\rvert}{\mathrm{d}\tilde{t}} < 0 \;\forall\tilde{t} \;\wedge$	$\boldsymbol{q}(\tilde{t}) \to \boldsymbol{q}_0$	as $\tilde{t} \to \infty$,

where ϵ_c is a positive constant.

3.1.5 Linear stability analysis

In this section it will be shown that when the initial perturbation $\boldsymbol{q}'(\tilde{t}=0)$ is infinitely small, its evolution is described by a linearized dynamical system, which implies an exponential growth or decay in time. When all infinitesimal perturbations decay exponentially, the basic state is called *linearly stable*. If there exists any infinitesimal perturbation which grows exponentially, the basic state is called *linearly unstable*.

Substitution of the decomposition $\boldsymbol{q}(\tilde{t}) = \boldsymbol{q}_0 + \boldsymbol{q}'(\tilde{t})$ into (3.5) under the assumption of a steady basic state $\partial_{\tilde{t}}\boldsymbol{q}_0 = 0$ leads to a dynamical system describing the evolution of the perturbation

$$\begin{aligned}\partial_{\tilde{t}}\boldsymbol{\mathcal{M}} \cdot (\cancel{\boldsymbol{q}_0} + \boldsymbol{q}') &= \boldsymbol{\mathcal{N}}(\boldsymbol{q}_0 + \boldsymbol{q}') \\ \partial_{\tilde{t}}\boldsymbol{\mathcal{M}} \begin{pmatrix} \boldsymbol{u}' \\ p' \end{pmatrix} &= \begin{pmatrix} -(\tilde{\boldsymbol{u}}_0 + \boldsymbol{u}') \cdot \tilde{\nabla}(\tilde{\boldsymbol{u}}_0 + \boldsymbol{u}') + \nu\tilde{\nabla} \cdot (\tilde{\boldsymbol{s}}_0 + \boldsymbol{s}') - \rho^{-1}\tilde{\nabla}(\tilde{p}_0 + p') \\ \tilde{\nabla} \cdot \tilde{\boldsymbol{u}}_0 + \tilde{\nabla} \cdot \boldsymbol{u}' \end{pmatrix},\end{aligned} \tag{3.7}$$

where $\tilde{\boldsymbol{s}}_0 = \tilde{\nabla}\tilde{\boldsymbol{u}}_0 + (\tilde{\nabla}\tilde{\boldsymbol{u}}_0)^{\mathrm{T}}$ and $\boldsymbol{s}' = \tilde{\nabla}\boldsymbol{u}' + (\tilde{\nabla}\boldsymbol{u}')^{\mathrm{T}}$. The non-linear right-hand side can be expanded in the Taylor series about $\boldsymbol{q}_0$

$$\boldsymbol{\mathcal{N}}(\boldsymbol{q}_0 + \boldsymbol{q}') = \cancelto{0}{\boldsymbol{\mathcal{N}}(\boldsymbol{q}_0)} + \underbrace{\frac{\partial\boldsymbol{\mathcal{N}}}{\partial\boldsymbol{q}_0}}_{\boldsymbol{\mathcal{A}}}(\boldsymbol{q}_0) \cdot \boldsymbol{q}' + \mathcal{O}\left((\boldsymbol{q}')^2\right), \tag{3.8}$$

where $\boldsymbol{\mathcal{A}}$ is the Jacobian of $\boldsymbol{\mathcal{N}}$. When the initial perturbation is asymptotically small, $|\boldsymbol{q}'(\tilde{t}=0)| \ll \boldsymbol{q}_0$, the higher order terms $\mathcal{O}\left((\boldsymbol{q}')^2\right)$ become negligible. The initial evolution of such small perturbation is then described by the linearized system

$$\begin{aligned} \partial_{\tilde{t}} \boldsymbol{\mathcal{M}} \cdot \boldsymbol{q}' &= \boldsymbol{\mathcal{A}}(\boldsymbol{q}_0) \cdot \boldsymbol{q}' \\ &= \begin{pmatrix} -(\tilde{\boldsymbol{u}}_0 \cdot \tilde{\nabla})\boldsymbol{u}' - (\boldsymbol{u}' \cdot \tilde{\nabla})\tilde{\boldsymbol{u}}_0 + \nu \tilde{\nabla} \cdot \boldsymbol{s}' - \rho^{-1}\tilde{\nabla} p' \\ \tilde{\nabla} \cdot \boldsymbol{u}' \end{pmatrix}. \end{aligned} \tag{3.9}$$

The perturbation satisfying (3.9) can be decomposed into normal modes

$$\boldsymbol{q}' = \sum_j \hat{\boldsymbol{q}}_j(\tilde{\boldsymbol{x}}_n) \exp(\eta_j \tilde{t} + \mathrm{i} k_h \tilde{x}_h) + \text{c.c.} \tag{3.10}$$

The index j enumerates the modes $\hat{\boldsymbol{q}}_j$ with the complex temporal exponents $\eta_j = \varsigma_j + \mathrm{i}\tilde{\omega}_j$, where $\varsigma_j \in \mathbb{R}$ is the growth rate and $\tilde{\omega}_j \in \mathbb{R}$ is an oscillation frequency. $\tilde{\boldsymbol{x}}_n$ is a position vector in the non-homogeneous directions, while the repeated index h implies summation over the homogeneous directions - i.e., those directions in which the problem is translation invariant. $k_h \in \mathbb{R}$ is a wave number of the modes in the corresponding homogeneous direction. When the domain is periodic in the homogeneous direction with some period L_h, then the wave number is restricted to discrete values $k_h = m_h 2\pi / L_h$, where $m_h \in \mathbb{Z}$. For example, in a cylindrical coordinate system when the problem is invariant in the azimuthal direction ϕ, $L_\phi = 2\pi$. The complex conjugate "c.c." ensures that the perturbation is real. The modes do not interact, and each individually satisfies the problem (3.9) due to its linearity.

Substitution of the normal mode Ansatz (3.10) with specified wave numbers k_h into (3.9) and expressing the derivatives $\partial_{\tilde{t}} \boldsymbol{q}'$ and $\partial_{\tilde{\boldsymbol{x}}_h} \boldsymbol{q}'$ analytically leads to a linear system of PDEs

$$\eta \boldsymbol{\mathcal{M}} \hat{\boldsymbol{q}} = \boldsymbol{\mathcal{A}} \hat{\boldsymbol{q}} \tag{3.11}$$

for each mode $\hat{\boldsymbol{q}}_j$ and its complex growth rate η_j. The system can be discretized in the non-homogeneous directions to obtain a generalized eigenproblem

$$\eta \boldsymbol{M} \hat{q}_i = \boldsymbol{A} \hat{q}_i \tag{3.12}$$

where the eigenvector $\hat{q}_i$ contains the values at the grid points (enumerated by i) of a given mode, and the linear differential operator $\boldsymbol{\mathcal{A}}$ is approximated numerically with a discretization matrix $\boldsymbol{A}$. The mass matrix $\boldsymbol{M}$ is the discrete version of $\boldsymbol{\mathcal{M}}$, which in the case of the linearized Navier–Stokes equations acts as an identity matrix on the nodal values of velocity and as a zero matrix on the nodal values of pressure.

Only the eigenvector corresponding to the largest growth rate ς is of interest in the context of linear stability analysis. It is called *the most dangerous mode*. As long as the real parts ς of all eigenvalues η are negative, the basic state is linearly stable. If at least one eigenvalue has a positive real part, the corresponding mode will grow exponentially, and the basic state is linearly unstable. Thus, we order the growth rates such that $\varsigma_1 > \varsigma_2 > \varsigma_3 > \dots$ and consider only the leading growth rates and their associated modes.

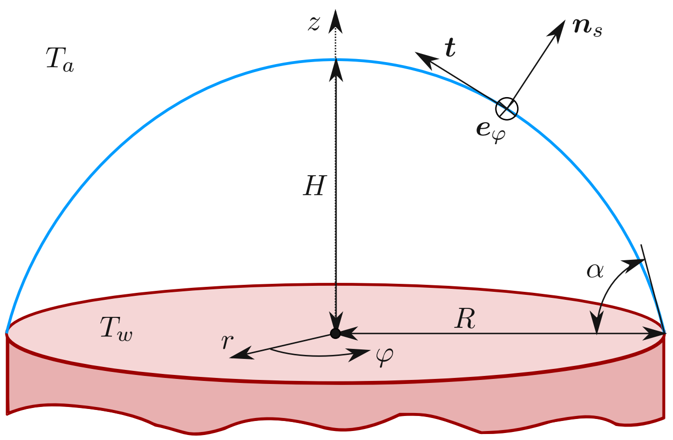

Figure 3.1: Sketch of the flow geometry - the sessile droplet with a spherical free surface (blue). The origin of the cylindrical coordinate system (r, ϕ, z) is located at the center of the droplet base. $\boldsymbol{n}$, $\boldsymbol{t}_{rz}$ and $\boldsymbol{e}_\phi$ are the surface normal and the surface tangent vectors.

3.2 Problem formulation

This chapter considers the flow inside a sessile liquid droplet (fig. 3.1) of a given wetting radius R and contact angle α on a perfectly conducting substrate with a fixed temperature T_w. The liquid is assumed to be non-volatile in the ambient gas, which has a uniform far-field temperature $T_a \neq T_w$. The temperature gradient within the droplet arises due to the heat transfer between its free surface Γ_s and the ambient gas, which is modeled by Newton's law of cooling

$$\tilde{q}(\tilde{\boldsymbol{x}}) = -\lambda_g \tilde{\nabla} T_g(\tilde{\boldsymbol{x}}) \approx h\left[\tilde{T}(\tilde{\boldsymbol{x}}) - T_a\right], \quad \tilde{\boldsymbol{x}} \in \Gamma_s, \tag{3.13}$$

where $\tilde{q}$ is the heat flux in the direction of the outward-pointing normal, λ_g is the thermal conductivity of the ambient gas, T_g is its local temperature, the parameter h is the heat transfer coefficient, and $\tilde{T}$ is the local temperature of the liquid. Due to the non-volatility, there is no additional heat and mass flux at the free surface due to phase change. The continuity of the normal heat flux at the free surface reads

$$\lambda \tilde{\nabla} \tilde{T} = -\tilde{q}, \tag{3.14}$$

where λ is the thermal conductivity of the liquid. The distribution of temperature within the droplet is governed by the conservation of energy. For an incompressible flow (1.1b), and when the heat production due to viscous dissipation of kinetic energy is neglected, the energy equation in differential form simplifies to a convection-diffusion transport of heat

$$\rho c_p (\partial_{\tilde{t}} + \tilde{\boldsymbol{u}} \cdot \tilde{\nabla}) \tilde{T} = \lambda \tilde{\nabla}^2 \tilde{T}, \tag{3.15}$$

where c_p is the specific heat capacity.

The thermocapillary driving of the flow occurs through the balance of tangential forces at the free surface, namely of the viscous shear stress and the thermocapillary stress (Levic, 1962)

$$\mu \boldsymbol{t}_{rz} \cdot (\boldsymbol{n} \cdot \tilde{\boldsymbol{s}}) = \boldsymbol{t}_{rz} \cdot \tilde{\nabla}\sigma \equiv -\gamma \boldsymbol{t}_{rz} \cdot \tilde{\nabla}\tilde{T} \qquad \text{at } \Gamma_s, \tag{3.16}$$

$$\mu \boldsymbol{e}_{\phi} \cdot (\boldsymbol{n} \cdot \tilde{\boldsymbol{s}}) = \boldsymbol{e}_{\phi} \cdot \tilde{\nabla}\sigma \equiv -\gamma \boldsymbol{e}_{\phi} \cdot \tilde{\nabla}\tilde{T} \qquad \text{at } \Gamma_s, \tag{3.17}$$

where $\gamma = -\mathrm{d}\sigma/\mathrm{d}\tilde{T}$ is the temperature coefficient of surface tension. The effect of the shear stress from the outer gas is neglected under the assumption that the viscosity of the gas is much smaller than the viscosity of the liquid $\mu_g/\mu \ll 1$. The balance of normal forces, on the other hand, determines the shape of the droplet. See, e.g., eqs. (2.7) or (2.22) of Kuhlmann (1996) for a full force balance at the free surface in dimensional or dimensionless form, respectively. In the absence of flow, the normal force balance is expressed by the Young-Laplace (Young, 1805; Laplace, 1806) equation

$$\Delta\tilde{p} = \sigma\tilde{\nabla} \cdot \boldsymbol{n}, \tag{3.18}$$

where $\Delta\tilde{p}$ is the pressure drop across the free surface and $\tilde{\nabla} \cdot \boldsymbol{n}$ is the local curvature. In the absence of flow and gravity, the pressure distribution in the liquid and the gas is uniform, leading to a constant pressure jump Δp_0. For an isothermal free surface (with constant surface tension) this leads to a constant surface curvature. A non-zero acceleration of gravity $\boldsymbol{g}$ induces a hydrostatic pressure

$$\Delta p_h = -(\rho - \rho_g)\boldsymbol{g} \cdot (\tilde{\boldsymbol{x}} - \tilde{\boldsymbol{x}}_0), \tag{3.19}$$

where ρ_g is the density of the outer gas and $\boldsymbol{x}_0$ is a reference location of zero hydrostatic pressure drop. This causes a *static surface deformation*. Furthermore, a non-uniform temperature of the free surface causes a variation of $\sigma(T)$ in (3.18), and the flow in the droplet exerts an additional *dynamic* normal stress

$$\Delta p_d = \tilde{p} - \boldsymbol{n} \cdot \tilde{\boldsymbol{s}} \cdot \boldsymbol{n} \tag{3.20}$$

on the free surface, where $\tilde{p}$ is the flow-induced pressure distribution relative to the state without flow. These two effects lead to a *dynamic surface deformation*. The overall normal stress balance at the free surface reads

$$\Delta p_0 + \Delta p_h + \Delta p_d = \sigma(T)\tilde{\nabla} \cdot \boldsymbol{n}. \tag{3.21}$$

In the present model, both the static and the dynamic surface deformations are neglected, such that the free surface is spherical and indeformable. This simplification applies to small Bond and capillary numbers, as described in section 3.2.1.

Since a constant density of the liquid is considered in this work, there is no buoyancy that would affect the flow. Although, in general, the density would be (at least) temperature dependent, it is assumed here that buoyancy is negligible compared to thermocapillary driving. In order to justify this assumption and define the conditions of its validity, we consider the Boussinesq approximation, which for small density variations models the effect of buoyancy with a bulk force term

$$\tilde{\boldsymbol{f}} = -\beta \boldsymbol{g}(\tilde{T} - T_0), \tag{3.22}$$

where $\beta = -(\mathrm{d}\rho/\mathrm{d}\tilde{T})/\rho(T_0)$ is the thermal expansion coefficient of the liquid and T_0 is a reference temperature. Accordingly, the scale of the buoyant force per unit mass is proportional to $\beta|\boldsymbol{g}|\Delta T$, where $\Delta T = |T_w - T_a|$ is the scale of temperature variations. On the other hand, the thermocapillary force per unit mass scales with $\gamma\Delta T/(\rho R^2)$. As the ratio of buoyant to thermocapillary forces $\rho\beta|\boldsymbol{g}|R^2/\gamma$ is proportional to R^2, it is typically small for small droplets.

3.2.1 Dimensional analysis

The reference physical parameters relevant for this problem are summarized in table 3.1 with their units indicated in the SI system. It lists 14 parameters, and the rank of the dimension matrix is 4. Thus, according to the Buckingham Π theorem, the problem depends on 10 independent dimensionless power products. We want to define these power products in terms of the characteristic scales of the problem. The wetting radius is selected for the length scale, $L := R$. Furthermore, the thermocapillary velocity scale $U := \gamma\Delta T/\mu$ is employed. The dimensionless power products are

$$\begin{aligned}
&\text{aspect ratio} && \Gamma = \frac{H}{R} = \tan\left(\alpha - \frac{\pi}{2}\right) + \frac{1}{\cos\left(\alpha - \frac{\pi}{2}\right)} \\
&\text{Reynolds number} && \mathrm{Re} = \frac{\rho U L}{\mu} = \frac{\rho\gamma\Delta T R}{\mu^2} \\
&\text{Prandtl number} && \mathrm{Pr} = \frac{\mu c_p}{\lambda} \\
&\text{Biot number} && \mathrm{Bi} = \frac{hR}{\lambda} \\
&\text{Grashof number} && \mathrm{Gr} = \frac{g\rho^2\beta\Delta T R^3}{\mu^2} \\
&\text{Bond number} && \mathrm{Bo} = \frac{\rho g R^2}{\sigma_0} \\
&\text{Capillary number} && \mathrm{Ca} = \frac{\gamma\Delta T}{\sigma_0} \\
&\text{Brinkman number} && \mathrm{Br} = \frac{\mu U^2}{\lambda\Delta T} = \frac{\gamma^2\Delta T}{\mu\lambda} \\
& && N_1 = \frac{|c_\sigma(T_0)|U}{\lambda} = \frac{|c_\sigma(T_0)|\gamma\Delta T}{\mu\lambda} \\
& && N_3 = \frac{|c_\sigma(T_0)|R\tilde{\omega}}{2\pi\lambda},
\end{aligned}$$

where H is the height of the droplet, $\tilde{\omega}$ is the oscillation frequency of the perturbation, and N_1 and N_3 are due to Schneider (2013).

	ρ	μ	$\lvert\boldsymbol{g}\rvert$	ΔT	c_p	λ	σ_0	γ	R	H	h	β	$c_\sigma(T_0)$	$\tilde{\omega}$
kg	1	1	0	0	0	1	1	1	0	0	1	0	1	0
m	-3	-1	1	0	2	1	0	0	1	1	0	0	0	0
s	0	-1	-2	0	-2	-3	-2	-2	0	0	-3	0	-2	-1
K	0	0	0	1	-1	-1	0	-1	0	0	-1	-1	-1	0

Table 3.1: Dimension matrix of the problem. H is the height of the droplet, and $\tilde{\omega}$ is the oscillation frequency of the perturbation.

	ρ	μ	$\lvert\boldsymbol{g}\rvert$	ΔT	c_p	λ	σ_0
	kg m^{-3}	Pa s	m s^{-2}	K	J kg^{-1} K^{-1}	W m^{-1} K^{-1}	N m^{-1}
(a)	912	4.56×10^{-3}	9.81	40	1.8×10^3	0.12	1.97×10^{-2}
(b)	789	1.095×10^{-3}	9.81	5	2.845×10^3	0.14	2.2×10^{-2}

	γ	R	β	$\tilde{\omega}$
	N m^{-1} K^{-1}	m	K^{-1}	rad s^{-1}
(a)	6.37×10^{-5}	1.5×10^{-3}	1.09×10^{-3}	2π
(b)	8.36×10^{-5}	1.5×10^{-3}	1.074×10^{-3}	

Table 3.2: Typical experimental conditions according to Takakusagi and Ueno (2017) for a silicon oil (a) and Brutin, Sobac, Rigollet and Le Niliot (2011) for ethanol (b). The remaining fluid properties which are not provided by the authors are taken from the datasheet of the KF96L-5cs silicone oil, and from Kleiber and Joh (2010), respectively.

Identification of relevant groups and related simplifications

In order to motivate the simplifications employed in this study, let us substitute some realistic values for the parameters listed in tab. 3.1. Consider, e.g., the typical experimental conditions of Takakusagi and Ueno (2017) or Brutin, Sobac, Rigollet and Le Niliot (2011) listed in tab. 3.2. In order to compute the heat capacity $c_\sigma = -T\sigma''(T)$ of the free surface per unit area, the second derivative of σ with respect to T is required. In case of ethanol we differentiate the empirical formula (6) on page 301 of Kleiber and Joh (2010) to obtain $c_\sigma^{\text{ethanol}}(T = 25°C) = 2.719 \times 10^{-5}$ J m^{-2} K^{-1}. In the case of the silicon oil there is, unfortunately, not enough data on the temperature dependence of surface tension to accurately compute c_σ.

The Brinkman number represents the ratio of viscous dissipation to thermal conduction. Since the viscous heat production is neglected in (3.15), it is only valid for $\mathrm{Br} \ll 1$. For the experimental conditions of Takakusagi and Ueno (2017) and Brutin, Sobac, Rigollet and Le Niliot (2011), $\mathrm{Br} = 3 \times 10^{-4}$ and $\mathrm{Br} = 2.3 \times 10^{-4}$, respectively.

As mentioned before, the buoyant force (3.22) is neglected as well, corresponding to a small ratio of Grashof to capillary Reynolds number $\mathrm{Gr}/\mathrm{Re} \ll 1$. This is typically valid for very small droplets or low gravity. For the exemplary parameters, $\mathrm{Gr}/\mathrm{Re} = 0.34$ and 0.22, which is still rather too large for the buoyancy force to be neglected. This analysis, therefore, applies either to even smaller droplets, fluids with smaller values of $\rho\beta/\gamma$, or to microgravity conditions (Watanabe et al., 2018). It is, however, expected that the results of this work remain at least qualitatively valid also for the millimeter-sized droplets of low-viscosity silicon oil under terrestrial gravity.

Once the buoyancy is neglected, it is, under similar arguments, consistent to also neglect static surface deformation. The importance of the static surface deformation is expressed by the Bond number $\mathrm{Bo} = \mathrm{Gr}/\mathrm{Re} \times \gamma/(\sigma_0\beta)$. The value of $\mathrm{Bo} = 1.02$ leads to a visible static deformation of the free surface (Takakusagi and Ueno, 2017), compared to a spherical shape. For the conditions of Brutin, Sobac, Rigollet and Le Niliot (2011), $\mathrm{Bo} = 0.79$. Nevertheless, the static deformation is neglected in this study, which limits its validity to reduced gravity, sub-millimeter droplets or fluids with larger ratio of surface tension to density.

Furthermore, it is assumed that the variations of the surface tension are small compared to its mean value, $\mathrm{Ca} \ll 1$. This allows to neglect dynamic surface deformations (Kuhlmann, 1999; Kuhlmann and Nienhüser, 2002) and thus, the droplet has the shape of a perfect spherical cap. The free surface then acts as an indeformable impenetrable boundary. For the exemplary parameters, $\mathrm{Ca} = 0.13$ and 0.02.

The validity of the approximation of continuous heat flux across the free surface further requires $N_1 \ll 1$ and also $N_3 \ll 1$ in case of a time-dependent perturbation (Schneider, 2013). Substituting the values from the second row of tab. 3.2 together with the value of c_σ for ethanol we obtain $N_1 = 7.4 \times 10^{-5}$ and $N_3 = 4.6 \times 10^{-8}\mathrm{s} \;\times \tilde{\omega}$. The heat flux can thus be assumed continuous up to oscillation frequencies of $\mathcal{O}(10^7\mathrm{s}^{-1})$.

3.2.2 Nondimensional governing equations

Scaling the problem as follows

$$\boldsymbol{x} = \frac{\tilde{\boldsymbol{x}}}{R}, \qquad T = \frac{\tilde{T} - T_a}{\Delta T}, \qquad \boldsymbol{u} = \frac{\tilde{\boldsymbol{u}}}{\nu/R}, \qquad t = \frac{\tilde{t}}{R^2/\nu}, \qquad p = \frac{R^2}{\rho\nu^2}\tilde{p},$$

the dimensionless form of the governing equations (1.1,3.15) is obtained as

$$(\partial_t + \boldsymbol{u}\cdot\boldsymbol{\nabla})\boldsymbol{u} = -\boldsymbol{\nabla}p + \boldsymbol{\nabla}\cdot\underbrace{(\nabla\boldsymbol{u} + \nabla\boldsymbol{u}^T)}_{\boldsymbol{S}}, \tag{3.23a}$$

$$\boldsymbol{\nabla}\cdot\boldsymbol{u} = 0, \tag{3.23b}$$

$$(\partial_t + \boldsymbol{u}\cdot\boldsymbol{\nabla})T = \frac{1}{\mathrm{Pr}}\nabla^2 T. \tag{3.23c}$$

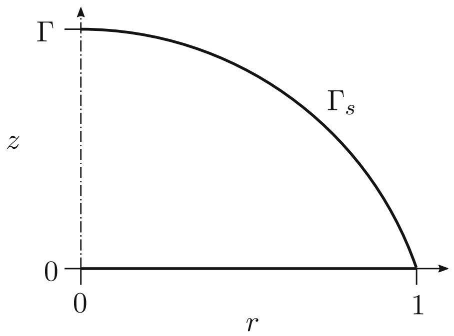

Figure 3.2: Scaled computational domain

The solution on the domain shown in fig. 3.2 must satisfy the following boundary conditions

$$\boldsymbol{u} = 0,\ T = \pm 1 \qquad \text{at } z = 0, \tag{3.24a}$$
$$\partial_\phi \boldsymbol{u} = \partial_\phi p = \partial_\phi T = 0 \qquad \text{at } r = 0, \tag{3.24b}$$
$$\boldsymbol{n} \cdot \boldsymbol{u} = 0 \qquad \text{at } \Gamma_s, \tag{3.24c}$$
$$\boldsymbol{n} \cdot \nabla T = -\mathrm{Bi}\, T \qquad \text{at } \Gamma_s, \tag{3.24d}$$
$$\boldsymbol{t}_{rz} \cdot (\mathbf{s} \cdot \boldsymbol{n}) = -\mathrm{Re}\, \boldsymbol{t}_{rz} \cdot \boldsymbol{\nabla} T \qquad \text{at } \Gamma_s, \tag{3.24e}$$
$$\boldsymbol{e}_\phi \cdot (\mathbf{s} \cdot \boldsymbol{n}) = -\mathrm{Re}\, \boldsymbol{e}_\phi \cdot \boldsymbol{\nabla} T \qquad \text{at } \Gamma_s, \tag{3.24f}$$

where Γ_s denotes the free surface and the sign $\pm$ corresponds to a heated or cooled substrate.

Unless stated otherwise, we fix the Biot number to $\mathrm{Bi} = 0.2362$, which is a realistic value for small droplets ($R \sim \mathcal{O}(10^{-3}\mathrm{m})$) of silicon oils ($k \sim \mathcal{O}(10^{-1}\mathrm{W/m\,K})$) and heat transfer coefficients $h \sim \mathcal{O}(10^{1}\mathrm{W/m^2K})$. This particular value was selected as an approximation of the conditions employed by Shi et al. (2017).

3.2.3 Basic state

As the problem definition (3.23,3.24) is invariant with respect to translation in t and ϕ, the problem admits a steady ($\partial_t = 0$) axially symmetric ($\partial_\phi = 0$) basic state $(\boldsymbol{u}_0, p_0, T_0)$. Substitution to (3.23) provides a system of steady two-dimensional equations

$$(\boldsymbol{u}_0 \cdot \boldsymbol{\nabla})\boldsymbol{u}_0 = -\boldsymbol{\nabla} p_0 + \boldsymbol{\nabla} \cdot \underbrace{(\nabla \boldsymbol{u}_0 + \nabla \boldsymbol{u}_0^T)}_{\boldsymbol{s}_0}, \tag{3.25a}$$
$$\boldsymbol{\nabla} \cdot \boldsymbol{u}_0 = 0, \tag{3.25b}$$
$$(\boldsymbol{u}_0 \cdot \boldsymbol{\nabla}) T_0 = \frac{1}{\mathrm{Pr}} \nabla^2 T_0. \tag{3.25c}$$

The force balance at the free surface in the azimuthal direction (3.24f) is then satisfied identically, and the uniqueness of the solution at the axis (3.24b) reduces to a symmetry condition

$$u_{0,r} = \partial_r u_{0,z} = \partial_r p_0 = \partial_r T_0 = 0 \qquad \text{at } r = 0, \tag{3.26}$$

where $\boldsymbol{u}_0 = u_{0,r}(r,z)\boldsymbol{e}_r + u_{0,z}(r,z)\boldsymbol{e}_z$. The azimuthal component of velocity in the basic state is zero. Since the numerical solution of (3.25) only requires two-dimensional spatial discretization, it is much less computationally demanding than solving the three-dimensional time-dependent problem (3.23).

3.2.4 Linear stability

Once the basic state is found, its linear stability with respect to three-dimensional time-dependent perturbation $(\boldsymbol{u}', p', T')$ is investigated. Substituting the decomposition

$$\begin{pmatrix} \boldsymbol{u} \\ p \\ T \end{pmatrix} (r,\phi,z,t) = \begin{pmatrix} \boldsymbol{u}_0 \\ p_0 \\ T_0 \end{pmatrix} (r,z) + \begin{pmatrix} \boldsymbol{u}' \\ p' \\ T' \end{pmatrix} (r,\phi,z,t) \tag{3.27}$$

into (3.23) and linearizing it about the basic state, a system of PDEs for the perturbation is obtained as

$$\partial_t \boldsymbol{u}' + (\boldsymbol{u}_0 \cdot \nabla)\boldsymbol{u}' + (\boldsymbol{u}' \cdot \nabla)\boldsymbol{u}_0 = -\nabla p' + \nabla \cdot \boldsymbol{s}' \tag{3.28a}$$

$$\nabla \cdot \boldsymbol{u}' = 0 \tag{3.28b}$$

$$\partial_t T' + \boldsymbol{u}_0 \cdot \nabla T' + \boldsymbol{u}' \cdot \nabla T_0 = \frac{1}{\mathrm{Pr}} \nabla^2 T' \tag{3.28c}$$

with the boundary conditions (3.24). The normal mode Ansatz for the perturbation reads

$$\begin{pmatrix} \boldsymbol{u}' \\ p' \\ T' \end{pmatrix} (r,\phi,z,t) = \begin{pmatrix} \hat{\boldsymbol{u}} \\ \hat{p} \\ \hat{T} \end{pmatrix} (r,z) \exp(\eta t + \mathrm{i} m \phi) + \text{c.c.} \tag{3.29}$$

where $m \in \mathbb{N}_0$ is the azimuthal wave number. Substituting the Ansatz (3.29) in (3.28) and expressing the derivatives ∂_t and ∂_ϕ we obtain the equations for the modes

$$\begin{aligned}
\eta\hat{u}_r =& -(u_{0,r}\partial_r + u_{0,z}\partial_z)\hat{u}_r && -(\hat{u}_r\partial_r + \hat{u}_z\partial_z)u_{0,r} - \partial_r\hat{p} \\
&+ \left(2\partial_{rr} + \frac{2}{r}\partial_r - \frac{m^2+2}{r^2} + \partial_{zz}\right)\hat{u}_r + \left(\frac{\mathrm{i}m}{r}\partial_r - \frac{3\mathrm{i}m}{r^2}\right)\hat{u}_\phi + \partial_{rz}\hat{u}_z && \qquad (3.30a)\\
\eta\hat{u}_\phi =& -(u_{0,r}\partial_r + u_{0,z}\partial_z)\hat{u}_\phi && -\frac{u_{0,r}\hat{u}_\phi}{r} - im\hat{p} \\
&+ \left(\partial_{rr} + \frac{1}{r}\partial_r - \frac{2m^2+1}{r^2} + \partial_{zz}\right)\hat{u}_\phi + \left(\frac{\mathrm{i}m}{r}\partial_r + \frac{3\mathrm{i}m}{r^2}\right)\hat{u}_r + \frac{\mathrm{i}m}{r}\partial_z\hat{u}_z && \qquad (3.30b)\\
\eta\hat{u}_z =& -(u_{0,r}\partial_r + u_{0,z}\partial_z)\hat{u}_z && -(\hat{u}_r\partial_r + \hat{u}_z\partial_z)u_{0,z} - \partial_z\hat{p} \\
&+ \left(\partial_{rr} + \frac{1}{r}\partial_r - \frac{m^2}{r^2} + 2\partial_{zz}\right)\hat{u}_z && + \left(\partial_{rz} + \frac{1}{r}\partial_z\right)\hat{u}_r + \frac{\mathrm{i}m}{r}\partial_z\hat{u}_\phi \qquad (3.30c)\\
0 =& \partial_r\hat{u}_r + \frac{\hat{u}_r}{r} + \frac{im}{r}\hat{u}_\phi + \partial_z\hat{u}_z && \qquad (3.30d)\\
\eta\hat{T} =& -(u_{0,r}\partial_r + u_{0,z}\partial_z)\hat{T} && -(\hat{u}_r\partial_r + \hat{u}_z\partial_z)T \\
&+ \frac{1}{\mathrm{Pr}}\left(\partial_{rr} + \frac{1}{r}\partial_r - \frac{m^2}{r^2} + \partial_{zz}\right)\hat{T}. && \qquad (3.30e)
\end{aligned}$$

Boundary conditions on the axis

The perturbation velocity in general consists of three velocity components, $\hat{\boldsymbol{u}} = \hat{u}_r\boldsymbol{e}_r + \hat{u}_\phi\boldsymbol{e}_\phi + \hat{u}_z\boldsymbol{e}_z$. For $m = 0$ the perturbation is axially symmetric, $\partial_\phi(\boldsymbol{u}', p', T') = 0$, and thus the symmetry condition (3.26) is prescribed for the modes at the axis. The azimuthal component of velocity then vanishes. For $m > 0$, the uniqueness of the scalar perturbation fields

$$\partial_\phi p' = \partial_\phi T' = 0 \qquad \text{at } r = 0 \tag{3.31}$$

requires

$$\hat{p} = \hat{T} = 0 \qquad \text{at } r = 0. \tag{3.32}$$

Noting that

$$\partial_\phi\boldsymbol{e}_r = \boldsymbol{e}_\phi, \qquad \partial_\phi\boldsymbol{e}_\phi = -\boldsymbol{e}_r, \tag{3.33}$$

the azimuthal derivative of the velocity vector expands as

$$\begin{aligned}
\partial_\phi\boldsymbol{u} &= (\partial_\phi u_r)\boldsymbol{e}_r + u_r\boldsymbol{e}_\phi + (\partial_\phi u_\phi)\boldsymbol{e}_\phi - u_\phi\boldsymbol{e}_r + \partial_\phi u_z\boldsymbol{e}_z \\
&= (\partial_\phi u_r - u_\phi)\boldsymbol{e}_r + (u_r + \partial_\phi u_\phi)\boldsymbol{e}_\phi + \partial_\phi u_z\boldsymbol{e}_z \qquad \stackrel{!}{=} 0 \text{ at } r = 0.
\end{aligned} \tag{3.34}$$

The axis condition for $\hat{u}_z$ is then the same as for the scalar fields

$$\text{for } m > 0, \qquad \hat{u}_z = 0 \qquad \text{at } r = 0. \tag{3.35}$$

For the radial and azimuthal component of velocity, the axis condition reads

$$\partial_\phi u_r - u_\phi = 0 \tag{3.36a}$$
$$\partial_\phi u_\phi + u_r = 0. \tag{3.36b}$$

Differentiation of (3.36a) with respect to ϕ and substitution from (3.36b) leads to a condition for the radial component

$$\partial_\phi^2 u_r + u_r = 0, \tag{3.37}$$

while differentiation of (3.36b) and substitution from (3.36a) provides a condition for the azimuthal component

$$\partial_\phi^2 u_\phi + u_\phi = 0. \tag{3.38}$$

The perturbation velocity components must satisfy these boundary conditions at $r = 0$. Substituting the normal mode Ansatz and canceling the common factor $\exp(\eta t + \mathrm{i} m\phi)$ we obtain

$$-m^2\Re(\hat{u}_r)\cos m\phi + m^2\Im(\hat{u}_r)\sin m\phi + \Re(\hat{u}_r)\cos m\phi - \Im(\hat{u}_r)\sin m\phi = 0, \tag{3.39a}$$
$$-m^2\Re(\hat{u}_\phi)\cos m\phi + m^2\Im(\hat{u}_\phi)\sin m\phi + \Re(\hat{u}_\phi)\cos m\phi - \Im(\hat{u}_\phi)\sin m\phi = 0. \tag{3.39b}$$

For $m \neq 1$ and $\phi \in \langle 0, 2\pi\rangle$ this can only be satisfied if

$$\hat{u}_r = \hat{u}_\phi = 0. \tag{3.40}$$

In the case of $m = 1$, (3.39) is satisfied identically and thus a non-zero velocity vector perpendicular to the axis, $\boldsymbol{u}(r = 0, z) = u_r \boldsymbol{e}_r + u_\phi \boldsymbol{e}_\phi$, is admissible. In order to obtain boundary conditions for $\hat{u}_r$ and $\hat{u}_\phi$ we substitute (3.35) and (3.36b) into the continuity equation (3.28b) at $r = 0$ for $m = 1$

$$\nabla \cdot \boldsymbol{u}'(r=0,z) \equiv \left(\partial_r + \frac{1}{r}\right) u_r' + \frac{1}{r}\underbrace{\partial_\phi u_\phi'}_{-u_r'\ (3.36b)} + \partial_z \cancelto{0\ (3.35)}{u_z'}$$
$$= \partial_r u_r' + \frac{1}{\cancel{r}}\cancel{u_r'} - \frac{1}{\cancel{r}}\cancel{u_r'} \overset{(3.28b)}{\Longrightarrow} \partial_r \hat{u}_r \overset{!}{=} 0. \tag{3.41a}$$

Next we differentiate (3.36a) with respect to r to obtain

$$\partial_\phi \cancelto{0\ (3.41a)}{\partial_r u_r} - \partial_r u_\phi' = 0 \implies \partial_r \hat{u}_\phi = 0 \tag{3.41b}$$

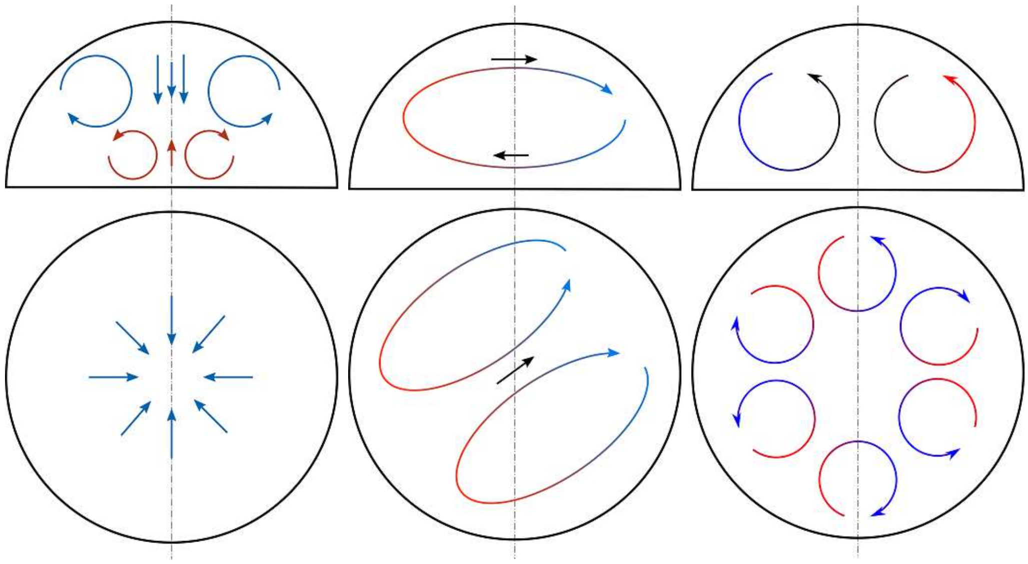

(a) $m = 0$ (b) $m = 1$ (c) $m > 1$

Figure 3.3: Sketch of some possible structures of the normal modes for different wave numbers indicated in the sub-captions. Arrows indicate the flow direction, and their color indicates temperature. The bottom row illustrates a top view of the velocity and temperature at the free surface, while the top row corresponds to a cut in a plane $\phi = \text{const}$.

at $r = 0$ for $m = 1$. Finally, we can summarize the axis boundary conditions at $r = 0$ for the modes as follows

$$\begin{aligned} &\text{for } m = 0 && \hat{u}_r = \hat{u}_\phi = \partial_r \hat{u}_z = \partial_r \hat{p} = \partial_r \hat{T} = 0 \\ &\text{for } m = 1 && \partial_r \hat{u}_r = \partial_r \hat{u}_\phi = \hat{u}_z = \hat{p} = \hat{T} = 0 \\ &\text{for } m > 1 && \hat{u}_r = \hat{u}_\phi = \hat{u}_z = \hat{p} = \hat{T} = 0 \end{aligned}$$

Examples of the structure of modes admitted by these boundary conditions are illustrated in fig. 3.3.

Non-integrable singularity on the axis for $m = 1$

The system (3.30) contains terms proportional to $1/r^2$, which present a non-integrable singularity at $r = 0$, unless they multiply a field that vanishes at the axis. The problematic terms are

$$-\frac{m^2+2}{r^2}\hat{u}_r, \quad -\frac{2m^2+1}{r^2}\hat{u}_\phi, \quad -\frac{3im}{r^2}\hat{u}_\phi, \quad \frac{3im}{r^2}\hat{u}_r.$$

since $\hat{u}_r$ and $\hat{u}_\phi$ can be non-zero on the axis for $m = 1$. Following Gelfgat et al. (1999) we express from the continuity equation (3.30d)

$$\frac{3im}{r^2}\hat{u}_r = -\frac{3im}{r}\partial_r \hat{u}_r + \frac{3m^2}{r^2}\hat{u}_\phi - \frac{3im}{r}\partial_z \hat{u}_z \tag{3.42a}$$

and

$$-\frac{3im}{r^2}\hat{u}_\phi = \frac{3}{r}\partial_r\hat{u}_r + \frac{3}{r^2}\hat{u}_r + \frac{3}{r}\partial_z\hat{u}_z. \tag{3.42b}$$

Substitution to (3.30) provides modified equations for $\hat{u}_r$ and $\hat{u}_\phi$

$$\begin{aligned}\eta\hat{u}_r = &-(u_{0,r}\partial_r + u_{0,z}\partial_z)\hat{u}_r - (\hat{u}_r\partial_r + \hat{u}_z\partial_z)u_{0,r} - \partial_r\hat{p}\\ &+\left(2\partial_{rr} + \frac{5}{r}\partial_r - \frac{m^2-1}{r^2} + \partial_{zz}\right)\hat{u}_r + \frac{im}{r}\partial_r\hat{u}_\phi + \left(\partial_{rz} + \frac{3}{r}\partial_z\right)\hat{u}_z\end{aligned} \tag{3.43a}$$

$$\begin{aligned}\eta\hat{u}_\phi = &-(u_{0,r}\partial_r + u_{0,z}\partial_z)\hat{u}_\phi - \frac{u_{0,r}\hat{u}_\phi}{r} - im\hat{p}\\ &+\left(\partial_{rr} + \frac{1}{r}\partial_r + \frac{m^2-1}{r^2} + \partial_{zz}\right)\hat{u}_\phi - \frac{2im}{r}\partial_r\hat{u}_r - \frac{2im}{r}\partial_z\hat{u}_z\end{aligned} \tag{3.43b}$$

where the non-integrable singularity is eliminated for $m = 1$. Thus, we employ the modified equations (3.43) for $\hat{u}_r$ and $\hat{u}_\phi$ when $m = 1$. For other azimuthal wave numbers $m \neq 1$, the original linearized equations (3.30a,b) are employed.

3.3 Numerical solution methods

3.3.1 Basic flow

The system (3.25) is discretized with the continuous Galerkin method (sec. 1.4.1). The inner product for cylindrical coordinates can be defined as

$$(\boldsymbol{a}, \boldsymbol{b}) = \frac{1}{2\pi}\int\limits_{\Omega\times\langle 0,2\pi\rangle} \boldsymbol{a}\cdot\boldsymbol{b}\, r\,\mathrm{d}r\,\mathrm{d}\phi\,\mathrm{d}z\ . \tag{3.44}$$

Due to the axial symmetry $\boldsymbol{a} = \boldsymbol{a}(r, z), \boldsymbol{b} = \boldsymbol{b}(r, z)$, the azimuthal integration is trivial and leads to

$$(\boldsymbol{a}, \boldsymbol{b}) = \int\limits_{\Omega} \boldsymbol{a}\cdot\boldsymbol{b}\, r\,\mathrm{d}r\,\mathrm{d}z.$$

The residual $\mathcal{R}_{\mathrm{NS}}$ of the dimensionless Navier–Stokes sub-system (3.25a,b) is analogous to (1.13). The residual of the energy equation (3.25c)

$$\mathcal{R}_{\mathrm{e}} = (\boldsymbol{u}_0\cdot\nabla T_h, \theta) + \frac{1}{\mathrm{Pr}}(\nabla T_h, \nabla\theta) - \frac{1}{\mathrm{Pr}}\langle\boldsymbol{n}\cdot\nabla T_h, \theta\rangle \qquad T_h, \theta\in\Theta \tag{3.45}$$

is obtained in the same way by integrating the heat diffusion term by parts. The test functions θ are set to 0 at the part of the boundary where a Dirichlet condition is prescribed for temperature, namely at the substrate $z = 0$ (3.24a). Thus, the boundary integral vanishes at the substrate. It also vanishes at the axis $r = 0$ due to the homogeneous

Neumann condition $\boldsymbol{n} \cdot \nabla T_0 = 0$ (3.26). At the free surface, the prescribed dimensionless heat flux (3.24d) is substituted into the boundary integral as

$$- \langle \boldsymbol{n} \cdot \nabla T_h, \theta \rangle = \langle \mathrm{Bi} T_h, \theta \rangle. \tag{3.46}$$

The Dirichlet boundary condition for the velocity $\boldsymbol{u}_0$ at the substrate (3.24a), and for its radial component $u_{0,r}$ also at the axis (3.26), are imposed in a strong sense. The integrand of the boundary integral at the axis

$$[\boldsymbol{n} \cdot (p_h \mathbf{I} - \boldsymbol{s}_h)] \cdot \boldsymbol{v} = \cancelto{0}{\partial_z u_{h,r}} + \cancelto{0}{\partial_r u_{h,z}} \tag{3.47}$$

vanishes due to the homogeneous Neumann condition for $u_{0,z}$.

At the free surface we have different boundary conditions in the normal (3.24c) and tangential (3.24e) directions, which do not coincide with the coordinate directions r and z. Therefore, the no-penetration condition cannot be easily enforced in a strong form. Instead, we project the boundary stress integral into the normal and tangential directions

$$\begin{aligned} \langle p_h \boldsymbol{n} - \boldsymbol{n} \cdot \boldsymbol{s}_h, \boldsymbol{v} \rangle = & \langle (\boldsymbol{n} \otimes \boldsymbol{n}) \cdot (p_h \boldsymbol{n} - \boldsymbol{n} \cdot \boldsymbol{s}_h), \boldsymbol{v} \rangle \\ & + \langle (\mathbf{I} - \boldsymbol{n} \otimes \boldsymbol{n}) \cdot (p_h \boldsymbol{n} - \boldsymbol{n} \cdot \boldsymbol{s}_h), \boldsymbol{v} \rangle \\ = & \langle p_h - \boldsymbol{n} \cdot \boldsymbol{s}_h \cdot \boldsymbol{n}, \boldsymbol{v} \cdot \boldsymbol{n} \rangle \\ & + \langle - \boldsymbol{n} \cdot \boldsymbol{s}_h \cdot \boldsymbol{t}_{rz}, \boldsymbol{v} \cdot \boldsymbol{t}_{rz} \rangle \end{aligned} \tag{3.48}$$

and impose both conditions independently in the weak form. The tangential shear stress is directly substituted with the thermocapillary stress from (3.24e)

$$\langle - \boldsymbol{n} \cdot \boldsymbol{s}_h \cdot \boldsymbol{t}_{rz}, \boldsymbol{v} \cdot \boldsymbol{t}_{rz} \rangle = \langle \mathrm{Re} \boldsymbol{t}_{rz} \cdot \nabla T_h, \boldsymbol{v} \cdot \boldsymbol{t}_{rz} \rangle . \tag{3.49}$$

The no-penetration boundary condition on the free surface is enforced with the method of Nitsche (1971). The method relies on adding a penalty term that measures the deviation from the no-penetration condition

$$\mathcal{R}_\mathrm{p} = \frac{C}{h} \langle \boldsymbol{n} \cdot \boldsymbol{u}_h, \boldsymbol{n} \cdot \boldsymbol{v} \rangle$$

to the residual of the Navier–Stokes sub-system. The value of the penalization constant $C = 60$ is selected. Furthermore, a stabilization term

$$\mathcal{R}_\mathrm{s} = \left\langle q - \boldsymbol{n} \cdot (\nabla \boldsymbol{v} + \nabla \boldsymbol{v}^\mathrm{T}) \cdot \boldsymbol{n}, \boldsymbol{u}_h \cdot \boldsymbol{n} \right\rangle , \tag{3.50a}$$

which is a symmetric counter-part of the normal boundary stress integral, is also added. Minimization of these Nitsche terms

$$\mathcal{R}_\mathrm{Ni} = \mathcal{R}_\mathrm{p} + \mathcal{R}_\mathrm{s} \stackrel{!}{=} 0 \tag{3.50b}$$

leads to enforcement of the no-penetration condition.

The final variational formulation of the problem reads

$$
\begin{aligned}
&\text{Find } (\boldsymbol{u}_h, p_h, T_h) \in \boldsymbol{V}_b \times Q \times \Theta_b \text{ such that} \\
&\qquad \mathcal{R}_{\mathrm{NS}}\left((\boldsymbol{u}_h, p_h), (\boldsymbol{v}, q)\right) + \mathcal{R}_{\mathrm{Ni}}\left((\boldsymbol{u}_h, p_h), (\boldsymbol{v}, q)\right) + \mathcal{R}_{\mathrm{e}}(T_h, \theta) = 0 \\
&\qquad\qquad \forall (\boldsymbol{v}, q, \theta) \in \boldsymbol{V}_0 \times Q \times \Theta_0.
\end{aligned} \tag{3.51}
$$

The variational formulation is solved using a Finite Element library FEniCS (Alnaes et al., 2015). To that end, the domain (fig. 3.2) is discretized with the package `mshr` into an unstructured mesh of triangular elements. The free surface is discretized into uniform, straight line segments - the edges of the elements.[2] In the interior of the domain, the mesh density parameter N (required by the meshing library `mshr`) is set inversely proportional to the square root of the height-to-wetting-radius ratio $N \sim 1/\sqrt{\Gamma}$. Namely, $N = 80/\sqrt{\Gamma}$, $90/\sqrt{\Gamma}$ and $110/\sqrt{\Gamma}$ for hot wall, cold wall and low $\mathrm{Pr} < 1$ and cold wall and high $\mathrm{Pr} \geq 1$, respectively. The size of the elements decreases close to the free surface, where the external element edges coincide with line segments approximating the curved boundary. The number of boundary segments per $\pi/2$ radians is set to $N^2/4$. Apart from the vicinity of the free surface, the size of the elements of the initial mesh is approximately uniform in the rest of the domain. Once the initial unrefined basic mesh has been generated, the elements adjacent to the substrate are divided into halves. An example of the structure of the mesh is shown with a smaller grid resolution $N = 20$ in figure 3.4. For a cold wall, the elements within the distance of 0.04 and 0.01 from the contact line $(r, z) = (1, 0)$ are divided to $1/8$ and $1/64$ of the size of elements in the interior for $\mathrm{Pr} < 1$ and $\mathrm{Pr} \geq 1$, respectively. For the computation of the linear stability with a hot wall and $m = 1$, the elements near the axis $r = 0$ are refined the same way as the elements near the wall, and the elements near the apex are refined the same way as those near the contact line in the case of a cold wall.

The standard Taylor–Hood elements are employed for the Navier–Stokes sub-system. The velocity field is approximated with quadratic element-wise Lagrange polynomials $\boldsymbol{V} = \mathbb{P}_2^2$ and the pressure with linear element-wise polynomials $Q = \mathbb{P}_1$. The temperature field is represented with the same polynomial order as the velocity $\Theta = \mathbb{P}_2$. The distribution of nodes and the shape of the basis functions are illustrated on a reference element in fig. 3.5. The discretization provides a system of non-linear algebraic equations $\boldsymbol{F}(\boldsymbol{Y}) = 0$ for the vector of nodal values $\boldsymbol{Y}$. The system is solved with a Newton–Raphson solver (algorithm 1.1) implemented in FEniCS, which automatically computes the Jacobian matrix $\nabla \boldsymbol{F}$.

3.3.2 Streamlines

Streamlines of the basic state, and of the axisymmetric perturbation, are computed as the isolines of the Stokes stream function ψ_{St}. A stream function ψ is in cylindrical

[2] During this work, the library FEniCS has been superseded by a newer version FEniCSx, which provides better support for elements with curved sides. For future works, it is advisable to employ curved elements to represent the free surface.

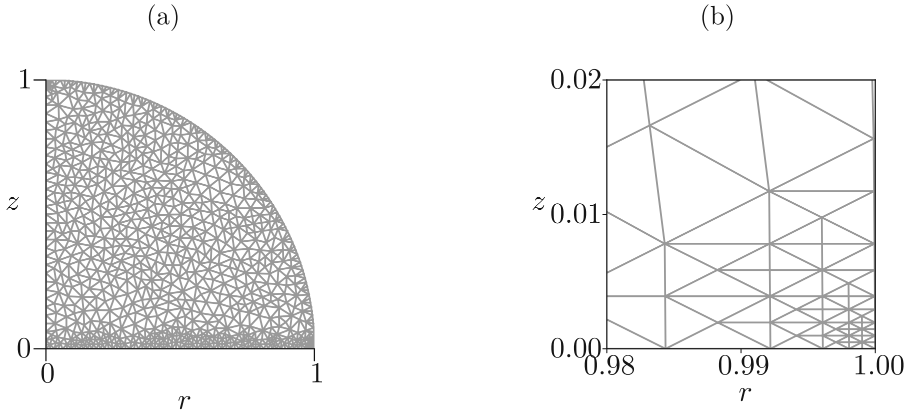

Figure 3.4: Illustration of the two-dimensional finite-element mesh for the computation of the thermocapillary-driven flow in a droplet on a wall

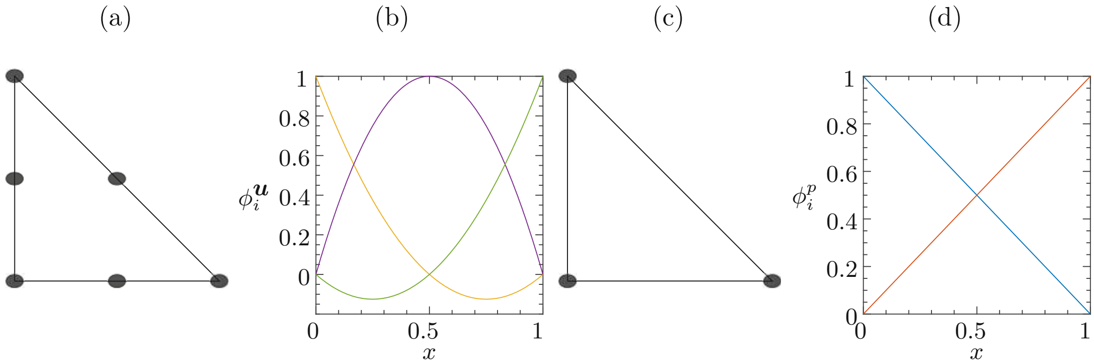

Figure 3.5: Distribution of grid nodes on a reference triangular finite element (a, c) and the corresponding basis and test functions (b, d) for velocity, temperature (a, b), and pressure (c, d).

coordinates defined as

$$u_{0,r} = \partial_z \psi \qquad\qquad u_{0,z} = -\partial_r \psi - \frac{1}{r}\psi \tag{3.52}$$

such that the continuity equation for an axisymmetric flow

$$\begin{aligned} \nabla \cdot \boldsymbol{u}_0 &= \frac{1}{r}u_{0,r} + \partial_r u_{0,r} + \partial_z u_{0,z} \\ &= \frac{1}{r}\partial_z \psi + \partial_{rz}\psi - \frac{1}{r}\partial_z \psi - \partial_{rz}\psi = 0 \end{aligned} \tag{3.53}$$

is identically satisfied. The isolines of ψ, however, do not coincide with the streamlines

$$\begin{aligned} \boldsymbol{u}_0 \cdot \boldsymbol{\nabla}\Psi &= u_{0,r}\partial_r \psi + u_{0,z}\partial_z \psi \\ &= \cancel{\partial_z \psi \partial_r \psi - \partial_r \psi \partial_z \psi} - \frac{1}{r}\psi \partial_z \psi \neq 0 \,. \end{aligned} \tag{3.54}$$

The streamlines can be computed as isolines of the Stokes stream function $\psi_{\mathrm{St}} = r\psi$

$$\begin{aligned}\boldsymbol{u}_0 \cdot \boldsymbol{\nabla}\psi_{\mathrm{St}} &= \boldsymbol{u}_0 \cdot \boldsymbol{\nabla}(r\psi) \\ &= u_{0,r}(\psi + r\partial_r\psi) + u_{0,z} r\partial_z\psi \\ &= -u_{0,r} r u_{0,z} + u_{0,z} r u_{0,r} \\ &= 0\ . \end{aligned} \tag{3.55}$$

In order to obtain a single PDE for ψ we use the definition of vorticity and substitute for the velocity components

$$\begin{aligned}\omega_0 &= (\boldsymbol{\nabla} \times \boldsymbol{u}_0) \cdot \boldsymbol{e}_\phi \\ &= \partial_z u_{0,r} - \partial_r u_{0,z} \qquad (3.56a)\\ &= \partial_z (\partial_z \psi) - \partial_r \left(-\partial_r \psi - \frac{1}{r}\psi \right) \\ &= \partial_{zz}\psi + \partial_{rr}\psi - \frac{1}{r^2}\psi + \frac{1}{r}\partial_r\psi \\ &= \boldsymbol{\Delta}\psi. \qquad (3.56b)\end{aligned}$$

The vorticity ω_0 is computed from the velocity components according to (3.56a), once the numerical solution $\boldsymbol{u}_h$ satisfying (3.51) is found. The Poisson equation (3.56b) for ψ is then subjected to a homogeneous Dirichlet condition at all boundaries

$$\psi = 0 \qquad\qquad \text{at } \partial\Omega, \tag{3.57}$$

which corresponds to a no-penetration condition (i.e., the outline of the domain is a single streamline). The problem (3.56b, 3.57) is again solved with the continuous Galerkin method

$$\text{Find } \psi_h \in \mathbb{P}_{2,0} \text{ such that} \qquad (\Delta\psi_h - \frac{\psi_h}{r^2}, \theta) = (\omega_0, \theta) \qquad \forall \theta \in \mathbb{P}_{2,0} \tag{3.58}$$

on the same mesh as used for the flow. $\mathbb{P}_{2,0}$ is the function space of element-wise second-order polynomials satisfying the homogeneous Dirichlet condition.

3.3.3 Linear stability

The equations for the modes (3.30), with the modification (3.43) for $m = 1$, subjected to the boundary conditions (3.32,3.35,3.403.41) are discretized in the same way as the equations for the basic state. The discretization provides the generalized eigenproblem (3.12). The matrices $\boldsymbol{M}$ and $\boldsymbol{A}$ are assembled by FEniCS and exported to SciPy (Virtanen et al., 2020) as sparse matrices of the type LIL (row-based list of lists). The eigenproblem is then solved with the SciPy function `sparse.linalg.eigs`, which is an interface to the Arnoldi Package (ARPACK) (Lehoucq et al., 1998).

The Arnoldi iteration algorithm implemented in ARPACK finds the eigenvalues with the largest magnitude. In order to find eigenvalues η with the largest real part (typically close to zero), the eigensolver must be operated in the shift-invert mode. The eigenproblem is internally transformed into a problem

$$(\boldsymbol{A} - \sigma_{\mathrm{A}}\boldsymbol{M})^{-1}\boldsymbol{M}\hat{q}_i = \hat{q}_i \nu_{\mathrm{A}} \tag{3.59}$$

with eigenvalues $\nu_{\mathrm{A}} = 1/(\eta - \sigma_{\mathrm{A}})$, which is then solved by the algorithm. The transformed eigenvalues ν_{A} with the largest magnitude obtained form the Arnoldi iteration correspond to the original eigenvalues η, which are closest to σ_{A}. The eigenvalues of interest are then obtained as $\eta = \sigma_{\mathrm{A}} + 1/\nu_{\mathrm{A}}$. More details of the implementation can be found in chapter 3.2 of (Lehoucq et al., 1998). We set $\sigma_{\mathrm{A}} = 1$ and request 50 converged eigenvalues. Furthermore, we set the value of the optional parameter `ncv` (which specifies the dimension of the Krylov subspace) to 300, as recommended by des Boscs and Kuhlmann (2021).

The Arnoldi iteration typically involves a large number of matrix-vector multiplications. These were computed by SciPy with the library OpenBLAS (Wang et al., 2014), which employs parallelization.

Computation of the neutral stability Reynolds number

The neutral stability Reynolds number Re_n is sought as a root of the function $\varsigma_1(\mathrm{Re})$, where ς_1 is the largest real part of the eigenvalues η for a given Reynolds number. It is advisable to employ an efficient root-finding algorithm due to the large computational requirements of the solution of the eigenproblem (3.12). The iterative method of Muller (1956) is employed in this work, as summarized in the algorithm 3.1. The essence of the method is to interpolate the last three computed values of $\varsigma_1(\mathrm{Re})$ quadratically and use the root closest to the last guess of Re_n as a new guess for which ς_1 is computed. It is then used in the next iteration. To initiate the algorithm, the first two interpolation points $\mathrm{Re}_{0,1}$ must be provided as initial guesses for the root. Re_0 is typically obtained by a quadratic extrapolation of the neutral stability curve and $\mathrm{Re}_1 = \mathrm{Re}_0 - \mathrm{sign}(\varsigma_1^0)\,\delta$ is shifted from Re_0 towards the expected location of the root by a guessed initial step δ. The third initial interpolation point is obtained by the secant method. In the subsequent iterations, the last three estimates of Re_n are employed for the interpolation. The computation is terminated once the change of Re_n between two subsequent iterations drops below 0.1%.

3.3.4 Verification

The implementation of the numerical methods is verified by reproducing the results of the linear stability analysis of thermocapillary convection in non-cylindrical liquid bridges (portion of liquid between two parallel and concentric support disks) due to Nienhüser and Kuhlmann (2002) for selected parameters. The comparison is summarized in tab. 3.3 for the contact angles $\alpha = 50°, 90°$ and $130°$, and Prandtl numbers $\mathrm{Pr} = 0.02$ and 4. In the interior of the domain, a uniform structured boundary-fitted mesh is employed. The number of elements N per radius of the support disks is varied to investigate the convergence of the critical Reynolds number with grid resolution. The elements near

Algorithm 3.1: The root-finding method of Muller (1956) for computation of the neutral Reynolds number

Data: Initial guess Re_0, initial step size δ, tolerance
Result: Re_n such that $\varsigma_1(\mathrm{Re}_n) = 0$

$\varsigma_1^0 \leftarrow \varsigma_1(\mathrm{Re}_0)$;
$\mathrm{Re}_1 \leftarrow \mathrm{Re}_0 - \mathrm{sign}(\varsigma_1^0)\,\delta$;
$\varsigma_1^1 \leftarrow \varsigma_1(\mathrm{Re}_1)$;
$\mathrm{Re}_2 \leftarrow \mathrm{Re}_1 - \varsigma_1^1 \frac{\mathrm{Re}_1 - \mathrm{Re}_0}{\varsigma_1^1 - \varsigma_1^0}$;
$k \leftarrow 2$;
while $|\mathrm{Re}_k - \mathrm{Re}_{k-1}|/\mathrm{Re}_k >$ tolerance **do**
    $k \leftarrow k + 1$;
    find $p(\mathrm{Re}) \in \mathbb{P}_2$ such that $p(\mathrm{Re}_i) = \varsigma_1^i \,\forall i \in \{k-3, k-2, k-1\}$;
    find r_1, r_2 such that $p(r_{1,2}) = 0 \wedge |r_1 - \mathrm{Re}_{k-1}| < |r_2 - \mathrm{Re}_{k-1}|$;
    $\mathrm{Re}_k \leftarrow r_1$;
end
return Re_k

Pr	0.02			4		
α / N	50°	90°	130°	50°	90°	130°
40	2426	2058	2930	1458	1001	805
60	2411	2058	2911	1452	1001	807
80	2408	2059	2907	1451	1001	808
100	2405	2059	2902	1449	1001	808
N&K	2380	2060	3070	1445	1010	800

Table 3.3: Grid convergence of the critical Reynolds number Re_c of the linear stability of axisymmetric thermocapillary convection to perturbation with $m = 2$ in non-cylindrical liquid bridges in zero gravity $\mathrm{Bo} = 0$ for various contact angles α and two different Prandtl numbers Pr. The results are compared to Nienhüser and Kuhlmann (2002), indicated by N&K.

each disk within the distance of 1% of the radius are halved, while those within the 1% distance from the free surface are gradually refined to 1/32 of the size of the elements in the interior. The elements within the distance of 0.06% of the support-disk radius from the triple lines are refined to 1/64 of the size of the elements in the interior. For $N = 100$ the critical Reynolds number agrees with Nienhüser and Kuhlmann (2002) up to 1%, except the demanding case of $\mathrm{Pr} = 0.02, \alpha = 130°$, for which a 5% difference is observed. For $\mathrm{Pr} = 4$, the agreement between the oscillation frequencies ω_c (not shown) is at a similar level. The instability is stationary for $\mathrm{Pr} = 0.02$.

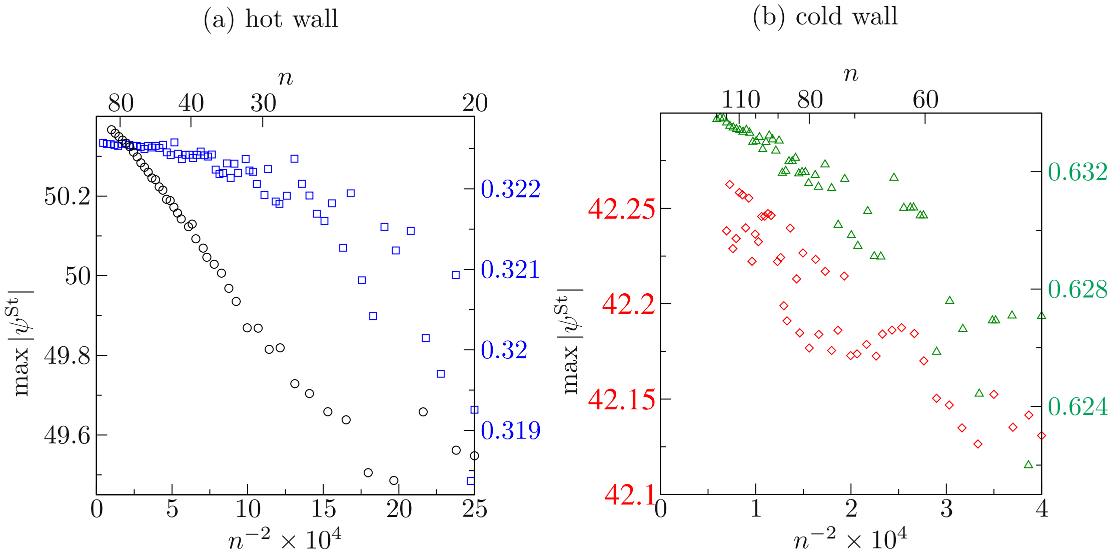

Figure 3.6: Convergence of the maximum absolute value of the Stokes stream function $|\psi^{\mathrm{St}}|_\infty$ of the basic flow with respect to n^{-2} for a hot (a) and cold (b) wall and $(\mathrm{Pr}, \alpha, \mathrm{Re}, \mathrm{Bi}) = (10^{-3}, 90°, 37024, 0.2362)$, $(16.36, 25°, 23622, 0.2362)$, $(0.038, 120°, 35645, 0.2362)$ and $(28.1, 120°, 17115, 0.4)$ indicated with black, blue, red and green symbols, respectively.

3.3.5 Grid convergence

The grid convergence of the numerical solution for typical combinations of the governing parameters is investigated by plotting the value of the global extremum of the Stokes stream function (fig. 3.6) and the critical Reynolds number (fig. 3.7) against n^{-2}, where $n = N\sqrt{\Gamma}$ is a scaled mesh parameter. A straight line in these axes indicates a quadratic convergence.

Four cases with high values of the Reynolds number $\mathrm{Re} \sim \mathcal{O}(10^4)$ were selected for fig. 3.6. Notice that the span of the vertical axis is below 2%. The maximum absolute value of the Stokes stream function $\max|\psi^{\mathrm{St}}|$ tends to increase with n, but converges quadratically to a finite value. Only for the blue symbols in fig. 3.6(a) the convergence seems to be super-quadratic. This deviation from the quadratic convergence might be related to the discretization of the free-surface shape with $\sim N^2$ line segments.

For coarser meshes the convergence plots in fig. 3.6 are polluted by a chaotic noise due to the unstructured nature of the meshes. This noise becomes insignificant for higher n. Note that even for the red symbols in fig. 3.6(b) the noise is well below 1%.

For a hot wall, $n = 60$ and $(\mathrm{Pr}, \alpha) = (16.36, 16°)$ (blue in fig. 3.7a) and $(\mathrm{Pr}, \alpha) = (10^{-3}, 90°)$ (black in fig. 3.7a), the critical Reynolds number Re_c is already converged to 0.1‰ and 5‰ deviation from the quadratically extrapolated value for an infinitely fine mesh. With the value $n = 80$ employed in this study, the estimated accuracy of the

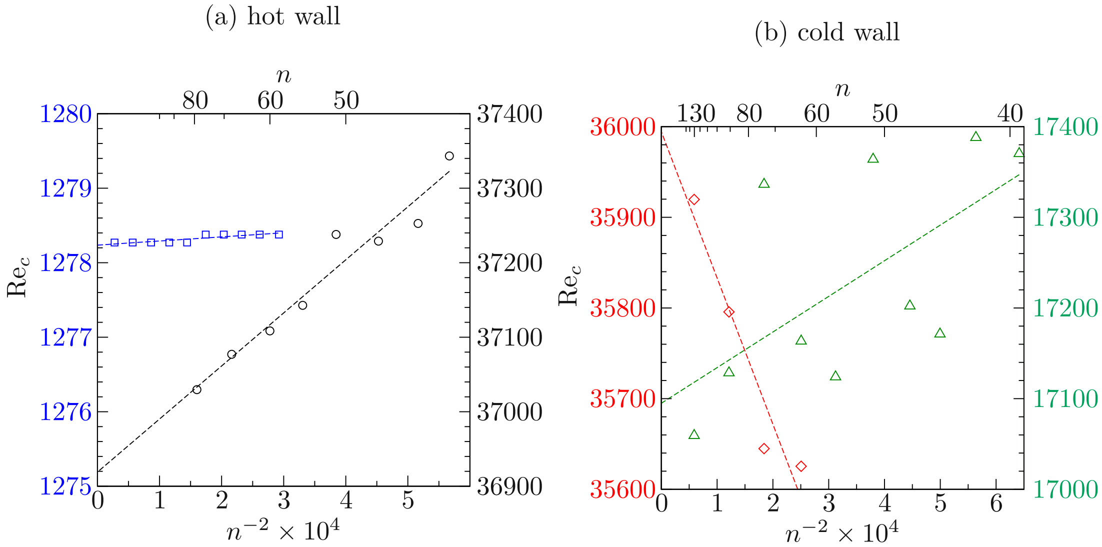

Figure 3.7: Convergence of the critical Reynolds number Re_c with respect to n^{-2} for a hot (a) and cold (b) wall and $(\mathrm{Pr}, \alpha, \mathrm{Bi}) = (10^{-3}, 90°, 0.2362)$, $(16.36, 16°, 0.2362)$, $(0.038, 120°, 0.2362)$ and $(28.1, 120°, 0.4)$ indicated by black, blue, red and green symbols, respectively. The dashed lines are the least-squares linear fits.

latter case is 3‰.

The mesh requirements are higher in the case of a cold wall. With $n = 90$, Re_c is converged to 6‰ for $(\mathrm{Pr}, \alpha) = (0.038, 120°)$ (red in fig. 3.7b). For $(\mathrm{Pr}, \alpha, \mathrm{Bi}) = (28.1, 120°, 0.4)$ (green in fig. 3.7b), there remains some noise in the convergence plot with an amplitude of approximately 8‰ for $n \in \langle 73, 130 \rangle$.

With the grid resolution selected in this study, the numerical results are converged to a tolerance of 1% for all combinations of parameters presented.

3.4 Results

We observe instabilities of the basic state in more or less distinct regions of the parameter space spanned by α, Pr, and the sign of the wall temperature with respect to the ambient. They are categorized based on the dominant symmetry-breaking mechanism.

Marangoni instability is presented in section 3.4.1. It is observed for low-α high-Pr droplets on a hot wall. It is characterized by steady or traveling convection cells, typically close to the axis $r = 0$. An up-flow at the centers of the convection cells lifts hot fluid from the wall towards the free surface. The perturbation of the free-surface temperature induces thermocapillary stress, which drives the perturbation flow. As this instability relies on the perturbation of the temperature field, the critical Reynolds number diverges as $\mathrm{Pr} \to 0$.

Section 3.4.2 describes a purely hydrodynamic instability due to **inertial** symmetry breaking of the basic toroidal vortex. This instability is driven by inertia in the bulk of the flow, and it does not rely on the perturbation of the temperature field. It is, therefore, the main mechanism in the limit of low Prandtl number fluids (e.g., liquid metals). We find this instability for higher contact angles and both hot and cold walls.

Finally, a **hydrothermal wave** (HTW) instability is presented in section 3.4.3. It derives energy from gradients of the basic temperature field in the bulk. An internal perturbation flow (possibly driven also by inertia) generates internal extrema of the temperature perturbation. These cause a weak perturbation of the free-surface temperature, and the induced thermocapillary stress feeds energy onto the perturbation flow. The hydrothermal waves are observed for higher α and Pr. For the hot wall, the basic state is characterized by a region of cold fluid near the apex. A displacement of this cold fluid from the apex along the free surface is the most dangerous perturbation. For the cold wall, on the other hand, the basic state exhibits a layer of hot fluid along the entire free surface. This layer suppresses perturbations of the free-surface temperature. The critical Marangoni number is thus significantly higher for the cold wall than for the hot wall.

3.4.1 Marangoni instability

This section considers a representative Prandtl number $\mathrm{Pr} = 16.36$, which corresponds to 1 cSt silicone oil. The wall is hot, and the contact angles are small ($\alpha \leq 25°$).

Basic thermocapillary flow

The thermocapillary stress due to the basic temperature field is directed from the contact line towards the apex, driving a toroidal vortex that rotates counter-clockwise in the $r-z$ plane (fig. 3.8). For very small contact angles ($\alpha < 10°$), the basic thermocapillary vortex at the stability threshold is weak, especially close to the axis $r = 0$. The temperature distribution in this region is dominated by conduction, with an almost linear vertical profile (fig. 3.8a). For $\alpha = 15°$ the vortex spreads up to the axis and a hyperbolic stagnation ring appears at $(r, z) = (0.187, 0.083)$, as indicated by the cross in fig. 3.8b. As the contact angle increases, the stagnation ring vanishes, and the vortex gains strength. It advects hot fluid from the contact line along the free surface, such that for $\alpha = 25°$, the vertical temperature gradient is locally inverted in part of the droplet.

Steady axisymmetric Marangoni convection

We consider $\alpha = 5°$ in some detail as a representative example of a very shallow droplet. The region of vanishing flow near $r = 0$ with an almost linear vertical temperature profile is reminiscent of liquid pools with a small aspect ratio (Koschmieder and Prahl, 1990). It is thus prone to Marangoni instability. For comparison, we follow Schatz and Neitzel (2001) and estimate the apex temperature from a local Biot number $\mathrm{Bi}_H = hH/\lambda = \mathrm{Bi}\Gamma$

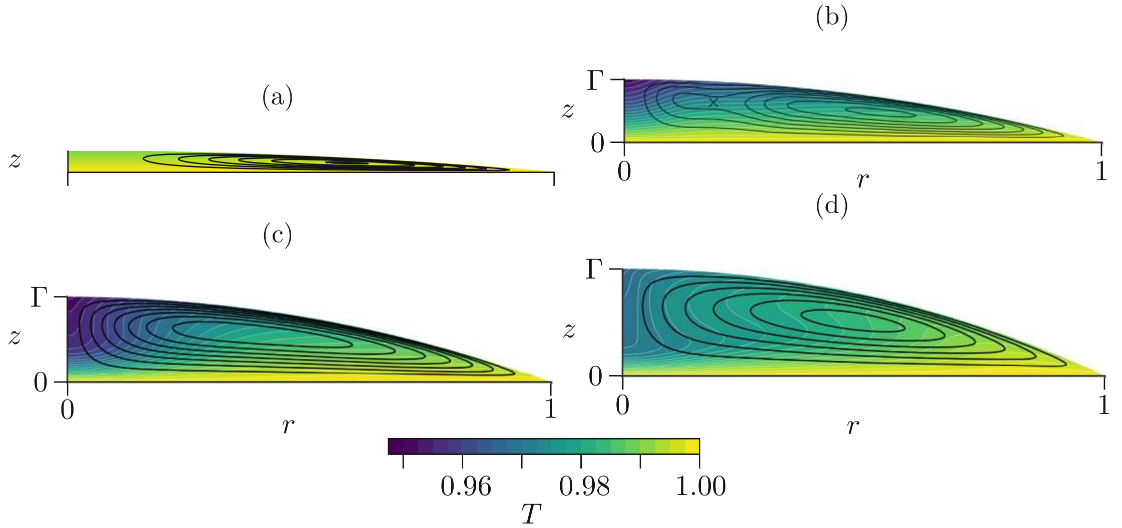

Figure 3.8: The temperature field (color) and streamlines (black) of the neutrally stable steady axisymmetric basic state for (a) $\alpha = 5°$, $\mathrm{Ma}_{H,c} = 83.35$, (b) $\alpha = 15°$, $\mathrm{Ma}_{H,c} = 122.0$, (c) $\alpha = 20°, \mathrm{Ma}_{H,c} = 603.3$, (d) $\alpha = 25°, \mathrm{Ma}_{H,c} = 4263$

at $r = 0$ as

$$T_{\mathrm{apex}} \approx \frac{T_w + \mathrm{Bi}_H T_a}{1 + \mathrm{Bi}_H}. \tag{3.60}$$

The Marangoni number based on the height H and the temperature difference between the wall and the apex

$$T_w - T_{\mathrm{apex}} = (T_w - T_a)\frac{\mathrm{Bi}_H}{1 + \mathrm{Bi}_H} \tag{3.61}$$

is then defined by

$$\begin{aligned} \mathrm{Ma}_H &= \frac{\rho c_p \gamma |T_w - T_{\mathrm{apex}}| H}{\mu \lambda} \\ &= \frac{\rho c_p \gamma \Delta T R}{\mu \lambda} \cdot \frac{H}{R} \cdot \frac{|T_w - T_{\mathrm{apex}}|}{|T_w - T_a|} \\ &= \mathrm{Ma}\,\Gamma \frac{\mathrm{Bi}\,\Gamma}{1 + \mathrm{Bi}\,\Gamma}, \end{aligned} \tag{3.62}$$

where $\mathrm{Ma} = \mathrm{RePr} = \rho c_p \gamma \Delta T R/(\mu\lambda)$ is the usual definition of the Marangoni number.

When the Marangoni number is increased beyond $\mathrm{Ma}_H = 82.16$, another steady axisymmetric flow solution (fig. 3.9b) comes into existence in addition to the thermocapillary flow (fig. 3.9a). The new solution is of Marangoni type. It consists of axisymmetric convection cells (tori) near the axis, the strengths of which decay in the radial direction, such that only the thermocapillary flow remains closer to the contact line. This radial

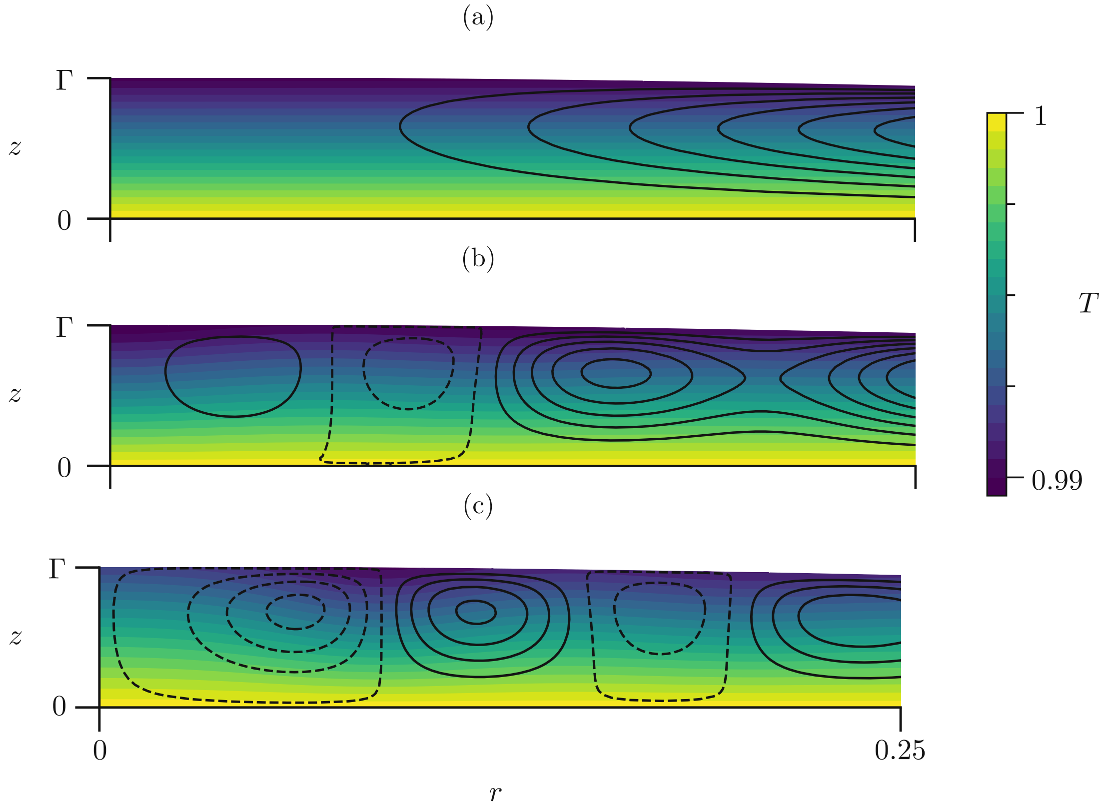

Figure 3.9: Steady two-dimensional flow states for heating from below, $\alpha = 5°$, $\mathrm{Pr} = 16.36$ and $\mathrm{Ma}_H = 87.0$ (triangles in fig. 3.10). (a) lower disconnected branch ($w(0, \Gamma/2) = -0.031$); (b) connected branch ($w(0, \Gamma/2) = -0.609$); (c) upper disconnected branch ($w(0, \Gamma/2) = 0.889$)

decay of the convection cells is related to the value of the local Marangoni number

$$\mathrm{Ma}_{\mathrm{loc}} = \mathrm{Ma}_H \frac{d(r)}{H} \tag{3.63}$$

based on the local depth $d(r)$, which decreases in the radial direction.

The bifurcation of the solutions is visualized in fig. 3.10 by plotting the vertical velocity $w(0, \Gamma/2)$ at mid-height at the axis versus the Marangoni number Ma_H. The orange curve, which comes from low Marangoni numbers and small negative $w(0, \Gamma/2)$, will be called the 'connected branch' in the following. The axisymmetric Marangoni cells with an up-flow at the axis come into existence by a saddle-node bifurcation at $(\mathrm{Ma}_H, w(0, \Gamma/2)) = (82.16, 0.479)$ (indicated by square in fig. 3.10). The two blue forward branches emerging from the saddle node will be called 'disconnected branches'. Along the stable upper disconnected branch (solid blue curve), the strength and radial extent of the convection cells increase upon an increase of the Marangoni number, at the expense of the thermocapillary vortex. The strength of the Marangoni convection

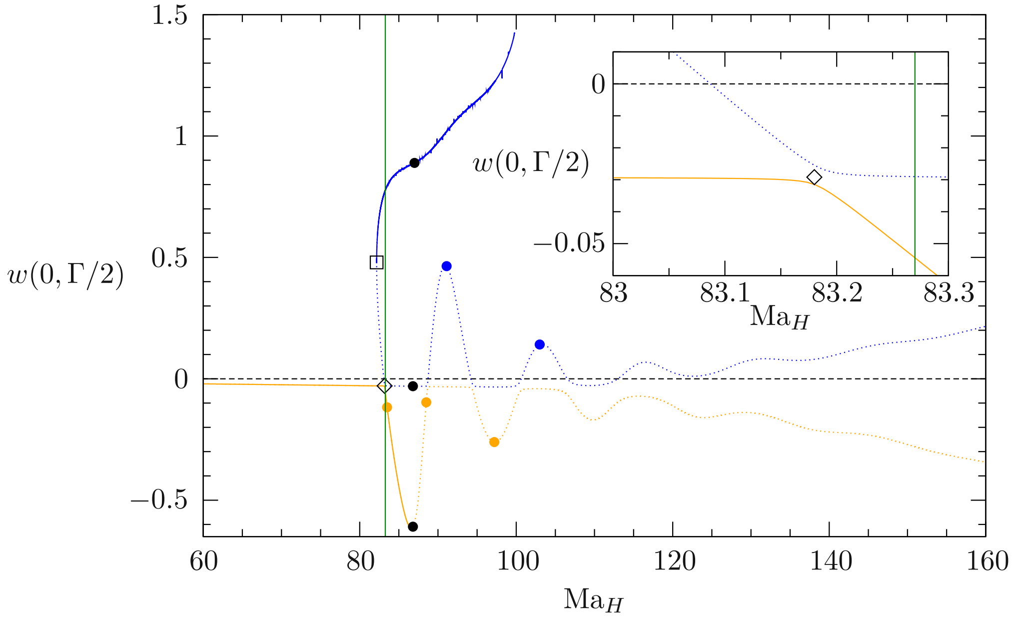

Figure 3.10: Bifurcation diagram showing the dependence of the vertical velocity w at the axis midpoint $(r, z) = (0, \Gamma/2)$ on the Marangoni number Ma_H for the steady axisymmetric states shown in fig. 3.9. The solid line indicates the part of the branch which is linearly stable to axisymmetric perturbation, while the dotted line indicates unstable solutions. The connected branch is shown in orange and the disconnected branches are shown in blue. The black square marks the saddle-node bifurcation point, the diamond shows the (weakly perturbed) transcritical bifurcation point, and the dots indicate Marangoni numbers for which the flow near the axis is illustrated in figs. 3.9 and 3.11. The green vertical line indicates the linear stability boundary with respect to three-dimensional perturbation.

decreases steeply along the unstable lower disconnected branch (dotted blue curve) such that it would seem to intersect the connected branch at a transcritical bifurcation point $(\mathrm{Ma}_H, w(0, \Gamma/2)) = (83.18, -0.029)$ (diamond in fig. 3.10). The transcritical bifurcation is, however, imperfect, as can be seen from the inset in fig. 3.10. It is perturbed by the weak thermocapillary flow.

In the absence of the thermocapillary flow, the transcritical bifurcation would be perfect. It seems that $w(0, \Gamma/2)$ would oscillate between positive and negative values along the lower disconnected branch, leading to a sequence of transcritical bifurcation points (intersections with $w(0, \Gamma/2) = 0$) where the Marangoni cells change the sense of rotation. Here, the thermocapillary flow becomes stronger when Ma_H increases and the transcritical bifurcations become increasingly perturbed. The connected (orange) and the lower disconnected (blue) branches separate from each other for $\mathrm{Ma}_H > 120$.

The evolution of the axisymmetric Marangoni cells along the connected and the lower disconnected branches is visualized in fig. 3.11 by plotting the difference between the flows

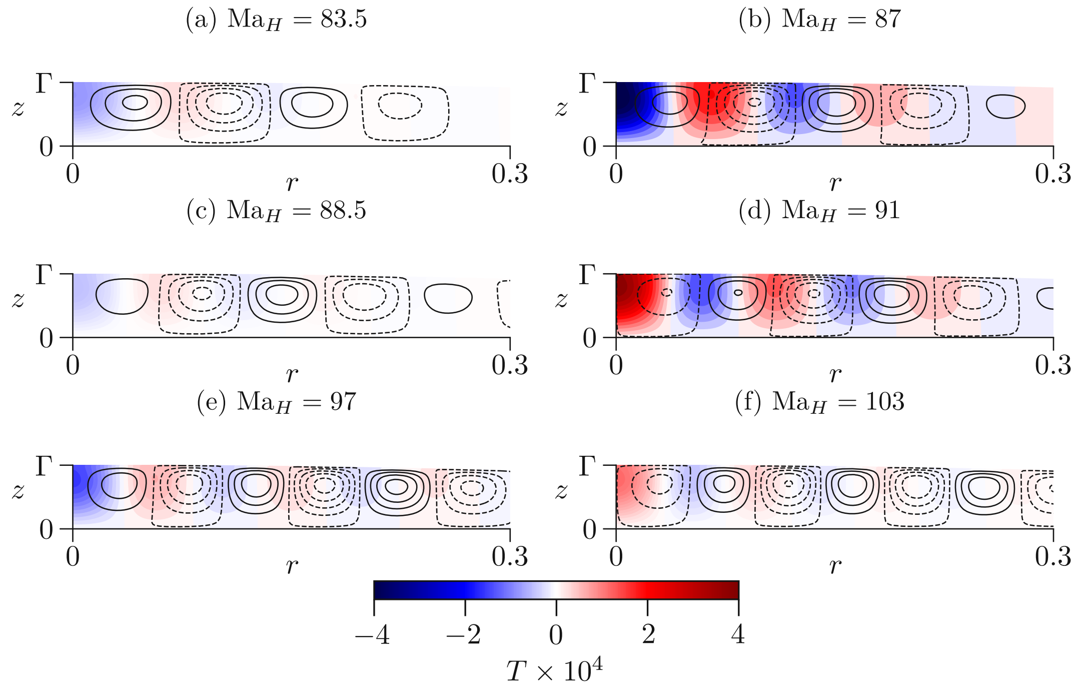

Figure 3.11: Difference of the flows corresponding to the orange and the lower part of the blue branch in fig. 3.10 for the Marangoni numbers indicated in the sub-captions

on these branches for the same Ma_H. The flow with lower $|w(0, \Gamma/2)|$ is subtracted from the other one. The strength of the cells (visualized by the difference of the temperature fields) and their sense of rotation depend sensitively on Ma_H. On the other hand, their radial wavelength only weakly decreases with Ma_H.

Symmetry-breaking Marangoni instability

This section investigates the linear stability of the steady axisymmetric flow on the connected branch, denoted as *basic state* in the following, to three-dimensional or time-dependent perturbation. The upper disconnected branch solution is linearly stable for $\alpha = 5°$ at the critical stability boundary $\mathrm{Ma}_{H,c} = 83.27$ of the connected branch. For $\alpha = 15°$ we can no longer find the disconnected branches.

For $\alpha = 5°$, the most dangerous symmetry-breaking perturbation in form of steady three-dimensional convection cells (fig. 3.12) is as well localized near the axis $r = 0$ in the region of vanishing basic flow with almost linear dependence of T_0 on z. Similarly to the Marangoni instability in low-aspect-ratio cylindrical liquid pools (Koschmieder and Prahl, 1990), the neutral Marangoni numbers $\mathrm{Ma}_{H,n}$ for different azimuthal wavenumbers are close to each other (tab. 3.4). At the contact angles $\alpha < 8°$, the most dangerous wave numbers are $m = 1$ and 2, and their neutral curves are almost indistinguishable (fig. 3.13a). Quadratic extrapolation of $\mathrm{Ma}_{H,n}$ for $m = 2$ to the limit of vanishing contact

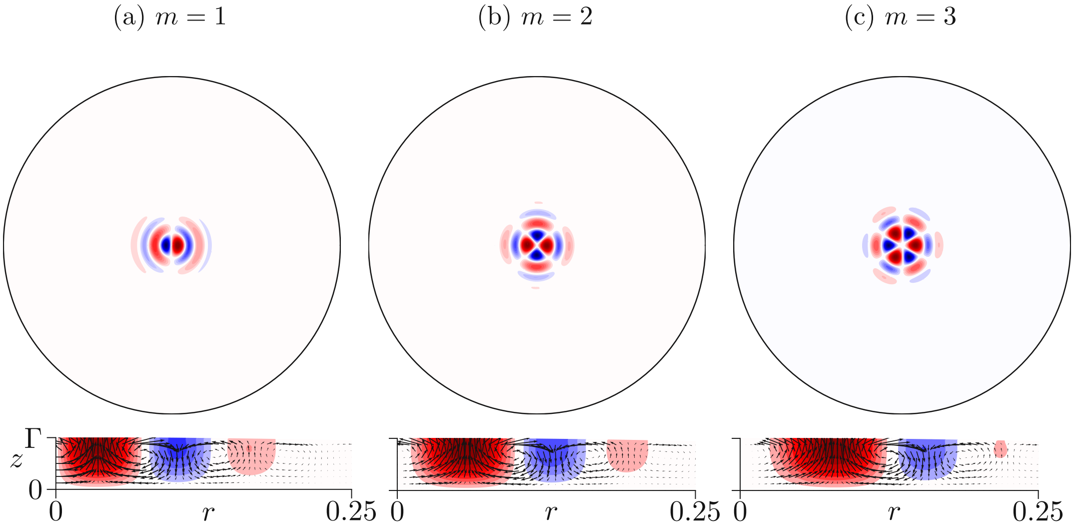

Figure 3.12: The most dangerous perturbation modes for heating from below, $\alpha = 5°$ and $\mathrm{Pr} = 16.36$. The azimuthal wave numbers are indicated in the sub-captions, and the corresponding neutral Marangoni numbers are provided in tab. 3.4. The free surface temperature is shown at the top, while at the bottom, the velocity vectors and temperature field close to the axis are shown in the meridional plane $\phi =$ const. containing the maximum temperature perturbation.

m	0	1	2	3	4	5	6	7	8
$\mathrm{Ma}_{H,n}$	87.01	83.27	83.35	83.92	84.47	85.18	87.04	86.82	87.55

Table 3.4: The neutral stability Marangoni numbers $\mathrm{Ma}_{H,n}$ for given azimuthal wave numbers m for a droplet on a hot substrate with the contact angle $\alpha = 5°$ and the Prandtl number $\mathrm{Pr} = 16.36$

angle gives $\mathrm{Ma}_{H,c}(\alpha \to 0) \approx 79.6$. This is a typical value for low-aspect-ratio liquid pools.

When α is increased, the critical m changes frequently, and the most dangerous perturbation extends in the positive radial direction (compare figs. 3.12 and 3.14). In the range $12.5° < \alpha < 13.5°$, the neutral curves of the steady modes $m = 2$ and 3 turn backward (see the inset in fig. 3.13a) and intersect other neutral curves of time-dependent modes with the same azimuthal wavenumbers, which continue to higher contact angles. Such intersections occur at $\alpha = 8.39°, 12.7°$ and $13.3°$ for $m = 1, 2$ and 3, respectively.

The time-dependent modes arise in pairs with complex conjugate eigenvalues η, where for $m > 0$, positive and negative oscillation frequencies ω indicate, respectively, clockwise and counter-clockwise rotation of the perturbation pattern in the view from the top with an azimuthal phase speed ω/m. Only the positive frequencies are plotted in fig. 3.13(b), and the corresponding clockwise-rotating modes are shown in fig. 3.14(a, b).

The frequencies grow with α (fig. 3.13b). The temperature perturbation at the droplet

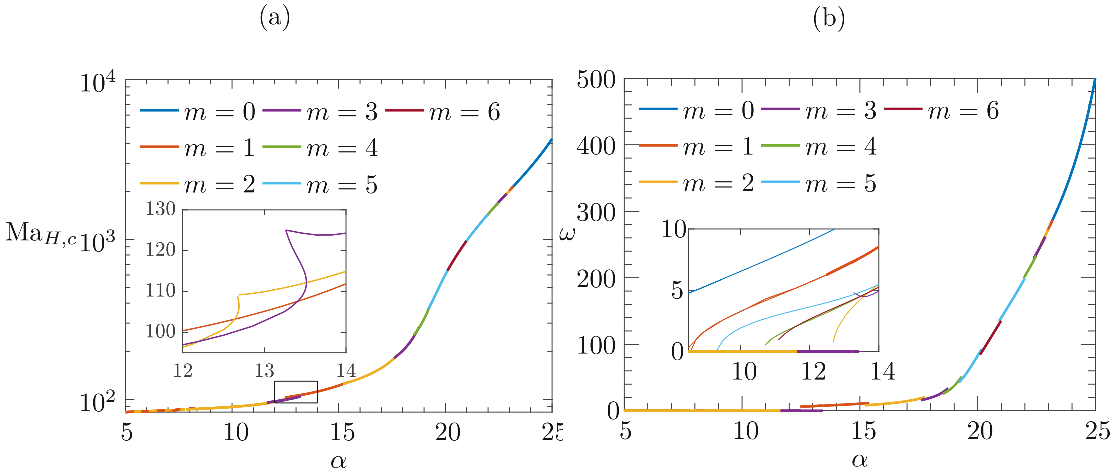

Figure 3.13: Dependence of the critical Marangoni number $\mathrm{Ma}_{H,c}$ (a) and of the critical oscillation frequency ω_c of the most dangerous mode (b) on the contact angle α for shallow droplets on a hot substrate with $\mathrm{Pr} = 16.36$. For $\alpha < 8°$, the critical curves for the azimuthal wavenumbers $m = 1$ and $m = 2$ are almost indistinguishable. The insets in (a) and (b) show the neutral Marangoni numbers $\mathrm{Ma}_{H,n}$ and neutral frequencies ω_n, respectively.

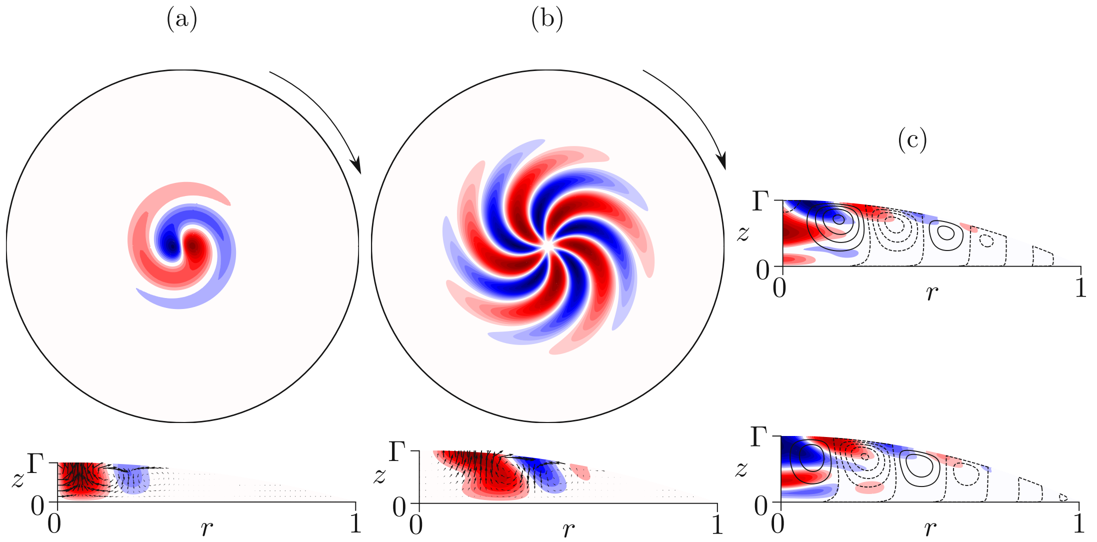

Figure 3.14: The most dangerous perturbation at the onset of instability for a droplet on a hot substrate with $\mathrm{Pr} = 16.36$ and: (a) $\alpha = 15°, \mathrm{Ma}_H = 122.0, m = 1$, (b) $\alpha = 20°, \mathrm{Ma}_H = 603.3, m = 5$, (c) $\alpha = 25°, \mathrm{Ma}_H = 4263, m = 0$. For the three-dimensional perturbation (a) and (b), the surface temperature is shown at the top, while the velocity and temperature field in a meridional plane containing the maximum positive temperature perturbation is shown at the bottom. For the axisymmetric perturbation (c) the projection to a meridional plane is shown for an arbitrary time t_0 (top) and $t_0 + \pi/(2\omega)$ (bottom).

surface develops a fan-blade shape (fig. 3.14a,b) similar to that observed by Karapetsas et al. (2012) in shallow evaporating droplets on a perfectly conducting substrate. In a cut with a fixed meridional plane $\phi = \text{const.}$, Marangoni convection cells can still be identified. They travel along the free surface towards the axis $r = 0$.

$\mathrm{Ma}_{H,c}$ rises steeply with α. This may be attributed to the basic temperature field. The basic thermocapillary flow, the strength of which grows with increasing α, transports hot fluid from the contact line towards the apex, decreasing or even inverting the local vertical temperature gradient (fig. 3.8d). When α exceeds 23°, the axisymmetric ($m = 0$) time-dependent perturbation becomes the most dangerous one. It consists of convection cells (fig. 3.14c) which travel in negative radial direction.

Influence of the Prandtl number

The effect of the Prandtl number is illustrated for a representative contact angle $\alpha = 16°$ in fig. 3.15. The critical Marangoni number decreases monotonically with Pr but saturates for large values of Pr. The critical Reynolds number $\mathrm{Re}_c = \mathrm{Ma}_c/\mathrm{Pr}$ then becomes inversely proportional to Pr. As Re_c drops to low values for large Pr, the basic flow at critical conditions becomes creeping and thus independent of Re. Inertia becomes negligible, and the stability of the basic flow then depends only on the ratio between convective and diffusive heat transfer within the droplet (i.e., on the value of the Marangoni number).

For this type of instability, the critical Marangoni number diverges as $\mathrm{Pr} \to 0$ (relevant, e.g., for liquid metals). This is because the instability relies on the perturbation of the temperature field by the perturbation flow. For low Pr, temperature perturbations are diffused rapidly, so that they cannot drive the perturbation flow.

3.4.2 Inertial instability

In this section, we consider the breaking of symmetry in the limit of a small Prandtl number, $\mathrm{Pr} \ll 1$ (such that Bi and Re remain finite). This limit is relevant, e.g., for droplets of liquid metals (additive manufacturing). The temperature field is governed by conduction, i.e., it is independent of the flow. It depends only on α and Bi. The basic temperature field is the same for heating or cooling from the wall, except for the sign. The basic flow, on the other hand, still depends also on the Reynolds number and on the sign of the dimensionless wall temperature. The latter affects not only the sense of rotation of the basic vortex but, for a non-zero Reynolds number, also the shape of the streamlines (as described in the following sub-section). The Marangoni number $\mathrm{Ma} = \mathrm{RePr}$ is not a suitable control parameter for $\mathrm{Pr} \ll 1$ and finite Re. Since the temperature diffuses too rapidly compared to convection, the temperature perturbation vanishes for vanishing Pr and finite Re. Thus, there is no perturbation of the thermocapillary stress in this limit which could drive a perturbation flow. Any instabilities can then only be driven by the inertial bulk terms in the linearized momentum equation (3.28a).

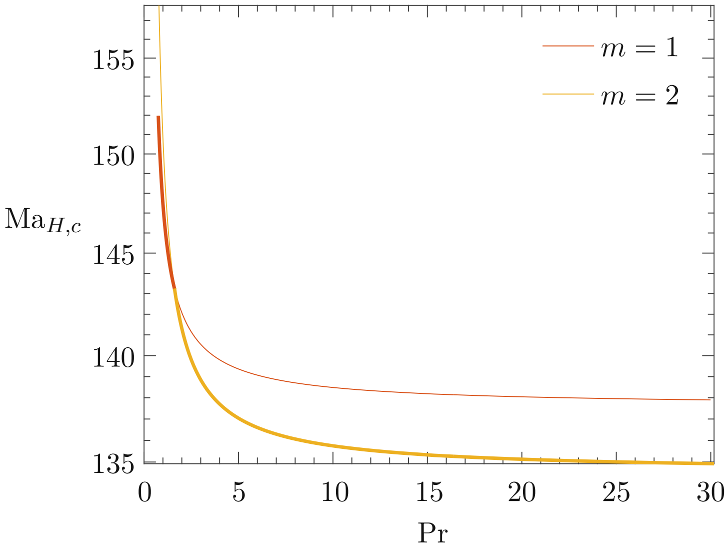

Figure 3.15: Dependence of $\mathrm{Ma}_{H,c}$ on the Prandtl number Pr for droplets on a hot substrate with $\alpha = 16°$. Thick lines indicate critical curves, while thin lines indicate neutral curves.

Basic flow

As described above, the basic temperature field (fig. 3.16a,d) is independent of the flow, but it determines the distribution of the thermocapillary stress which drives the basic flow. The basic flow at criticality for two different contact angles $\alpha = 100°$ and 120° and either hot or cold wall is show in fig. 3.16(b,c,e,f) for a very small Pr. For $\alpha = 120°$, it consists of a single toroidal vortex. The largest thermocapillary stress is close to the contact line. On a hot wall (fig. 3.16b,e), the fluid is accelerated from zero velocity at the contact line along the free surface towards the apex. The thermocapillary driving decays with increasing distance from the contact line, and the maximum velocity is reached on the free surface at some intermediate height. Near the apex, the fluid is decelerated and deflected downwards. On the other hand, on a cold wall (fig. 3.16c,f), the flow is driven by the free surface from the stagnation point at the apex towards the contact line, and the driving thermocapillary stress grows in the direction of the flow. Thus, the maximum velocity is reached at the free surface close to the contact line, where the flow turns sharply towards the axis and away from the wall. For a cold wall, the center of the vortex is closer to the contact line. For a hot wall, the flow is stronger near the axis as compared to a cold wall.

Effect of α on the basic flow and on the stability boundary

The effect of the contact angle on the critical Reynolds number Re_c and on the critical oscillation frequency ω_c (in case of a time-dependent perturbation) is shown in fig. 3.17. Both Re_c and ω_c decay monotonically with α. For $\alpha = 120°$, the critical Reynolds number

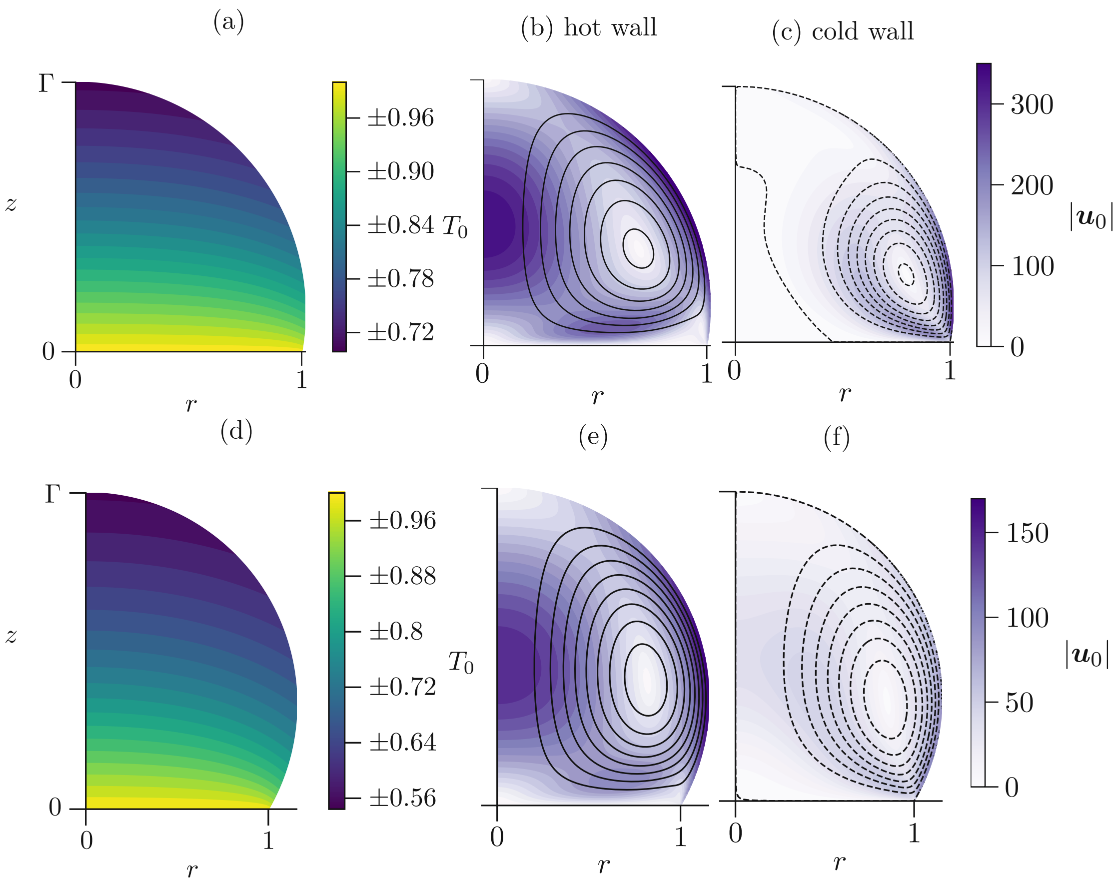

Figure 3.16: The marginally stable basic state for $\mathrm{Pr} = 10^{-3}$ and: $\alpha = 100°$ (a–c), $\alpha = 120°$ (d–f). The left column shows the basic temperature field. The middle and the right columns show the streamlines and the velocity magnitude (color) for the hot and cold walls, respectively. The critical Reynolds numbers are: $\mathrm{Re}_c = 14622$ (b), $\mathrm{Re}_c = 12030$ (c), $\mathrm{Re}_c = 3102$ (e), $\mathrm{Re}_c = 1700$ (f).

is one order of magnitude smaller compared to $\alpha = 100°$. This is due to the increase in the size of the droplet relative to R, the temperature variation across the droplet (fig. 3.16a,d), and the free surface area across which the thermocapillary stress drives the flow. The maximum basic flow velocity at critical conditions (fig. 3.16b,c,e,f) is of the order of 100. It decreases by approximately one half when α is increased from 100° to 120°. Also, the increased strain due to the axial stretching of the basic vortex might support the instability. In the case of a cold wall, the streamlines are more sensitive to the contact angle. Namely, the basic vortex shrinks towards the contact line when α decreases.

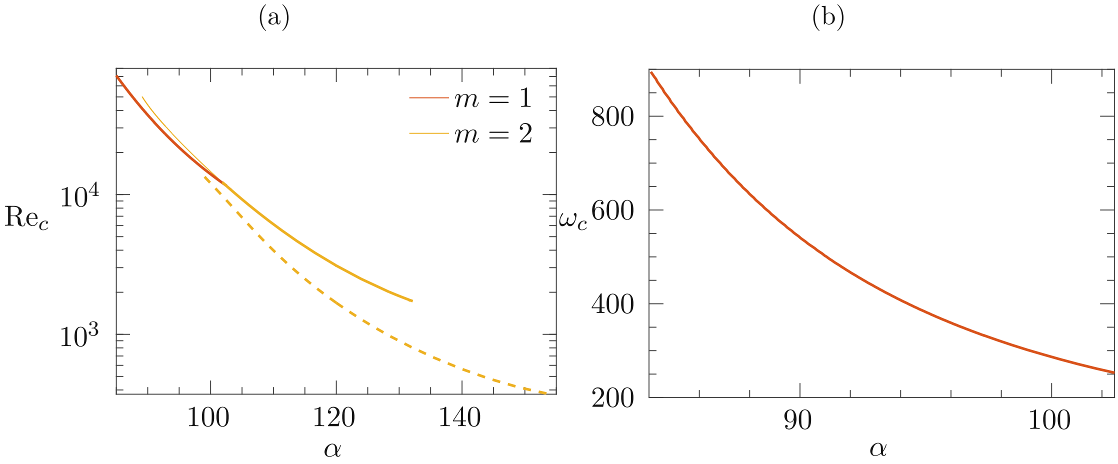

Figure 3.17: Dependence of the critical Reynolds number Re_c (a) and of the critical frequency ω_c on the contact angle for droplets with $\mathrm{Pr} = 0.001$. The azimuthal wavenumber m is coded by color (see the legend in a). Solid lines correspond to a hot wall, while the dashed line indicates a cold wall. The mode with $m = 2$ is steady. Both the full and the dashed line continue to the complete range of α shown, but only part of each critical curve was computed.

Structure of the most dangerous modes

For a cold wall and all contact angles, or a hot wall and higher contact angles $\alpha > 102°$ we find an instability to a steady perturbation (fig. 3.18a,b,d,e) with a wavenumber $m_c = 2$. It consists of vortices, which can be seen in the horizontal cut with the plane $z = \Gamma/2$. The distance of the apparent centers of these vortices from the axis tends to increase (decrease) with z for a hot (cold) wall. The perturbation flow is alternatingly perpendicular and tangential to equidistant meridional planes separated by $\pi/4$.

For a hot wall and lower contact angles $\alpha < 102°$ the most dangerous perturbation is replaced by a traveling wave (fig. 3.18c,f) with a wavenumber $m_c = 1$. Again, the clockwise-rotating mode is displayed. One can identify two vortices in the cut at $z = \Gamma/2$ with a flow across the axis. Near the apex, the perturbation velocity is large compared to the rest of the droplet.

Dependence on the Prandtl number

The dependence of the neutral Reynolds number Re_n and of the critical frequency ω_c on the Prandtl number for $\alpha = 120°$ is shown in fig. 3.19. In the case of a cold wall, only the steady mode $m = 2$ is found. Re_c grows by at least one order of magnitude upon a small increase of $\mathrm{Pr} \sim \mathcal{O}(10^{-2})$. This is similar to the low-Pr instability in liquid bridges (see, e.g. Wanschura et al., 1995). In our case, the critical curve even turns backward. At higher Pr even the mode $m = 2$ becomes time-dependent, but its neutral Reynolds number is the much higher than that of the mode $m = 1$. For a higher contact angle in

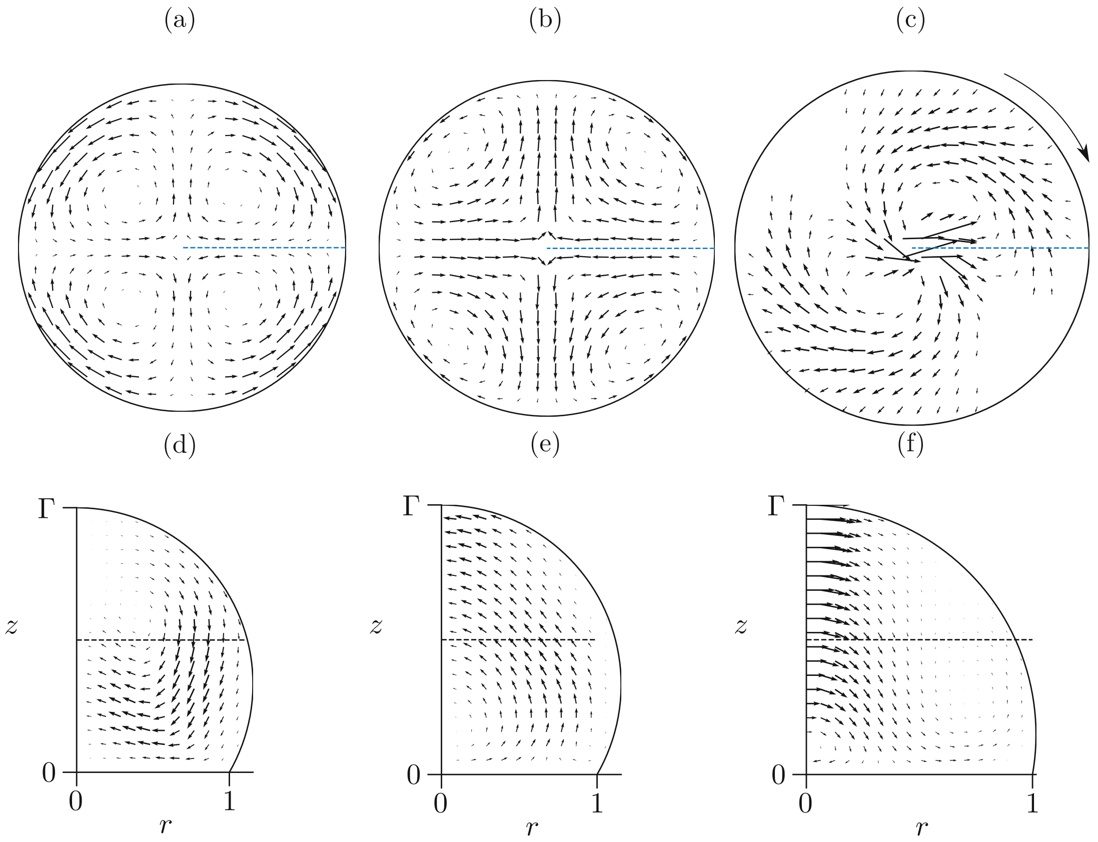

Figure 3.18: The most dangerous perturbation for $\mathrm{Pr} = 10^{-3}$ shown in the horizontal midplane $z = \Gamma/2$ indicated by the black dashed line (a-c) and in the meridional plane indicated by the blue dashed line (d-f). The parameters are: cold wall, $\alpha = 120°, \mathrm{Re}_c = 1700, m_c = 2, \omega_c = 0$ (a,d); hot wall, $\alpha = 120°, \mathrm{Re}_c = 3102, m_c = 2, \omega_c = 0$ (b,e); hot wall, $\alpha = 100°, \mathrm{Re}_c = 14622, m_c = 1, \omega_c = 286.7$ (c,f).

the range $130° \lessapprox \alpha \lessapprox 140°$, the stabilization of the basic state is weaker, and the critical curve can be continued to higher Pr. For a hot wall and $\alpha = 120°$ we find neutrally stable perturbation modes in the range $m \in \langle 1, 3\rangle$, and their neutral curves continue beyond $\mathrm{Pr} > 1$. For $m = 1$ and 3 the stabilization with Pr is weaker than for $m = 2$. Thus, the traveling wave $m = 1$ becomes more dangerous than the steady mode $m = 2$ for $\mathrm{Pr} > 2.181 \times 10^{-2}$. The frequency ω_c of the former decreases monotonically with the Prandtl number for $\mathrm{Pr} < 5$.

When the Prandtl number is increased, the stronger convection of heat within the fluid tends to homogenize the temperature distribution (fig. 3.20b) and decrease the thermocapillary stress (fig. 3.21a) in the lower part of the free surface. Thus, a higher Reynolds number would be needed to maintain the same strength of the thermocapillary flow (fig. 3.21b). For a hot wall, $\mathrm{Pr} = 1$ and $\mathrm{Re}_c = 8409$ the basic temperature field develops a thermal boundary layer near the wall (fig. 3.20b).

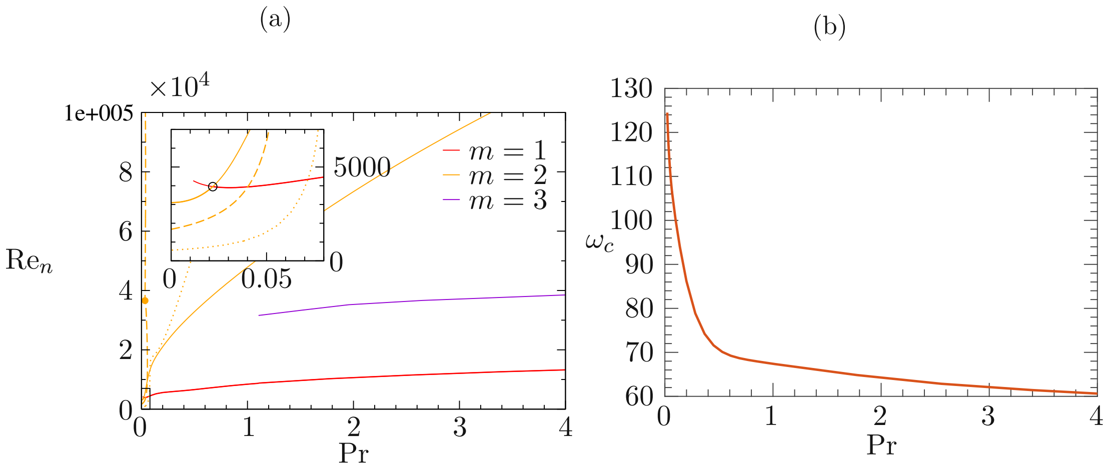

Figure 3.19: Dependence of the neutral Reynolds number Re_n for the azimuthal wave numbers coded by color (a) and of the critical frequency ω_c (b) on the Prandtl number Pr for a hot substrate with the contact angle $\alpha = 120°$ (full lines), cold substrate and $\alpha = 120°$ (dashed line), cold substrate and $\alpha = 140°$ (dotted line). The modes $m = 1$ (full red line) and for the hot wall, $\alpha = 120°$ and $\mathrm{Re}_n > 3.6 \times 10^4$ also $m = 2$ (dashed orange line above the orange dot) are time-dependent. Otherwise, the modes $m = 2$ and $m = 3$ are steady.

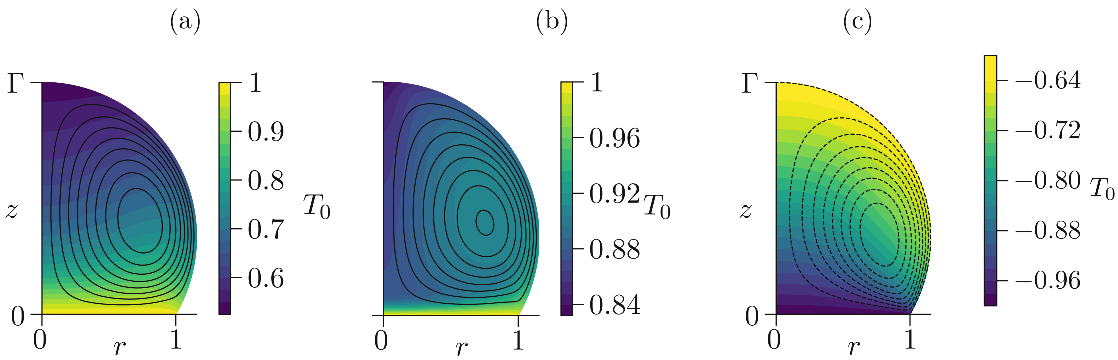

Figure 3.20: The marginally stable basic state for $\alpha = 120°$ and: hot wall, $\mathrm{Pr} = 2.1813 \times 10^{-2}, \mathrm{Re} = 3953$ (a); hot wall, $\mathrm{Pr} = 1, \mathrm{Re} = 8409$ (b); cold wall, $\mathrm{Pr} = 3.8 \times 10^{-2}, \mathrm{Re} = 3656$ (c).

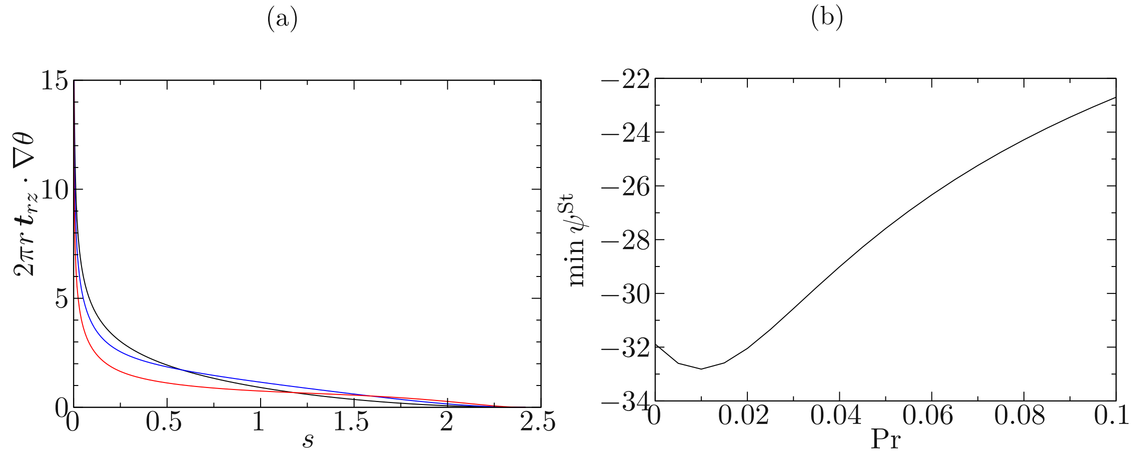

Figure 3.21: For hot wall, $\alpha = 120°$ and $\mathrm{Re} = 3953$: (a) The tangential temperature gradient at the free surface integrated in the azimuthal direction plotted against the path length s from the contact line to the apex for $\mathrm{Pr} = 0$ (black), $\mathrm{Pr} = 0.02$ (blue) and $\mathrm{Pr} = 0.1$ (red); (b) Dependence of the value of the Stokes stream function at the center of the basic vortex on the Prandtl number

The perturbation of the temperature field due to the steady mode $m = 2$ for the critical conditions at $\alpha = 120°$, small but non-zero Pr and either hot or cold wall is shown in fig. 3.22. In both cases, the velocity at the free surface is dominantly directed in the direction of the positive gradient of the surface temperature perturbation and thus against the thermocapillary stress induced by this perturbation. The thermocapillary stress, therefore, tends to suppress the perturbation flow, stabilizing the basic state upon an increase of Pr.

In case of the travelling wave $m = 1$ the perturbation velocity at the free surface for $\alpha = 120°, \mathrm{Pr} = 2.181 \times 10^{-2}$ becomes localized near the apex where the velocity aligns with the thermocapillary stress (fig. 3.23a-c). As the Prandtl number further increases along the critical curve to $\mathrm{Pr} = 1$ (fig. 3.23d-f), the extrema of the temperature perturbation at the free surface migrate closer towards the apex.

For both modes, $m = 1$ and $m = 2$, the extrema of the temperature perturbation are created in the bulk of the droplet by the action of the inertia-induced perturbation velocity acting on the internal basic temperature gradient.

3.4.3 Hydrothermal wave instability

For large contact angles ($\alpha \gtrsim 70°$) and high Prandtl numbers (the threshold depends on α), we find only the azimuthal wavenumber $m = 1$ to be the critical one. This is in qualitative agreement with the experiments of Watanabe et al. (2018). In addition to the traveling hydrothermal wave we also find a steady critical perturbation for $\mathrm{Pr} \sim \mathcal{O}(1)$ with a similar spatial structure to the traveling wave. In this section, we use the Marangoni

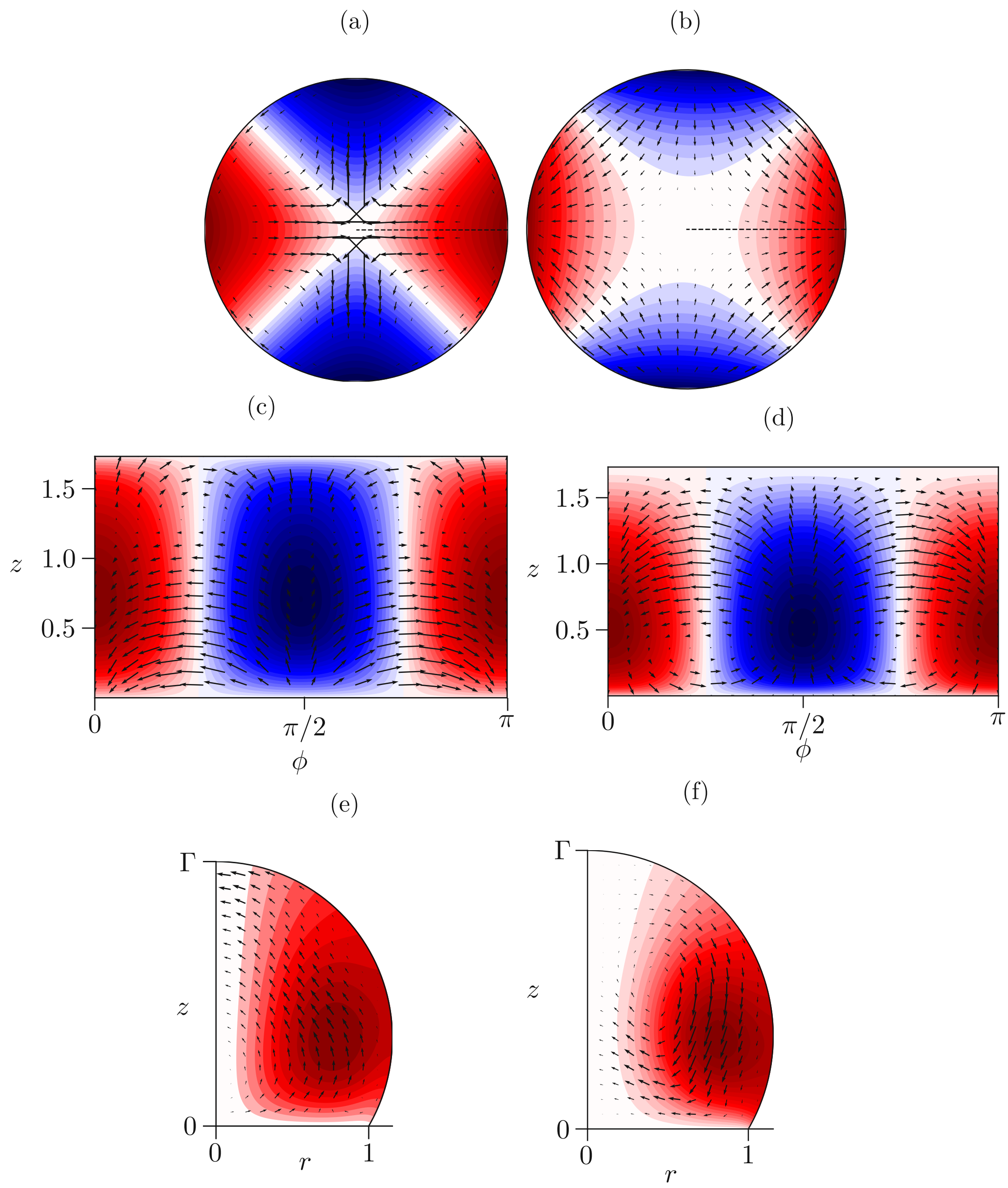

Figure 3.22: The temperature and velocity fields of the most dangerous mode at the free surface projected in axial (a,b) and radial (c,d) direction, and in a meridional cut indicated by the dashed line (e,f) for $\alpha = 120°, m_c = 2$ and hot wall, $\mathrm{Pr} = 2.1813 \times 10^{-2}, \mathrm{Re} = 3953$ (a,c,e); cold wall, $\mathrm{Pr} = 3.8 \times 10^{-2}, \mathrm{Re} = 3656$ (b,d,f) .

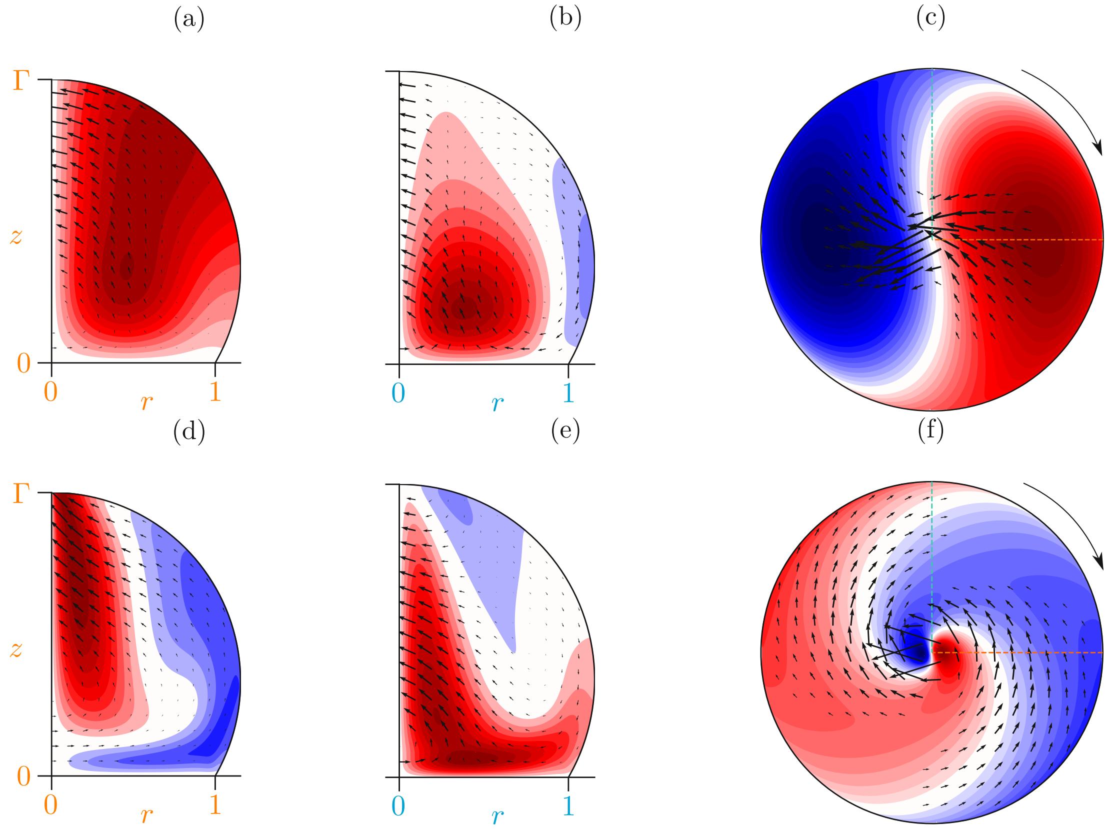

Figure 3.23: The most dangerous perturbation for a hot substrate, $\alpha = 120°, m_c = 1$ and: $\mathrm{Pr} = 2.1813 \times 10^{-2}, \mathrm{Re} = 3953$ (a,b,c), $\mathrm{Pr} = 1, \mathrm{Re} = 8409$ (d,e,f) . The right column shows the velocity and temperature at the free surface viewed from the top. The left (and the middle) column shows the meridional cuts corresponding to the cyan and orange dashed lines, respectively.

number $\mathrm{Ma} = \mathrm{RePr}$ as a suitable control parameter. The critical Marangoni number Ma_c and the oscillation frequency ω_c of the time-dependent modes decrease monotonically with α (fig. 3.24). For Ma_c the decrease is roughly exponential, at least within some range of α (depending on the other parameters). Again, we attribute the steep decrease of Ma_c with α to the growing size of the droplet relative to R, as in the case of the inertial instability.

For a cold wall, the dependence of Ma_c on Pr is similar to the Marangoni instability. Namely, Ma_c decreases steeply upon an increase of the Prandtl number for $\mathrm{Pr} \sim \mathcal{O}(1)$, but the slope of the decay decreases with increasing Pr (fig. 3.25a). In the case of a hot wall, the dependence is more complex. The critical curve of the low-Prandtl-number traveling wave with $m = 1$ (fig. 3.27a,b) described in sec. 3.4.2 continues for $\alpha = 120°$ up to the point A: $(\mathrm{Pr}, \mathrm{Ma}_c) = (5.0218, 67787)$ in fig. 3.25. Ma_c increases by two orders of magnitude from $\mathcal{O}(10^2)$ to $\mathcal{O}(10^4)$ as Pr increases from 0.1 to 5. At the point A, the

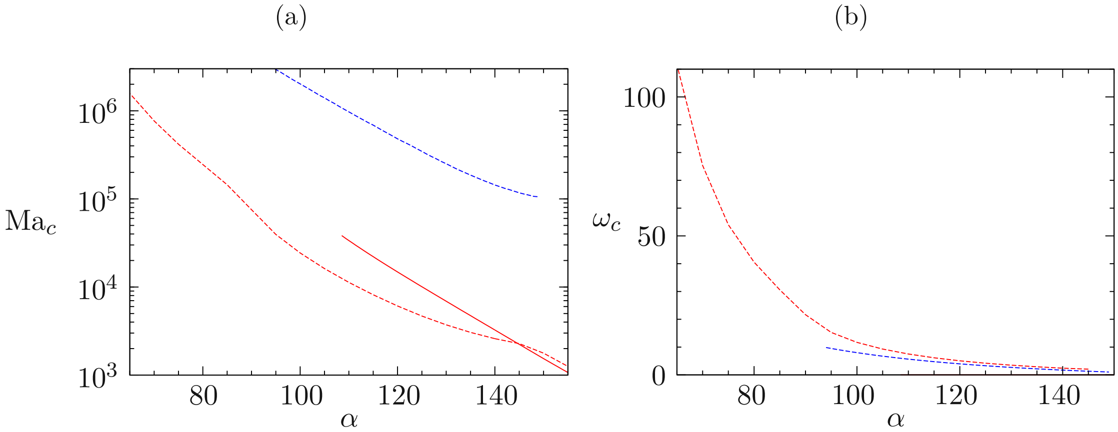

Figure 3.24: The dependence of the critical Marangoni number Ma_c (a) and of the critical frequency ω_c (b) on the contact angle α for a hot (red) and cold (blue) wall, $(\mathrm{Pr}, \mathrm{Bi}) = (16.36, 0.2362)$ (full line), $(\mathrm{Pr}, \mathrm{Bi}) = (28.1, 0.4)$ (dashed line). The critical azimuthal wave number is $m_c = 1$.

traveling wave is replaced by a steady mode with the same azimuthal wavenumber $m = 1$ (fig. 3.27c,d), which has a similar spatial structure as the traveling wave. In particular, it is characterized by a hot and a cold spot close to the apex. Ma_c drops by one order of magnitude upon a small increase of the Prandtl number from the point A to a local minimum of the critical curve at $(\mathrm{Pr}, \mathrm{Ma}_c) = (7.184, 8993)$. Afterward, Ma_c increases until the point B: $(\mathrm{Pr}, \mathrm{Ma}_c) = (16.36, 14833)$, where the steady mode is again replaced by a traveling wave. Upon a further increase of Pr from the point B both Ma_c and ω_c decrease. The critical Marangoni number saturates for $\mathrm{Pr} \gtrsim 50$ at $\mathrm{Ma}_c \approx 8750$.

In the case of a cold wall, the critical Marangoni number is one order of magnitude larger than for a hot wall. This is due to a layer of hot fluid that develops below the free surface (fig. 3.26c). The temperature gradient tangential to the free surface almost vanishes except in the close vicinity of the contact line. The thermocapillary driving of the basic flow is thus restricted to this small region. The basic state is shown for larger values of $\alpha = 140°, \mathrm{Pr} = 28.1$ and $\mathrm{Bi} = 0.4$ compared to the values considered in the case of a hot wall. With this choice, the order of magnitude of $\mathrm{Ma}_c \sim \mathcal{O}(10^5)$ for the cold wall is comparable to the typical values obtained for the hot wall for lower values of α, Pr and Bi.

For lower contact angles ($\alpha \sim 90°$), the critical Marangoni number is large even for a hot wall. The thermal convection is thus intense compared to thermal conduction. The variation of the basic temperature within the droplet at criticality is smaller than for higher α with lower Ma_c. The basic state exhibits a thin thermal boundary layer at the wall (fig. 3.26a). In the bulk, the vertical temperature gradient is inverted in some regions. The horizontal component of the temperature gradient reaches magnitudes comparable to the vertical one. In the case of the hot wall, there is a column of cold fluid near the axis in the upper part of the droplet.

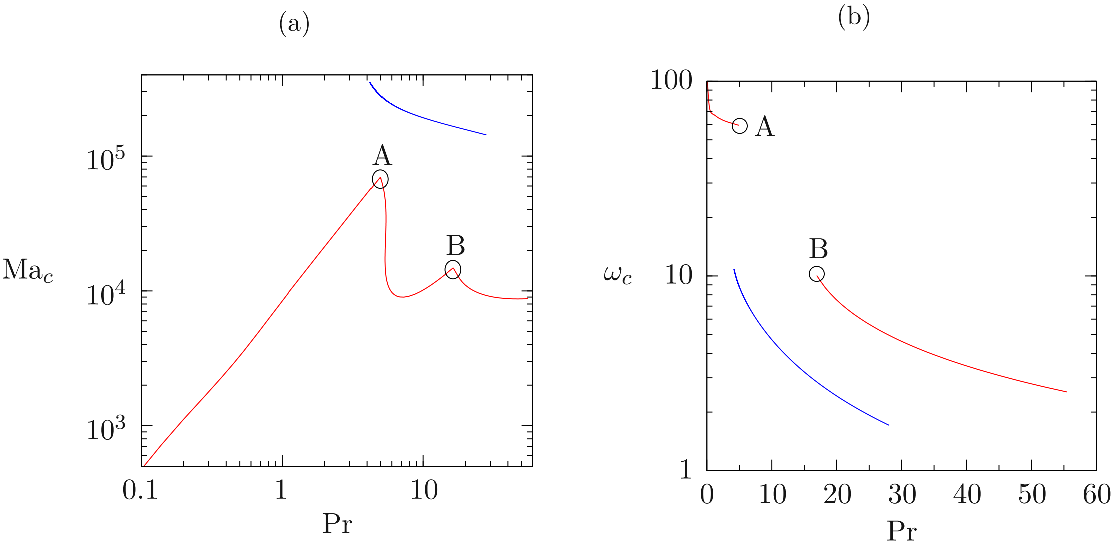

Figure 3.25: Critical Marangoni number Ma_c (a) and critical oscillation frequency ω_c (b) as functions of the Prandtl number for a hot wall, $\alpha = 120°, \mathrm{Bi} = 0.2362$ (red), and for a cold wall, $\alpha = 140°, \mathrm{Bi} = 0.4$ (blue). The critical azimuthal wavenumber is $m_c = 1$. Between the points A and B on the red curve $\omega_c = 0$.

The different structure of the basic temperature field for hot and cold wall leads to a different structure of the most dangerous perturbation. For a hot wall (fig. 3.27), the perturbation is dominated by a displacement of the column of cold fluid, which is located below the apex in the basic state, by a perturbation vortex with $m = 1$. The displacement of the cold fluid is manifested by two columns of positive and negative temperature perturbation close to the axis at opposite sides. The vortex is driven by a localized thermocapillary stress at the apex due to the extrema of the temperature perturbation, which are located close to the apex. In the case of the steady mode (fig. 3.27c,d), the perturbation flow is tangential to the meridional plane containing the extrema of the temperature perturbation and perpendicular to the perpendicular meridional plane.

In the case of a cold wall, the velocity perturbation has a similar structure, but it is not so localized near the apex as in the hot wall case. For illustration, the most dangerous mode is plotted in fig. 3.28 for $\alpha = 140°$ and $\mathrm{Bi} = 0.4$. Two vortices are visible in a horizontal cut $z = \Gamma/2$. The perturbation flow creates extrema of the temperature perturbation in the bulk of the droplet from the internal basic temperature gradient. In the horizontal cut, the temperature perturbation has a Yin-Yang shape. The temperature perturbation almost vanishes at the free surface. This is due to the layer of hot fluid near the free surface in the basic state which suppresses perturbations of the free-surface temperature by the mechanism described by Pearson (1958).

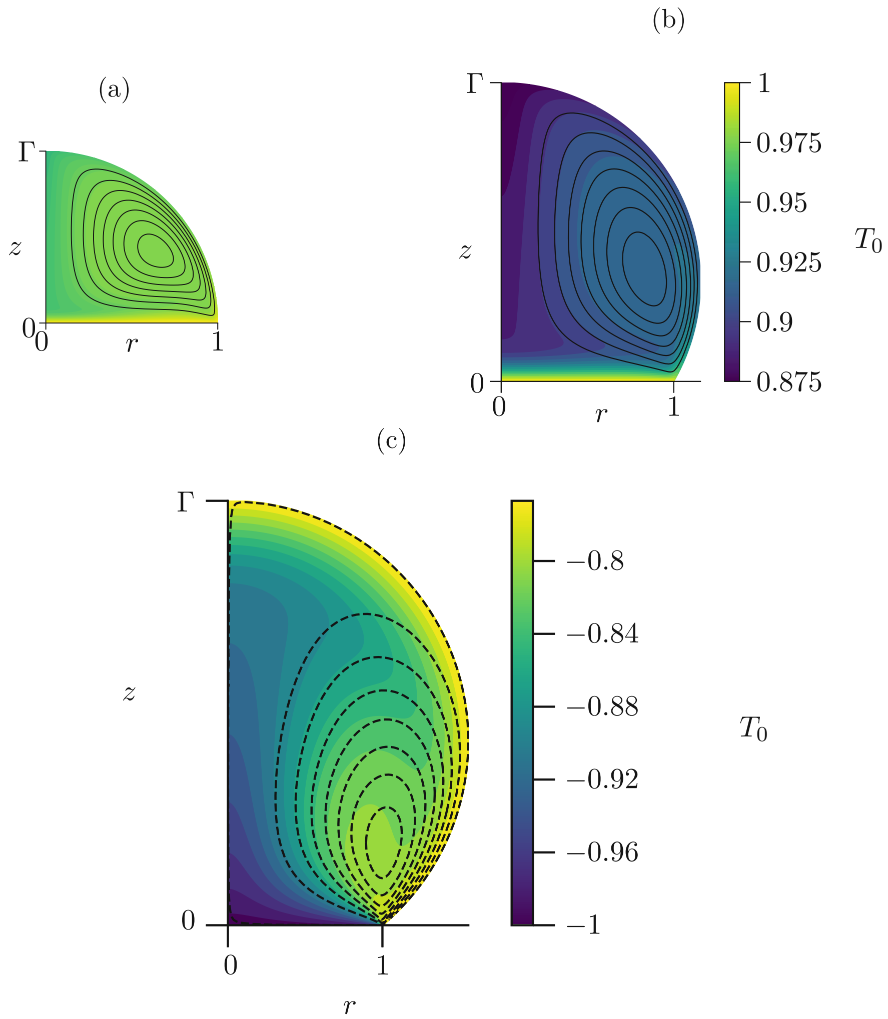

Figure 3.26: The marginally stable basic state for: (a) hot wall, $\alpha = 90°, \mathrm{Pr} = 16.36, \mathrm{Bi} = 0.2362, \mathrm{Ma}_c = 276602$; (b) $\alpha = 120°, \mathrm{Pr} = 16.36, \mathrm{Bi} = 0.2362, \mathrm{Ma}_c = 14833$; (c) cold wall, $\alpha = 140°$, $\mathrm{Pr} = 28.1$, $\mathrm{Bi} = 0.4, \mathrm{Ma}_c = 143820$.

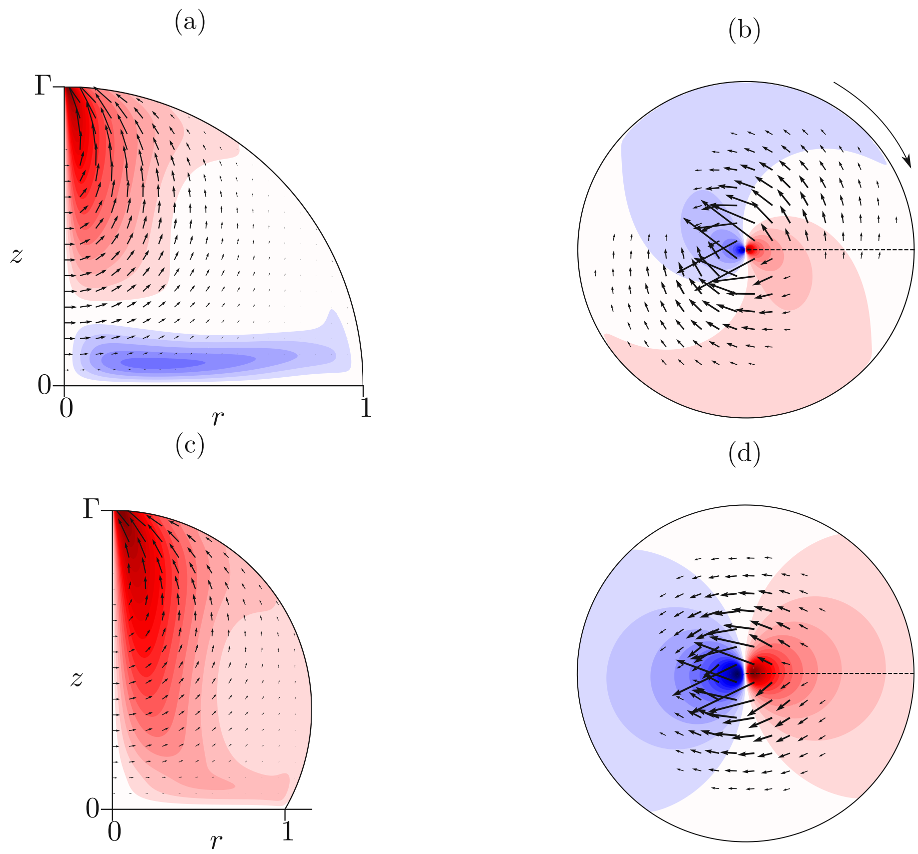

Figure 3.27: The most dangerous modes with $m_c = 1$ for a hot wall, $\mathrm{Pr} = 16.36$, $\mathrm{Bi} = 0.2362$ and (a–b) $\alpha = 90°$, $\mathrm{Ma}_c = 276602$, $\omega_c = 55.6$; (c–d) $\alpha = 120°$, $\mathrm{Ma}_c = 14833$, $\omega_c = 0$. The perturbation of velocity (arrows) and temperature (color) is shown: (a,c) in a meridional cut containing the maximum of the temperature perturbation, as indicated by the dashed line in (b) and (d), respectively; (b,d) at the free surface viewed from the top. The direction of propagation of the traveling wave (a,b) is clockwise.

3.5 Summary

We observe three more or less distinct types of instability. For high-Pr small-α droplets on a hot wall, we find Marangoni instability in the central part of the droplets. This is in qualitative agreement with other numerical studies (Karapetsas et al., 2012; Shi et al., 2017). The critical azimuthal wavenumber depends sensitively on α. For very small α, the Marangoni cells are steady. When α increases, the critical Marangoni number rises steeply, and the critical mode becomes time-dependent.

The Marangoni cells (or rolls) do not arise near the contact line, as observed in evaporating droplets on walls of finite conductivity experimentally by Sefiane et al. (2010) and in the three-dimensional time-dependent simulations of Zhu and Shi (2021). It should be noted that the convection cells near the contact line were also not found by the linear stability

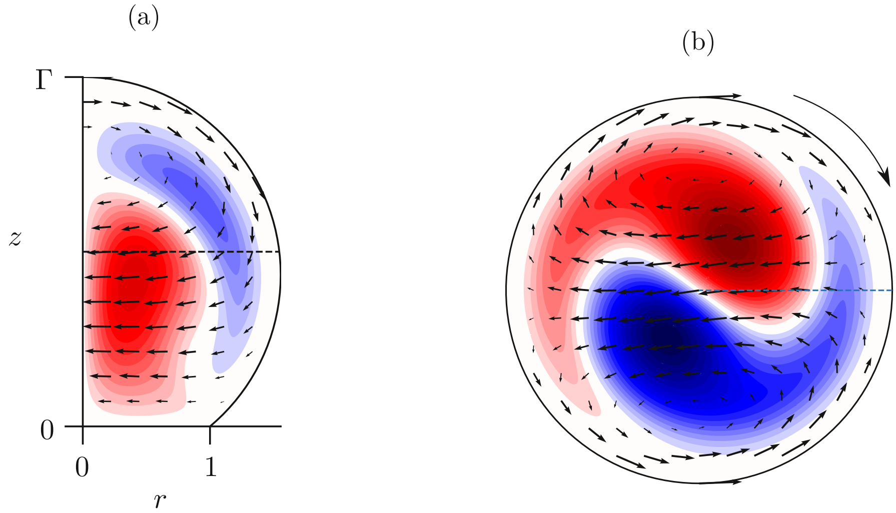

Figure 3.28: The clockwise-rotating most dangerous mode with $m_c = 1$ and $\omega = 1.71$ for a cold wall, $\alpha = 140°$, $\mathrm{Pr} = 28.1$ and $\mathrm{Bi} = 0.4$. The perturbation of velocity (arrows) and temperature (color) is shown in (a) a meridional cut indicated by the dashed line in (b), (b) the horizontal cut at $z = \Gamma/2$ indicated by the dashed line in (a).

analysis of Karapetsas et al. (2012), who imposed an evaporation heat flux at the free surface and a constant temperature of the wall. Karapetsas et al. (2012) found the same structure of Marangoni cells as presented here in section 3.4.1. Furthermore, it is shown by Sefiane et al. (2010) that the conductivity of the substrate favors the occurence of the cells. Thus, the discrepancy cannot be attributed to the simplifications of the thermal boundary conditions with the Newton's law of cooling at the free surface and a perfectly conducting wall. Instead, the inability to find the cells near the contact line may be related to the limitations of the linear stability theory which cannot capture subcritical instabilities (e.g. due to backward bifurcation). It has been illustrated in fig. 3.10 that a subcritical Marangoni instability can indeed occur in shallow droplets. This speculation is further supported by the three-dimensional time-dependent numerical simulations of Kumar et al. (2022), which show that Marangoni cells originate in the central part of the droplet, as predicted by our results, and subsequently trigger smaller cells closer to the contact line in the course of time.

In the limit of small Prandtl number $\mathrm{Pr} \ll 1$, we find an instability for higher contact angles ($\alpha \gtrsim 90°$) to a steady perturbation with $m = 2$. The structure of the perturbation is very similar for the hot and cold walls. The neutral Reynolds number of this perturbation mode grows steeply when Pr is increased to small non-zero values $\sim \mathcal{O}(10^{-2})$, since the perturbation of the thermocapillary stress is directed against the perturbation flow. In the case of a hot wall, there is, in addition, a time-dependent perturbation mode $m = 1$, which becomes the most dangerous one when Pr is increased. This perturbation mode displaces a region of cold fluid in the basic state from the apex, which produces a thermocapillary driving of the perturbation flow. The critical curve of the $m = 1$ mode continues to high Prandtl numbers.

For high Pr and α we find instability only to $m_c = 1$. The structure of the basic temperature field and of the most dangerous mode depends on whether the wall is hotter or colder than the ambient. For a hot wall, the critical curve is continued from the low-Prandtl-number instability. The perturbation mode can be either steady or traveling, depending on the values of Pr and α. For a cold wall, the extrema of the temperature perturbation are located in the interior of the droplet, while at the free surface, the temperature perturbation is only very weak. A layer of hot fluid below the free surface in the basic state suppresses perturbations of the free surface temperature. This leads to much larger Ma_c compared to the hot wall.

CHAPTER 4

The onset of chaotic advection in a thermocapillary-driven droplet on a wall

4.1 Motivation

In droplets hanging from a hot horizontal wall (or rod), particle accumulation structures (PAS) have been observed experimentally by Takakusagi and Ueno (2017) and Watanabe et al. (2018). The flow in which the PAS have been observed was three-dimensional and time-dependent due to the hydrothermal wave (HTW) instability. Although the investigation of the accumulation mechanism in this particular flow geometry is lacking, the observed structures are very similar to those found in liquid bridges (Schwabe et al., 2006, and others). It has been shown (see, e.g. Hofmann and Kuhlmann, 2011; Kuhlmann and Muldoon, 2012; Mukin and Kuhlmann, 2013) that in the latter setup, solid neutrally buoyant particles of finite size can accumulate inside or near Kolmogorov-Arnold-Moser (KAM) tori, which approach sufficiently close to some impenetrable boundary (wall or free surface). The transport mechanism of particles from the sea of chaotic trajectories onto KAM tori is due to repulsive force between the particle and a boundary, either by direct contact or by the lubrication effect. Thus, the typical prerequisite for accumulation of density-matched particles is that their size is comparable to the minimal distance of a KAM torus from the boundary. Kuhlmann and Muldoon (2013) however show that PAS can also appear in the chaotic sea when collisions of the particles with boundaries repeatedly return them to the same section of some open chaotic trajectory. For a review, see Romanò and Kuhlmann (2019).

This chapter aims to compute the Lagrangian topology in a flow comparable to Watanabe et al. (2018) and correlate it to their particle accumulation structures. The KAM tori are computed in a moving frame of reference which rotates together with the traveling hydrothermal wave. In such frame, the flow as well as the KAM tori are steady and three-dimensional. We consider droplets attached to a hot wall with large contact angles ($\alpha \geq 90°$) and high Prandtl numbers ($\mathrm{Pr} = 28.1, 68.4, 207$), corresponding to 2, 5, and 20 cSt silicone oils at 20°C. The Biot number of 0.3 is employed throughout this chapter, unless stated otherwise. The Biot number typically shifts the critical Marangoni number but does not have other significant qualitative effects.

4.2 Methodology

Similar as Kuhlmann and Muldoon (2012) we construct a model flow which aims to approximate the true three-dimensional flow at supercritical conditions. Here, the model is constructed as a superposition of the basic flow and the critical mode with positive ω (i.e, rotating in the negative ϕ direction), in a co-rotating reference frame with an azimuthal phase velocity $-\omega/m$. The model flow in the rotating frame reads

$$\boldsymbol{u}_m(r,\phi,z) = \boldsymbol{u}_0 + \frac{\omega}{m} r \boldsymbol{e}_\phi + a_T \frac{\max T_0 - \min T_0}{\max \hat{T}} \left(\hat{\boldsymbol{u}} \exp(\mathrm{i}m\phi) + \mathrm{c.\ c.} \right). \tag{4.1}$$

The term $(\omega/m) r \boldsymbol{e}_\phi$ is an additional azimuthal component of the basic velocity field due to the rotation of the reference frame. The perturbation mode is re-normalized with the factor $(\max T_0 - \min T_0)/\max \hat{T}$ such that a_T is the amplitude of the temperature perturbation relative to the maximum variation of the basic temperature field $(\max T_0 - \min T_0)$. Thus, a_T can be compared to the experiments where the basic temperature as well as the temperature perturbation have been measured by infrared imaging (Takakusagi and Ueno, 2017). The model (4.1) is expected to approximate the three-dimensional flow for slightly supercritical conditions.

The model flow (4.1) is interpolated onto a finer mesh (obtained by applying the FEniCS function `refine` to the computational mesh) and evaluated at $n_\phi = 400$ uniformly distributed meridional planes. The values of the flow variables at element vertices are imported to ParaView 5.10.1 (Ayachit, 2015), where the fluid trajectories are computed with the adaptive-step 5th order Runge–Kutta method (2.24) implemented in the filter `Stream Tracer`. A Poincaré section is then defined as a `Slice` (i.e., an intersection with a given plane) of the trajectories. The meridional plane containing the global maximum of the temperature perturbation, which is located near the apex, is used as the Poincaré plane.

Vertices of the same triangular element at two adjacent meridional planes form a three-dimensional cell. The grid of cells is divided into sub-domains, which are distributed among MPI ranks using the filter `D3`. The trajectories are started from random positions within the droplet (corresponding to the seed type `Point Cloud`), such that they are distributed among the sub-domains. Nevertheless, no satisfactory parallelization of the computation of trajectories has been achieved by this workflow - at best, 3 out of 12 available MPI ranks have been active at a time. This identifies a large potential for improvement of parallel efficiency of the computation.

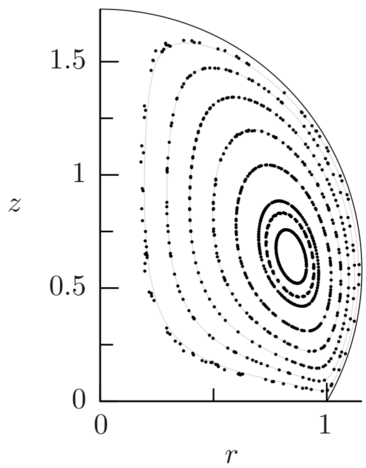

Figure 4.1: Poincaré section of fluid trajectories in the basic flow (in a rotating frame of reference) compared to the contour lines of the Stokes stream function. See text for the physical and numerical parameters.

4.2.1 Verification

The accuracy of the trajectory computation is assessed by comparing the Poincaré section for $a_T = 0$ at an arbitrary meridional plane to the contour lines of the Stokes stream function of the basic flow for the following parameters: $\mathrm{Re} = 329, \alpha = 120°, \mathrm{Pr} = 28.1, \mathrm{Bi} = 0.2362$. The computational mesh for the basic state and the perturbation is adapted as follows: The finite elements within the distance $d_1 = 0.05$ from the wall and the apex are divided into halves, compared to the basic mesh in the bulk. The elements within the distances 7.5×10^{-4} from the apex and $d_2 = 5 \times 10^{-3}$ from the contact line are further divided into quarters. The number of elements along the free surface per $\pi/2$ radians is set to sN^2, where $N = n/\sqrt{\Gamma}$ corresponds to the number of elements per unit length in the bulk and $s = 0.5, n = 70$ are numerical parameters. The penalization factor for the Nitsche method is set to $C = 500$. These parameters lead to sufficiently accurate streamlines and fluid trajectories (fig. 4.1) with acceptable numerical cost. The trajectory started at the outermost streamline in fig. 4.1 deviates slightly from the streamline due to numerical error. The Poincaré points presented in this chapter should thus be understood with small error bars. Other trajectories in fig. 4.1 match perfectly with the streamlines. In general, the numerical error tends to increase with increasing distance from the vortex center due to the increased length of the trajectory and due to the streamline crowding near the free surface. It is obvious that any normal offset from the exact streamline created by numerical error near the free surface becomes magnified in the low-velocity region near the axis $r = 0$.

α \ Pr	28.1	68.4	207
90°	(98 238, 21.55)	(54 345, 6.600)	(55 152, 2.238)
100°	(31 647, 11.69)	(25 544, 4.417)	(26 929, 1.537)
110°	(14 444, 7.461)	(13 133, 3.037)	(14 291, 1.083)
120°	(7 658, 5.020)	(7 329, 2.120)	(8 310, 0.7795)

Table 4.1: The critical Marangoni numbers and critical oscillation frequencies $(\mathrm{Ma}_c, \omega_c)$ for the range of parameters considered in this chapter. The wall is hot, the Biot number is $\mathrm{Bi} = 0.3$ and the wave number is $m = 1$.

4.3 Results

First, we investigate the effect of the perturbation amplitude a_T on the topology of fluid trajectories for a representative case $\alpha = 90°, \mathrm{Pr} = 68.4$ and $\mathrm{Ma}_c = 54345$. Afterwards, the effects of the contact angle and Prandt number for selected amplitudes are considered. The azimuthal wavenumber is $m = 1$ and the frequencies are $\omega > 0$ throughout this chapter. The critical Marangoni numbers and oscillation frequencies for the cases considered in this chapter are indicated in table 4.1.

For the perturbation amplitudes $a_T \sim 0.01$, the trajectories remain regular except possibly next to the boundaries, and the majority of them lie on primary KAM tori similar to streamlines of the unperturbed basic flow. A secondary set of KAM tori (blue in fig. 4.2a) of period 1 emerges by resonance from a closed trajectory orbiting around the center of the basic toroidal vortex. The size of this set grows when the amplitude increases, and saturates at $a_T \approx 2\%$ for the selected parameters $\alpha = 90°, \mathrm{Pr} = 68.4$. For $a_T = 0.05$, a subharmonic torus of period 3 is observed in the outer part of the basic vortex (red in fig. 4.2b), approaching very close to the free surface. The minimum distance from the free surface of the trajectory on this torus is 3.5×10^{-3} at $(r, \phi, z) = (0.9773, 1.395\ \mathrm{rad}, 0.1948)$, where ϕ is measured from the position of the maximum positive temperature perturbation.

Chaotic trajectories are visible for $a_T \geq 0.05$ in this outermost region of the basic vortex. The extent of the chaotic sea grows with a_T, at the expense of the tori. Resonances occasionally occur near the borders of the regular islands. For $a_T \gtrapprox 0.06$ (fig. 4.2c), the chaotic sea is also observable along the homoclinic connection separating the primary (black) and the secondary (blue) set of the nested KAM tori, and the primary tori become more and more displaced away from the center of the basic vortex. For $a_T \gtrapprox 0.3$ (fig. 4.2e) both the primary and the secondary set orbit about the center of the basic vortex. Subharmonic tori with small cross-sections and higher periodicities (~ 10) are typically found near the outermost secondary torus for $0.1 \leq a_T \leq 0.3$.

For a given amplitude $a_T \sim \mathcal{O}(1\%)$ and $\alpha = 90°$ the topology is not very sensitive to the Prandtl number for high values ($\mathrm{Pr} = 68.4$ and $\mathrm{Pr} = 207$). But when Pr is decreased to 28.1 (leading to an increase of the critical Reynolds number), the secondary set of KAM tori vanishes (fig. 4.3a). For higher amplitudes $a_T \sim \mathcal{O}(10\%)$ the set of primary tori

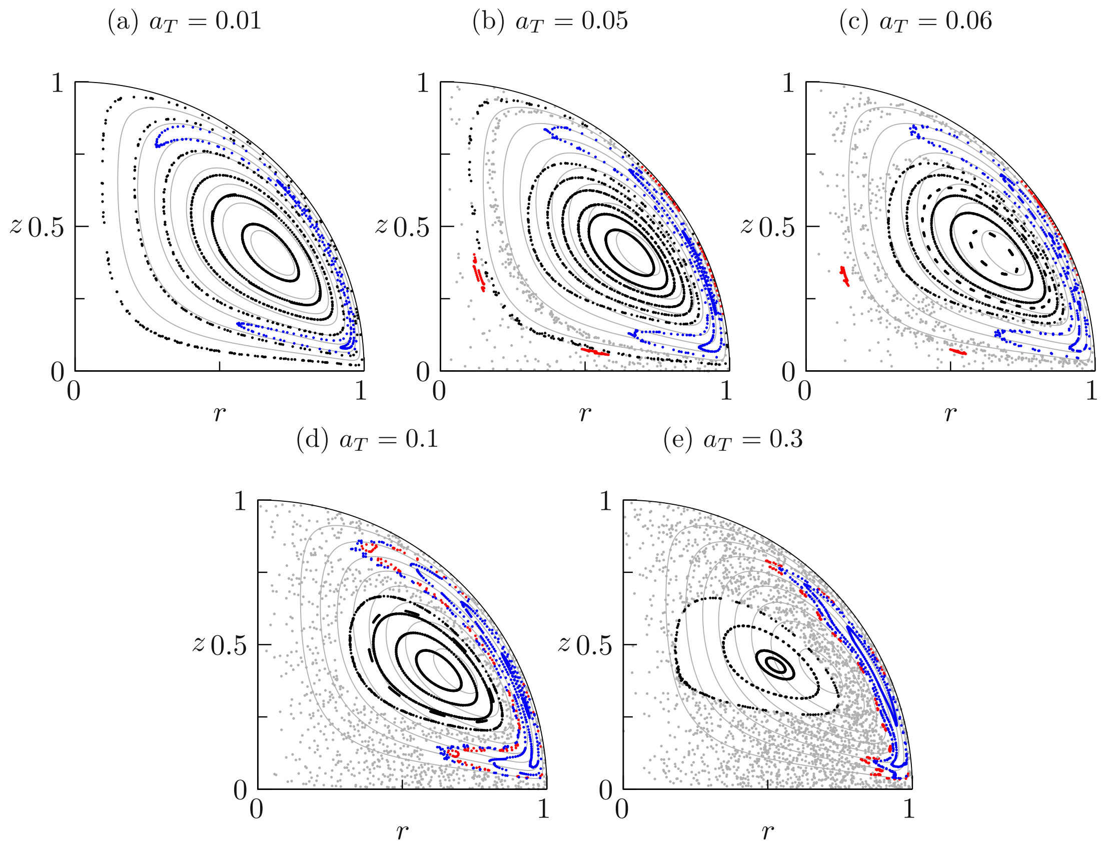

Figure 4.2: Poincaré sections of fluid trajectories for different perturbation amplitudes a_T (indicated in sub-captions) and $\alpha = 90°, \mathrm{Pr} = 68.4, \mathrm{Bi} = 0.3$. The grey lines in the background are the streamlines of the basic flow. Grey dots are the intersections of chaotic trajectories, black dots indicate regular trajectories belonging to the primary KAM tori, blue dots correspond to the secondary synchronous tori, and dots of other colors indicate subharmonic tori. The periodicities of the subharmonic tori in (d) and (e) are 11 and 16, repsectively.

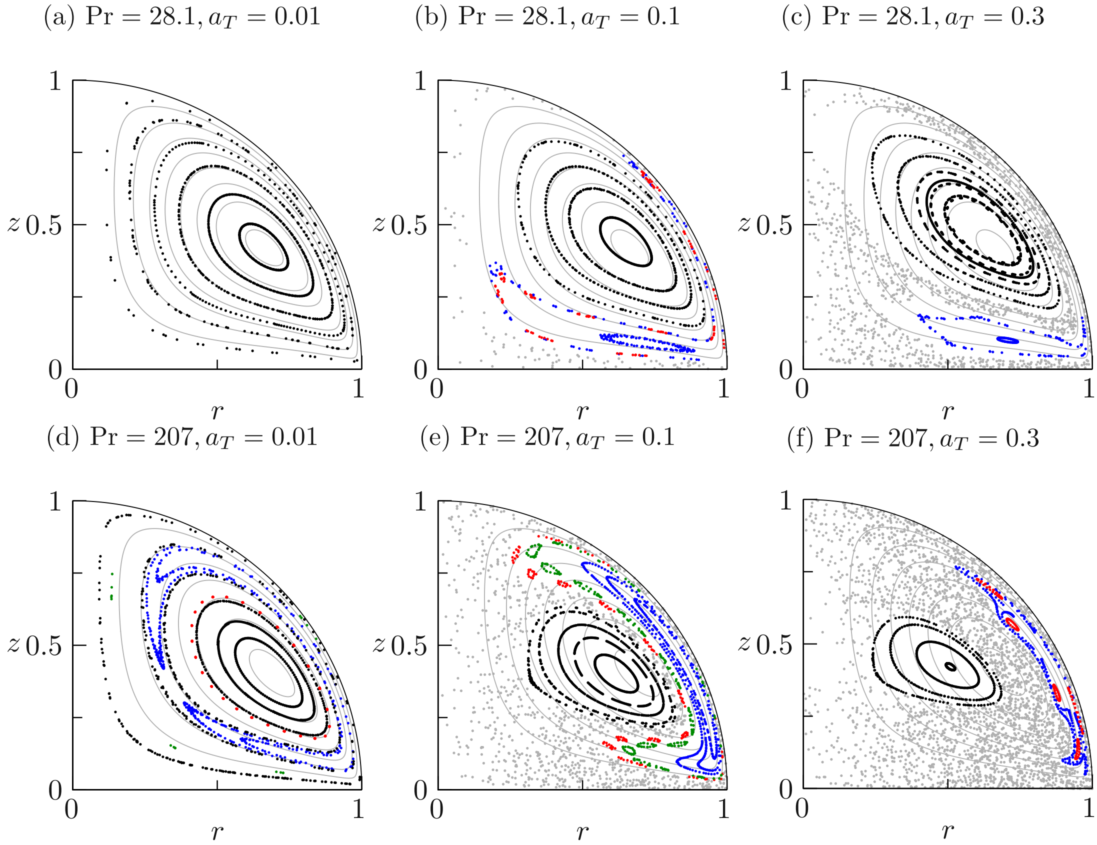

Figure 4.3: Poincaré section of fluid trajectories in the model flow for $\alpha = 90°$ and different Pr and a_T as indicated in the sub-captions. Colors and other parameters as in fig. 4.2.

shrinks and the extent of the chaotic sea increases when the Prandtl number is increased (fig. 4.3b,c,e,f). This dependence is, however, only weak, and the topology is very similar across the range of Pr considered.

When the contact angle is increased from 90° up to 120°, the secondary tori migrate towards the center of the basic vortex (fig. 4.4). This indicates that the resonance between the wave speed ω/m and the rotational frequency of the basic vortex occurs closer to the vortex center. The effect of the contact angle on the topology of trajectories is stronger for higher Prandtl numbers. For Pr = 207 there remains only one set of nested KAM tori when the contact angle is increased from 110° to 120° with $a_T = 0.01$ (fig. 4.4c,f), or when a_T is increased from 0.03 to 0.1 for $\alpha = 110°$ (fig. 4.5g,h). When a_T is further increased from 0.1 to 0.3 for Pr = 207 and $\alpha = 110°$, the second set of tori appears again (black in fig. 4.5i).

The topology becomes more sensitive to a_T at higher contact angles (compare figs. 4.2 and 4.3 to 4.5). For a given value of a_T the extent of the chaotic sea typically increases

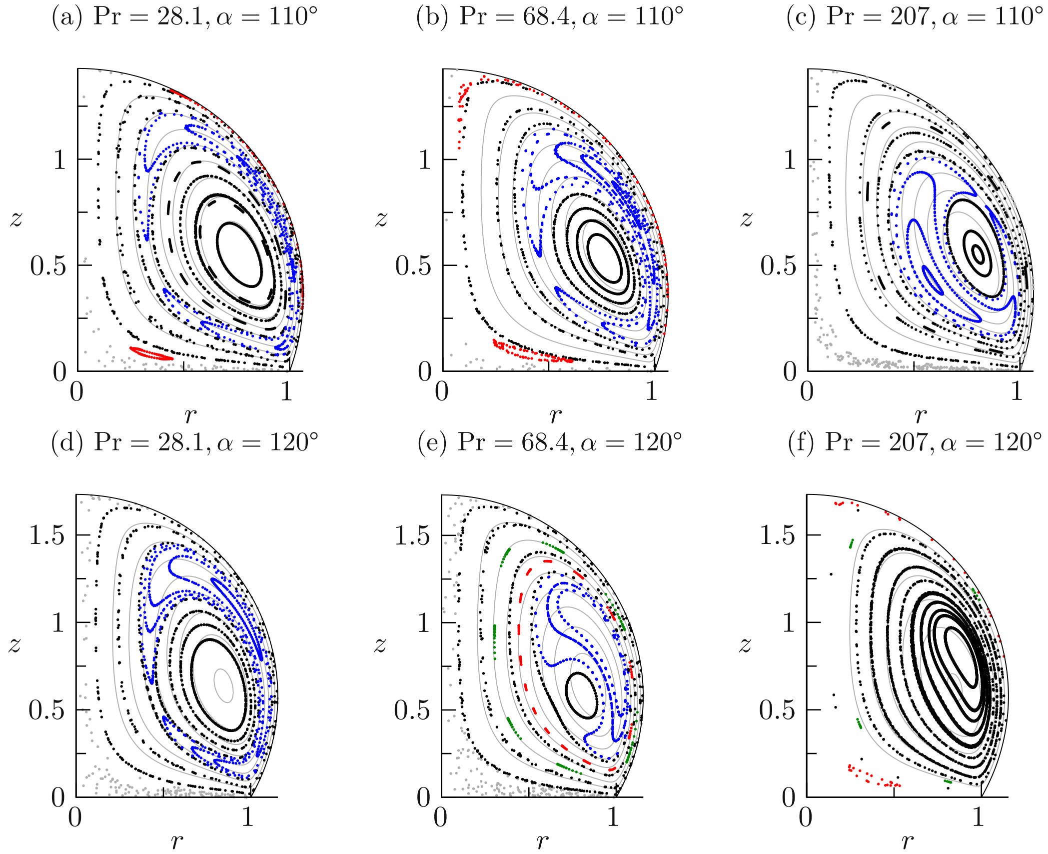

Figure 4.4: Poincaré sections of fluid trajectories in the model flow for $a_T = 0.01$ and different Pr and α (indicated in sub-captions). Colors as in fig. 4.2.

with α. For example, with $\alpha \geq 110°$, some chaotic trajectories and subharmonic tori are observable even at perturbation amplitude as low as $a_T = 0.01$ (fig. 4.4a-c).

4.3.1 Three-dimensional structure of the KAM tori

In this sub-section, examples of the three-dimensional structure of the KAM tori are provided for $a_T = 0.3$. The primary and the secondary tori of period 1 together form two interlocked rings (fig. 4.6). The proportion of the sizes of the outermost secondary and primary tori increases with the Prandtl number, and the extent of the chaotic sea increases with the Prandtl number and the contact angle.

The primary torus is displaced, compared to the unperturbed basic streamlines, by the perturbation velocity. Thus, it is shifted towards the apex in the region where the perturbation velocity transports hot fluid from the bulk towards the apex, and away from it on the other side of the droplet where a perturbation flow from the apex into the bulk is associated with a negative temperature perturbation (fig. 4.7). On the other

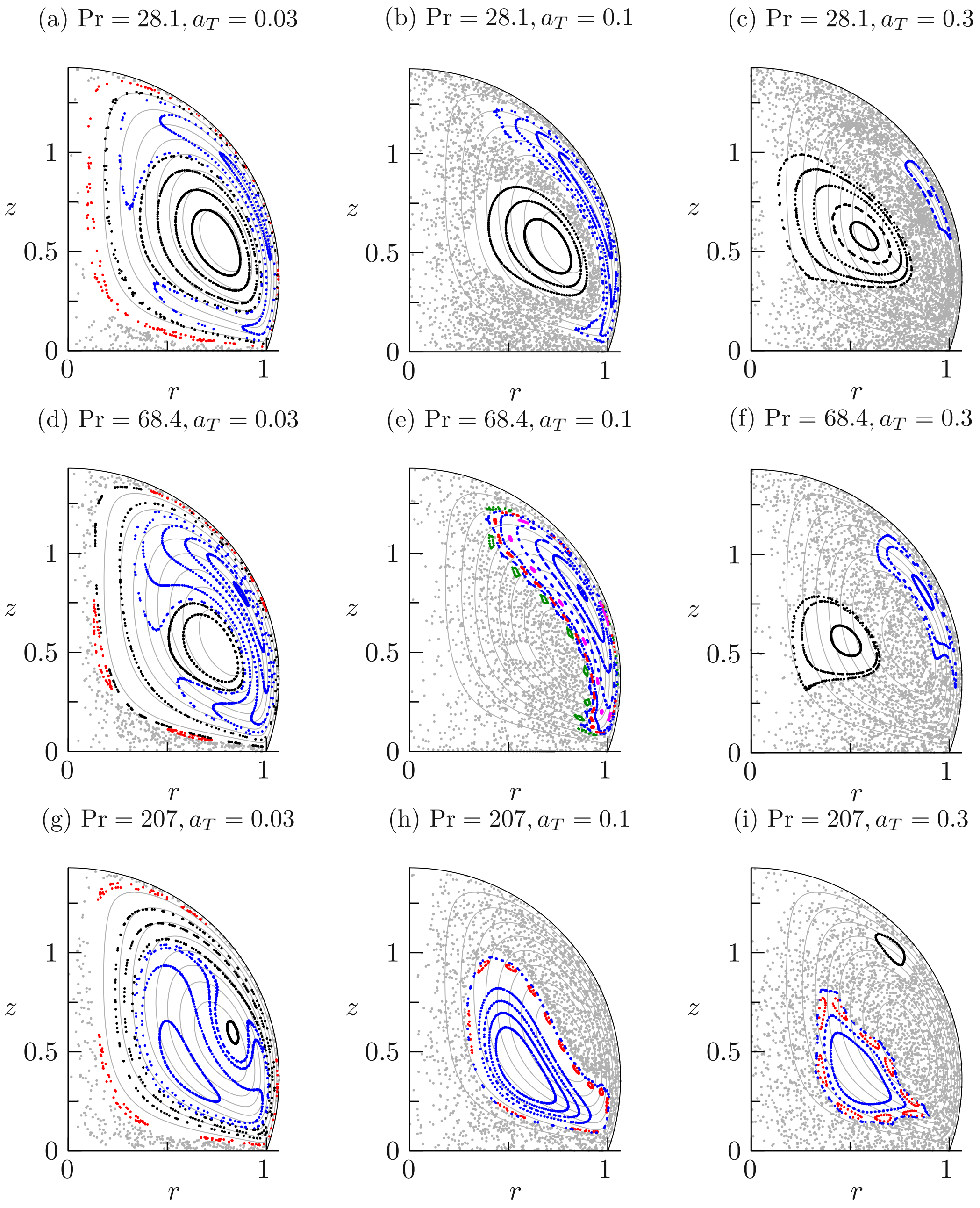

Figure 4.5: Poincaré sections for $\alpha = 110°$ and different Pr and a_T as indicated in the sub-captions. Colors as in fig. 4.2.

(a) $\alpha = 90°, \mathrm{Pr} = 28.1$ (b) $\alpha = 90°, \mathrm{Pr} = 68.4$ (c) $\alpha = 90°, \mathrm{Pr} = 207$

(d) $\alpha = 110°, \mathrm{Pr} = 28.1$ (e) $\alpha = 110°, \mathrm{Pr} = 68.4$ (f) $\alpha = 110°, \mathrm{Pr} = 207$

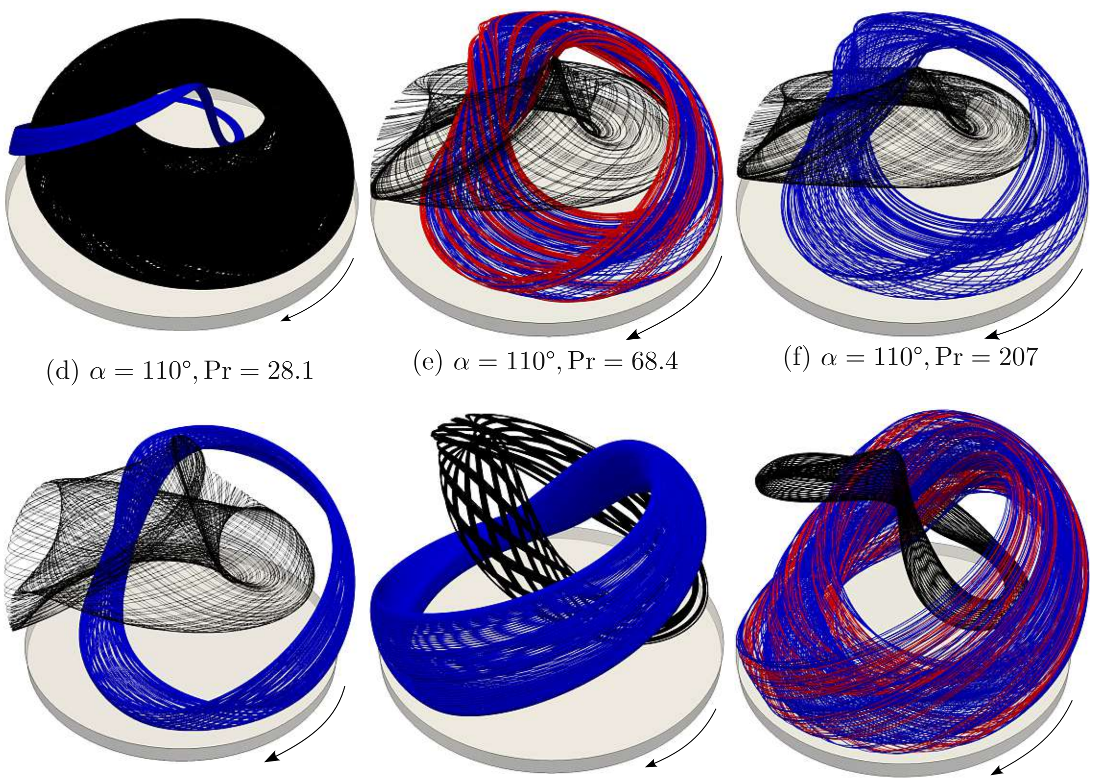

Figure 4.6: Regular trajectories (colored as in fig. 4.2) on the outermost reconstructed KAM tori for $a_T = 0.3$ and selected α and Pr (indicated in sub-captions). The arrows indicate the sense of rotation of the tori in the laboratory frame. In the co-rotating frame the tori are steady and the base rotates in opposite direction.

hand, the secondary torus approaches the apex on the side of the dominant downward perturbation flow, and the contact line on the side of the upward perturbation flow.

On the primary tori, which originate from the streamlines of the basic vortex, the regular trajectories typically wind about the central closed trajectory with rather uniform speed along the azimuth. On the other hand, on the secondary tori the trajectories make most of the winding near the axis of the droplet, while they do not wind significantly near the free surface. The winding is typically slower on the secondary tori compared to the primary tori.

The secondary torus for $\alpha = 90°, \mathrm{Pr} = 68.4$ and $a_T = 0.2$ is compared in fig. 4.8 to the particle accumulation structures (PAS) reported by Takakusagi and Ueno (2017) and Watanabe et al. (2018) from terrestrial and on-orbit experiments. In the case of the terrestrial conditions the shape of the droplet is significantly deformed due to gravity (fig. 4.8e). The particles approaching the apex along the free surface are not easily visible in

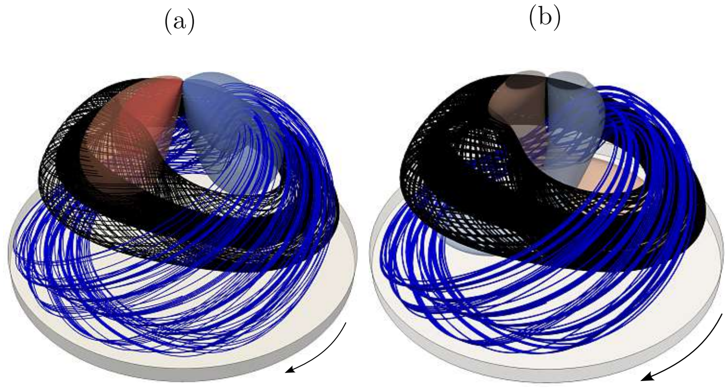

Figure 4.7: Regular trajectories (black and blue lines) and contours of the vertical velocity perturbation (semi-transparent surfaces in (a)) and temperature perturbation (semi-transparent surfaces in (b)) for $\alpha = 90°, \mathrm{Pr} = 68.4$ and $a_T = 0.3$. The red and blue color of the surfaces indicates positive and negative values.

the photographs, but the complete closed structure is sketched in fig. 4 (3) of Takakusagi and Ueno (2017). The general structure of the PAS agrees with the secondary torus, but the solid particles approach closer to the apex and they travel towards the wall closer near the axis. This is also evident from the three-dimensional reconstruction of particle trajectories provided in fig. 8 (2) of Takakusagi and Ueno (2017). This might either indicate that the PAS is located in the chaotic sea near the secondary torus, or it might be a consequence of the different shape of the droplet, buoyancy or nonlinear effects in the supercritical flow.

As far as the perturbation of the free-surface temperature is considered, we find a very good qualitative agreement with the experiments (fig. 4.8g,h). Thus, the simplified thermal boundary condition at the free surface employed in our model seems to have a minor effect on the instability.

As pointed out in the motivation of this chapter, the prerequisite for accumulation of neutrally buoyant particles on a KAM torus is that the size of the particles is comparable to the smallest distance of the torus from a boundary. Therefore, the smallest dimensionless distance d of regular trajectories from the free surface and the location (ϕ_d, z_d) of the closest approach are provided for selected cases in tab. 4.2. Again, ϕ_d is measured from the location of the maximum temperature perturbation. The closest approach of the secondary torus to a distance $d = 7.72 \times 10^{-3}$ from the free surface is observed for $(\alpha, \mathrm{Pr}, a_T) = (90°, 68.4, 0.3)$ close to the contact line. For a larger contact angle $\alpha = 110°$ and the same $\mathrm{Pr} = 68.4$ and $a_T = 0.3$ it is the primary torus which approaches closer to the free surface than the secondary torus. But the minimal distance $d = 8 \times 10^{-3}$ is very similar to the former case. The primary and the secondary tori approach the free surface at the opposite sides of the droplet.

The scaled radii of the particles employed in the terrestrial and on-orbit experiments

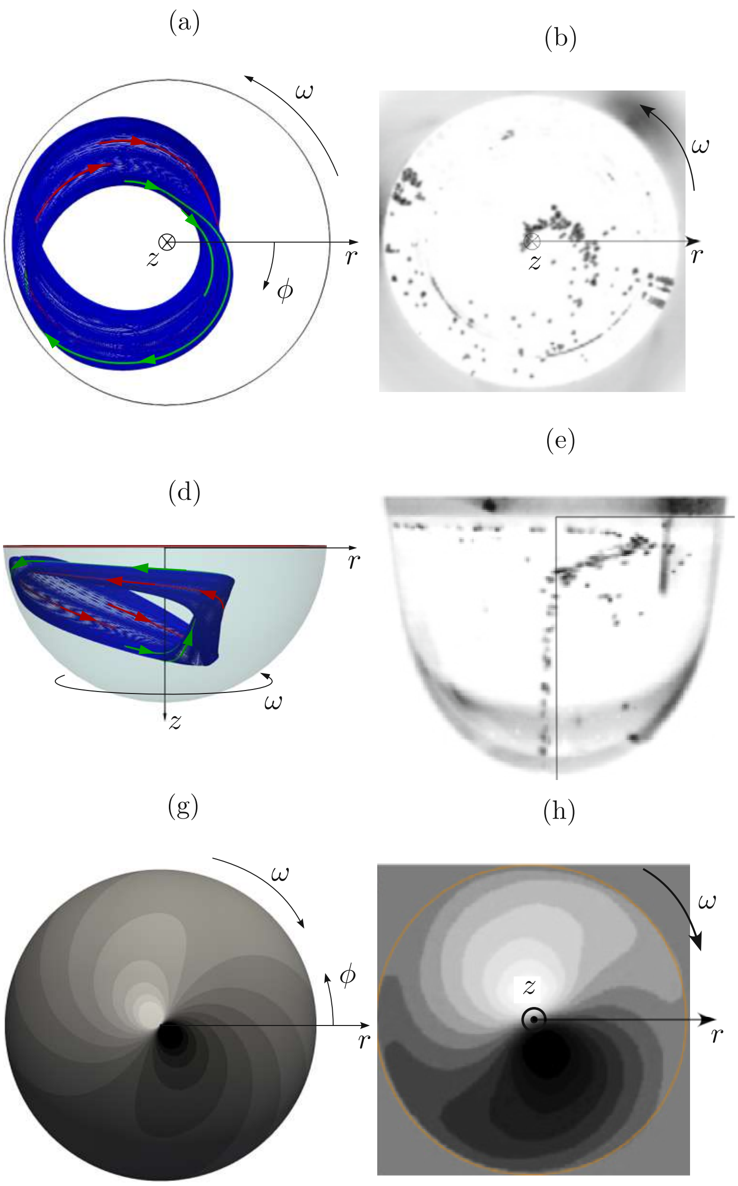

Figure 4.8: The secondary KAM torus (a,d) for $\alpha = 90°$, $\mathrm{Pr} = 68.4$ and $a_T = 0.2$ compared to PAS observed in terrestrial experiments by Takakusagi and Ueno (2017) for the same Pr (b,e), and in on-orbit experiments by Watanabe et al. (2018) (c,f). The perturbation of the free-surface temperature from our linear stability analysis (g) is compared to the infrared imaging from the terrestrial experiments (h) provided by Watanabe et al. (2018). The top, middle and bottom rows show the views from the top through the transparent wall into the droplet, from the side and from below, respectively. The red and green curves with arrows in (a) and (b) are short sections of the blue regular trajectory. The arc arrows in (a–d and g–h) indicate the sense of rotation of the structures in the laboratory frame.

α	Pr	a_T	d	ϕ_d [rad]	z_d
90°	68.4	0.3	7.72×10^{-3}	0.528	0.184
90°	68.4	0.5	1.06×10^{-2}	−2.314	0.312
90°	207	0.3	9.70×10^{-3}	0.443	0.187
110°	28.1	0.3	1.04×10^{-2}	−2.771	0.377
110°	68.4	0.3	8.00×10^{-3}	−2.650	0.381

Table 4.2: The smallest distance d of a KAM torus from the free surface, and the position of the closest approach (ϕ_d, z_d) for selected combinations of α, Pr and a_T. ϕ_d is measured from the position of the maximum temperature perturbation.

reported by Watanabe et al. (2018) were 0.005, 0.006 and 0.0075. These values are only slightly lower than those of the smallest distance d between the tori and the free surface, listed in tab. 4.2. It is expected that there remains a lubrication film between the particles and the free surface, such that the minimal distance of the particle centroids form the free surface remains larger than their radii (Romanò, Wu and Kuhlmann, 2019).

4.4 Discussion

Within the range of parameters considered in this chapter, the critical frequency ω_c of the most dangerous mode $m_c = 1$ is such that in the reference frame which rotates with the azimuthal velocity of the critical mode, the basic state contains two closed trajectories of period one in the bulk of the droplet. In addition to the trivial closed trajectory at the center of the basic toroidal vortex, there exists a second one that winds about the center of the vortex once per revolution of the critical mode. This second closed trajectory gives rise to secondary KAM tori when the basic flow is perturbed by the critical mode. Qualitatively, the same flow topology has been found in the supercritical flow in a high-Prandtl-number liquid bridge by Barmak et al. (2021).

The secondary tori typically approach close to the free surface, especially for higher a_T and lower Pr and α. Finite-size neutrally buoyant particles can therefore be transported from the chaotic sea onto the KAM tori due to repulsion by the free surface. For $\alpha = 90°$, the general three-dimensional structure of the secondary tori (fig. 4.8a,d) agrees with the shape of the particle accumulation structures reported in figs. 1 and 4(3) of Takakusagi and Ueno (2017). For Pr = 68.4, the tori are stretched along the free surface, while they are rather compact near the axis $r = 0$. This is due to the larger magnitude of the basic velocity near the free surface and the related streamline crowding. In the experiments, the particles indeed seem rather dispersed near the free surface.

With our model flow (4.1), rather large perturbation amplitudes $a_T \sim \mathcal{O}(10\%)$ are necessary to obtain a sufficient extent of the chaotic sea. This is significantly larger than the colormap limits of the temperature perturbation employed, e.g., in fig. 7 of Watanabe et al. (2018). It is, however, pointed out by Takakusagi and Ueno (2017) that the temperature variation visualized by the infrared imaging is more of a qualitative nature.

Furthermore, the amplitudes considered in this chapter are beyond the assumption of an infinitesimal perturbation, which was employed to justify neglecting the non-linear terms in the equations for the perturbation. Our results can therefore be compared only qualitatively to the real supercritical flow.

CHAPTER 5

Conclusions

All topics of this work are related to the stability and streamline topology in boundary-driven flows. The interest comes from the fact that solid particles of finite size with a density similar to that of the carrier fluid may cluster into non-trivial line-like particle accumulation structures (PAS) in such flows (Romanò, Wu and Kuhlmann, 2019). Namely, PAS have been observed in a three-dimensional lid-driven cavity (Romanò, Kannan and Kuhlmann, 2019; Wu et al., 2021) and in thermocapillary flows (Schwabe et al., 2006; Takakusagi and Ueno, 2017). The occurrence of accumulation structures requires either three-dimensional or time-periodic flow. Under steady two-dimensional boundary conditions (and source terms, if present), the three-dimensional flow (e.g., in the form of cells or hydrothermal waves) can be born out of the basic steady two-dimensional flow by a flow instability.

Owing to the lower computational requirements and better accuracy by which time-periodic two-dimensional flows can be computed as compared to three-dimensional flows, preference was given to the former case in chapter 2, where the structure of fluid trajectories in a time-periodic two-dimensional lid-driven cavity has been investigated. Several results have been accumulated, extending the ranges of parameters considered by other investigators. A parametric study of the topology of fluid trajectories and of the mixing capability of the flow has been conducted for the case of zero mean velocity of the lid. It is shown that for a given Reynolds number, there exists an optimal frequency for fast mixing, which arises as a trade-off between the extent of the sea of chaotic pathlines and the duration of the driving cycle.

It was, however, observed that the time scales for particle accumulation in this system are too large to be of practical relevance, either due to long driving periods ($\mathrm{Str}^{-1} \gtrapprox 20$) or due to long time scales of net advection in the bulk of the cavity ($\sim 10^3\times$ the convective time scale L/U for $\mathrm{Str} = 1$ and $\mathrm{Re} \sim 10^2$). The most promising combination of parameters for particle accumulation seems to be $\mathrm{Str} = 0.25$ and $\mathrm{Re} = 50$. As an extension of this work, the potential for particle accumulation could be investigated by computing the transport of finite-size density-matched particles, modeling particle-wall collisions as, e.g., in Hofmann and Kuhlmann (2011).

In the next step, the creation of three-dimensional flows by an instability of a thermocapillary flow in a droplet adhering to a wall was investigated in detail by means of linear stability analysis. Three more or less distinct regions of instability have been identified, namely

- the Marangoni instability in high-Prandtl-number low-contact-angle droplets on a hot wall,
- purely inertial instability for very-low-Prandtl-number high-contact-angle droplets,
- hydrothermal wave instability for high-Prandtl-number high-contact-angle droplet.

The Marangoni instability creates convection cells in the central part of the droplet. The structure of these cells agrees well with the linear stability analysis of Karapetsas et al. (2012). We find neutrally stable perturbations over a spectrum of azimuthal wave numbers with similar neutral Marangoni numbers. Shi et al. (2017) show that for some parameters, the convection cells of different wave numbers coexist in the three-dimensional flow at different radial distances from the center of the droplet. The fact that Shi et al. (2017) observe the cells even at Marangoni numbers significantly lower than the critical values determined by the present linear stability analysis for the same parameters indicates that the bifurcation of the basic state might be backward. We indeed find a backward bifurcation giving rise to steady axisymmetric convection cells. Another three-dimensional transient numerical study of Kumar et al. (2022) indicates that cells originating near the center of the droplet can trigger a sub-critical emergence of smaller cells closer to the contact line, which are commonly observed experimentally in evaporating droplets Sefiane et al. (2010). As an extension of this work, the nonlinear bifurcation of the basic flow into the three-dimensional state(s) should be investigated in more detail by three-dimensional numerical simulations or experiments.

For the hydrothermal wave instability in droplets on a hot wall, the structure of the most dangerous perturbation agrees very well with the experimental results of Watanabe et al. (2018). The present analysis provides further insight into the instability mechanism. The basic state contains a region of cold stagnant fluid at the apex. Above the critical Marangoni number, the location of this *cold spot* becomes unstable to any displacement along the free surface. The displacement of the cold spot induces a perturbation of the thermocapillary stress at the apex. The induced thermocapillary stress drives a perturbation vortex which in turn amplifies the displacement. The perturbation vortex is asymmetric with respect to the meridional plane of the displacement of the cold spot. This asymmetry is related to a rotation of the perturbation about the axis of the droplet. For intermediate Prandtl numbers $\mathrm{Pr} \sim 1$, the hydrothermal wave is replaced by a steady perturbation mode of a similar spatial structure. For both the hydrothermal wave and the steady mode, the extrema of the temperature perturbation are located very close to the free surface. Thus, this instability differs from a typical hydrothermal wave instability, for which the extrema of the temperature perturbation are located in the bulk of the fluid.

To the best of the author's knowledge, this is the first work presenting a hydrothermal wave instability in droplets on a cold wall and an inertial instability in adhering droplets for small Prandtl numbers $\mathrm{Pr} \ll 1$.

For a cold wall, the hydrothermal wave instability has a typical structure. Extrema of the temperature perturbation are created in the bulk of the droplet from basic internal temperature gradients by a perturbation flow. The temperature perturbation diffuses up to the free surface, causing a weak perturbation of the free surface temperature. The induced perturbation of the thermocapillary stress drives the perturbation flow. Apart from the internal temperature gradients, the basic flow is characterized by a layer of hot fluid that forms below the free surface. This layer tends to suppress the perturbations of the free-surface temperature. Consequently, the critical Marangoni number is approximately one order of magnitude larger compared to a droplet on a hot wall for the same parameters. This might explain why this instability has not been reported previously in the literature.

The inertial instability for low Prandtl numbers $\mathrm{Pr} \ll 1$ has a similar critical Reynolds number and structure of the most dangerous perturbation for both the cold and the hot wall. The perturbation vortices create a temperature perturbation in the bulk of the droplet and at the free surface. The perturbation of the thermocapillary stress acts against the perturbation flow at the free surface. Thus, the critical Reynolds number grows steeply when the Prandtl number is increased.

Although buoyancy and static surface deformation have been neglected in chapter 3, it is shown in section 3.2.1 that both effects are non-negligible for millimeter-sized droplets in terrestrial gravity. Thus, another natural continuation of this work would be to consider the effect of gravity on the aforementioned instabilities.

As a by-product of the linear stability analysis, the supercritical nonlinear flow in the thermocapillary-driven droplet on a wall is approximated qualitatively by a superposition of the basic flow at the linear stability threshold and the most dangerous perturbation mode. The structure of fluid trajectories in this model flow is investigated for a range of perturbation amplitudes a_T. Such conditions are selected for which particle accumulation structures have been observed experimentally, as reported in the literature. For the relative amplitude of perturbation $a_T \sim \mathcal{O}(1\%)$, we observe the emergence of secondary tori orbiting about the basic toroidal vortex. These periodically approach the free surface and the wall near the contact line. At higher perturbation amplitudes $a_T \sim \mathcal{O}(10\%)$ and contact angles $\alpha \gtrapprox 110°$, the primary tori vanish, and the chaotic sea fills most of the domain, while only the secondary tori remain. This topology of fluid trajectories is similar to that found in liquid bridges. Solid particles can accumulate on the secondary tori, or on the subharmonic tori which occasionally appear in the chaotic sea for some parameters. The general structure of the secondary tori agrees with the shape of the experimentally observed particle accumulation structures reported in the literature.

The approximation of the supercritical flow as a superposition of the basic flow and the leading perturbation mode is, of course, an oversimplification of the problem. The results of chapter 4 should thus be understood only as first-order estimates. The predicted structure of the KAM tori should be confirmed by computing fluid trajectories in flows obtained from three-dimensional numerical simulations.

Minimal model problems have been employed throughout this thesis in order to isolate the essential physics and for the sake of generality and reproducibility of the results. A natural continuation of this work would be to confirm the predictions by relaxing the simplifying assumptions and increasing the level of detail of the model. To that end, some potential extensions of this study have been indicated above.

Bibliography

Albensoeder, S., Kuhlmann, H. C. and Rath, H. J. (2001*a*), 'Multiplicity of steady two-dimensional flows in two-sided lid-driven cavities', *Theor. Comp. Fluid Dyn.* **14**, 223–241.

Albensoeder, S., Kuhlmann, H. C. and Rath, H. J. (2001*b*), 'Three-dimensional centrifugal-flow instabilities in the lid-driven cavity problem', *Phys. Fluids* **13**, 121–135.

Alnaes, M. S., Blechta, J., Hake, J., Johansson, A., Kehlet, B., Logg, A., Richardson, C., Ring, J., Rognes, M. E. and Wells, G. N. (2015), 'The FEniCS project version 1.5', *Arch. Numer. Softw.* **3**, 9–23.

Anderson, P. D., Galaktionov, O. S., Peters, G. W. M., van de Vosse, F. N. and Meijer, H. E. H. (2000), 'Chaotic fluid mixing in non-quasi-static time-periodic cavity flows', *Int. J. Heat Fluid Flow* **21**, 176–185.

Aref, H. (1984), 'Stirring by chaotic advection', *J. Fluid Mech.* **143**, 1–21.

Aref, H., Blake, J. R., Budišić, M., Cardoso, S. S. S., Cartwright, J. H. E., Clercx, H. J. H., El Omari, K., Feudel, U., Golestanian, R., Gouillart, E., van Heijst, G. F., Krasnopolskaya, T. S., Le Guer, Y., MacKay, R. S., Meleshko, V. V., Metcalfe, G., Mezić, I., de Moura, A. P. S., Piro, O., Speetjens, M. F. M., Sturman, R., Thiffeault, J.-L. and Tuval, I. (2017), 'Frontiers of chaotic advection', *Rev. Mod. Phys.* **89**, 025007 (66pp).

Arnold, V. I. (1963), 'Small denominators and problems of stability in classical and celestial mechanics', *Russ. Math. Surv.* **18**, 85–191.

Ayachit, U. (2015), *The ParaView Guide: A Parallel Visualization Application*, Kitware.

Barmak, I., Romanò, F. and Kuhlmann, H. C. (2021), 'Finite-size coherent particle structures in high-Prandtl-number liquid bridges', *Phys. Rev. Fluids* **6**, 084301 (36pp).

Bhardwaj, R. (2018), 'Analysis of an evaporating sessile droplet on a non-wetted surface', *Colloids Interface Sci. Commun.* **24**, 49–53.

Birkhoff, G. D. (1934), *Nouvelles recherches sur les systèmes dynamiques...*, Ex aedibus academicis in Civitate Vaticana.

Botella, O. and Peyret, R. (1998), 'Benchmark spectral results on the lid-driven cavity flow', *Comput. Fluids* **27**, 421–433.

Brutin, D., Sobac, B., Loquet, B. and Sampol, J. (2011), 'Pattern formation in drying drops of blood', *J. Fluid Mech.* **667**, 85–95.

Brutin, D., Sobac, B., Rigollet, F. and Le Niliot, C. (2011), 'Infrared visualization of thermal motion inside a sessile drop deposited onto a heated surface', *Exp. Therm. Fluid Sci.* **35**, 521–530.

Burguete, J., Mukolobwiez, N., Daviaud, F., Garnier, N. and Chiffaudel, A. (2001), 'Buoyant-thermocapillary instabilities in extended liquid layers subjected to a horizontal temperature gradient', *Phys. Fluids* **13**, 2773–2787.

Chien, W.-L., Rising, H. and Ottino, J. M. (1986), 'Laminar mixing and chaotic mixing in several cavity flows', *J. Fluid Mech.* **170**, 355–377.

Davis, S. H. (1987), 'Thermocapillary instabilities', *Annu. Rev. Fluid Mech.* **19**, 403–435.

Deegan, R. D., Bakajin, O., Dupont, T. F., Huber, G., Nagel, S. R. and Witten, T. A. (1997), 'Capillary flow as the cause of ring stains from dried liquid drops', *Nature* **389**, 827–829.

des Boscs, P.-E. and Kuhlmann, H. C. (2021), 'Stability of obliquely driven cavity flow', *J. Fluid Mech.* **928**, A25 (42pp).

Dormand, J. R. and Prince, P. J. (1980), 'A family of embedded Runge–Kutta formulae', *J. Comput. Appl. Math.* **6**, 19–26.

Farazmand, M. and Haller, G. (2012), 'Computing Lagrangian coherent structures from their variational theory', *Chaos* **22**, 013128 (12pp).

Fischer, P. F., Lottes, J. W. and Kerkemeier, S. G. (2008), 'nek5000 Web page'.
URL: *http://nek5000.mcs.anl.gov*

Franjione, J. G., Leong, C.-W. and Ottino, J. M. (1989), 'Symmetries within chaos: a route to effective mixing', **1**, 1772–1783.

Garnier, N. and Chiffaudel, A. (2001), 'Two dimensional hydrothermal waves in an extended cylindrical vessel', *Eur. Phys. J. B* **19**, 87–95.

Gavrilina, A. A. and Barash, L. Y. (2021), 'Modeling unsteady Bénard-Marangoni instabilities in drying volatile droplets on a heated substrate', *J. Exp. Theor. Phys.* **132**, 302–312.

Gelfgat, A. Y., Bar-Yoseph, P. Z., Solan, A. and Kowalewski, T. A. (1999), 'An axisymmetry-breaking instability of axially symmetric natural convection', *Int. J. Transp. Phenom.* **1**, 173–190.

Guha, R., Mohajerani, F., Mukhopadhyay, A., Collins, M. D., Sen, A. and Velegol, D. (2017), 'Modulation of spatiotemporal particle patterning in evaporating droplets: Applications to diagnostics and materials science', *Appl. Mater. Interfaces* **9**, 43352–43362.

Gupta, M. M., Manohar, R. P. and Noble, B. (1981), 'Nature of viscous flows near sharp corners', *Comput. Fluids* **9**, 379–388.

Haller, G. (2015), 'Lagrangian coherent structures', *Annu. Rev. Fluid Mech.* **47**, 137–162.

Helleman, R. H. (1980), Self generated chaotic behavior in nonlinear mechanics, *in* E. G. D. Cohen, ed., 'Fundamental problems in statistical mechanics V: Proceedings of the 5th International Summer School on Fundamental Problems in Statistical Mechanics', North-Holland Publishing Company, pp. 165–275.

Hofmann, E. and Kuhlmann, H. C. (2011), 'Particle accumulation on periodic orbits by repeated free surface collisions', *Phys. Fluids* **23**, 072106 (14pp).

Hu, H. and Larson, R. G. (2002), 'Evaporation of a sessile droplet on a substrate', *J. Phys. Chem. B* **106**, 1334–1344.

Hu, H. and Larson, R. G. (2006), 'Marangoni effect reverses coffee-ring depositions', *J. Phys. Chem. B* **110**, 7090–7094.

Ishii, K., Ota, C. and Adachi, S. (2012), 'Streamlines near a closed curve and chaotic streamlines in steady cavity flows', *Proc. IUTAM* **5**, 173–186. IUTAM Symposium on 50 Years of Chaos: Applied and Theoretical.

Kalita, J. C., Biswas, S. and Panda, S. (2018), 'Finiteness of corner vortices', *Z. Angew. Math. Phys.* **69**, 37 (15pp).

Kalová, J. and Mareš, R. (2018), 'The temperature dependence of the surface tension of water', *AIP Conf. Proc.* **2047**, 020007 (7pp).

Karapetsas, G., Matar, O. K., Valluri, P. and Sefiane, K. (2012), 'Convective rolls and hydrothermal waves in evaporating sessile drops', *Langmuir* **28**, 11433–11439.

Karbalaei, A., Kumar, R. and Cho, H. J. (2016), 'Thermocapillarity in microfluidics–a review', *Micromachines* **7**, 13 (41pp).

Kelly-Zion, P. L., Pursell, C. J., Wassom, G. N., Mandelkorn, B. V. and Nkinthorn, C. (2018), 'Correlation for sessile drop evaporation over a wide range of drop volatilities, ambient gases and pressures', *Int. J. Heat Mass Transf.* **118**, 355–367.

Kleiber, M. and Joh, R. (2010), Liquids and gases, *in* V. D. Ingenieure, ed., 'VDI Heat Atlas', second edn, Springer Berlin, Heidelberg, chapter D3.1, pp. 301–393.

Kolmogorov, A. N. (1954*a*), The general theory of dynamical systems and classical mechanics, *in* 'Proceedings of the 1954 Congress in Mathematics', North-Holland, pp. 315–333.

Kolmogorov, A. N. (1954*b*), 'On conservation of conditionally periodic motions under small perturbations of the Hamiltonian', *Dokl. Akad. Nauk. SSSR* **98**, 527–530.

Kopriva, D. A. (2009), *Implementing spectral methods for partial differential equations: Algorithms for scientists and engineers*, Springer Science & Business Media.

Koschmieder, E. L. and Prahl, S. A. (1990), 'Surface-tension-driven Bénard convection in small containers', *J. Fluid Mech.* **215**, 571–583.

Kuhlmann, H. C. (1996), Thermokapillare Konvektion in Modellsystemen der Kristallzucht, Habilitation thesis, Bremen, Germany.

Kuhlmann, H. C. (1999), *Thermocapillary Convection in Models of Crystal Growth*, Vol. 152 of *Springer Tracts in Modern Physics*, Springer, Berlin, Heidelberg.

Kuhlmann, H. C. and Albensoeder, S. (2014), 'Stability of the steady three-dimensional lid-driven flow in a cube and the supercritical flow dynamics', *Phys. Fluids* **26**, 024104 (11pp).

Kuhlmann, H. C. and Muldoon, F. H. (2012), 'Particle-accumulation structures in periodic free-surface flows: Inertia versus surface collisions', *Phys. Rev. E* **85**, 046310 (5pp).

Kuhlmann, H. C. and Muldoon, F. H. (2013), 'On the different manifestations of particle accumulation structures (PAS) in thermocapillary flows', *Eur. Phys. J. Special Topics* **219**, 59–69.

Kuhlmann, H. C. and Nienhüser, C. (2002), 'Dynamic free-surface deformations in thermocapillary liquid bridges', *Fluid Dyn. Res.* **31**, 103–127.

Kuhlmann, H. C. and Rath, H. J. (1993), 'Hydrodynamic instabilities in cylindrical thermocapillary liquid bridges', *J. Fluid Mech.* **247**, 247–274.

Kuhlmann, H. C. and Romanò, F. (2018), *The Lid-Driven Cavity*, Vol. 50 of *Computational Methods in Applied Sciences*, Springer, Berlin, Heidelberg, pp. 233–309.

Kuhlmann, H. C. and Schoisswohl, U. (2010), 'Flow instabilities in thermocapillary-buoyant liquid pools', *J. Fluid Mech.* **644**, 509–535.

Kumar, M. and Bhardwaj, R. (2018), 'A combined computational and experimental investigation on evaporation of a sessile water droplet on a heated hydrophilic substrate', *Int. J. Heat Mass Transf.* **122**, 1223–1238.

Kumar, S., Medale, M. and Brutin, D. (2022), 'Numerical model for sessile drop evaporation on heated substrate under microgravity', *Int. J. Heat Mass Transf.* **195**, 123150 (14pp).

Laplace, P. S. (1806), Traité de mécanique céleste, *in* ‘Ouvres Complete’, Suppléments au Livre X, Gauthier-Villars.

Larson, R. G. (2017), ‘Twenty years of drying droplets’, *Nature* **550**, 466–467.

Lehoucq, R. B., Sorensen, D. C. and Yang, C. (1998), ‘ARPACK users’ guide: Solution of large scale eigenvalue problems with implicitly restarted Arnoldi methods’, *Softw. Environ. Tools* .

Leong, C. W. and Ottino, J. M. (1989), ‘Experiments on mixing due to chaotic advection in a cavity’, *J. Fluid Mech.* **209**, 463–499.

Levic, V. G. (1962), *Physicochemical hydrodynamics*, Prentice-Hall international series in the physical and chemical engineering sciences, second edn, Prentice-Hall, Englewood Cliffs, NJ.

Leypoldt, J., Kuhlmann, H. C. and Rath, H. J. (2000), ‘Three-dimensional numerical simulation of thermocapillary flows in cylindrical liquid bridges’, *J. Fluid Mech.* **414**, 285–314.

Li, T., Kar, A. and Kumar, R. (2019), ‘Marangoni circulation by UV light modulation on sessile drop for particle agglomeration’, *J. Fluid Mech.* **873**, 72–88.

Li, Y., Zhao, Z., Lam, M. L., Liu, W., Yeung, P. P., Chieng, C.-C. and Chen, T.-H. (2015), ‘Hybridization-induced suppression of coffee ring effect for nucleic acid detection’, *Sens. Actuators B Chem.* **206**, 56–64.

Lian, H., Qi, L., Luo, J., Zhang, R. and Hu, K. (2020), ‘Uniform droplet printing of graphene micro-rings based on multiple droplets overwriting and coffee-ring effect’, *Appl. Surf. Sci.* **499**, 143826 (8pp).

Mengaldo, G., De Grazia, D., Moxey, D., Vincent, P. E. and Sherwin, S. J. (2015), ‘Dealiasing techniques for high-order spectral element methods on regular and irregular grids’, *J. Comput. Phys.* **299**, 56–81.

Meunier, P. and Villermaux, E. (2010), ‘The diffusive strip method for scalar mixing in two dimensions’, *J. Fluid Mech.* **662**, 134–172.

Moffatt, H. K. (1964), ‘Viscous and resistive eddies near a sharp corner’, *J. Fluid Mech.* **18**, 1–18.

Moffatt, H. K. (2019), ‘Singularities in fluid mechanics’, *Phys. Rev. Fluids* **4**, 110502 (11pp).

Möser, J. (1962), ‘On invariant curves of area-preserving mappings of an annulus’, *Nachr. Akad. Wiss. Göttingen Math. Phys. Kl.* pp. 1–20.

Mukin, R. V. and Kuhlmann, H. C. (2013), ‘Topology of hydrothermal waves in liquid bridges and dissipative structures of transported particles’, *Phys. Rev. E* **88**, 053016 (20pp).

Muller, D. E. (1956), ‘A method for solving algebraic equations using an automatic computer’, *Math. Comput.* **10**, 208–215.

Nienhüser, C. and Kuhlmann, H. C. (2002), ‘Stability of thermocapillary flows in non-cylindrical liquid bridges’, *J. Fluid Mech.* **458**, 35–73.

Nitsche, J. (1971), ‘Über ein Variationsprinzip zur Lösung von Dirichlet-Problemen bei Verwendung von Teilräumen, die keinen Randbedingungen unterworfen sind’, *Abh. Math. Semin. Univ. Hambg.* **36**, 9–15.

O’Brien, V. (1975), ‘Unsteady cavity flows: Oscillatory flat box flows’, *J. Appl. Mech.* **42**, 557–563.

Ottino, J. M. (1989), *The Kinematics of Mixing: Stretching, Chaos, and Transport*, Cambridge Texts in Applied Mathematics, Cambridge University Press, Cambridge.

Ottino, J. M., Leong, C. W., Rising, H. and Swanson, P. D. (1988), ‘Morphological structures produced by mixing in chaotic flows’, *Nature* **333**, 419–425.

Park, J. and Moon, J. (2006), ‘Control of colloidal particle deposit patterns within picoliter droplets ejected by ink-jet printing’, *Langmuir* **22**, 3506–3513.

Pearson, J. R. A. (1958), ‘On convection cells induced by surface tension’, *J. Fluid Mech.* **4**, 489–500.

Perot, J. B. (1993), ‘An analysis of the fractional step method’, *J. Comput. Phys.* **108**, 51–58.

Petkovic, K., Metcalfe, G., Chen, H., Gao, Y., Best, M., Lester, D. and Zhu, Y. (2017), ‘Rapid detection of hendra virus antibodies: an integrated device with nanoparticle assay and chaotic micromixing’, *Lab Chip* **17**, 169–177.

Poumaëre, N. (2020), Numerical investigation of the effect of temporal symmetries on Lagrangian topology and emergence of chaotic advection in a two-dimensional lid-driven cavity, mathesis, École Centrale de Lyon.

Riedler, J. and Schneider, W. (1983), ‘Viscous flow in corner regions with a moving wall and leakage of fluid’, *Acta Mech.* **48**, 95–102.

Riley, R. J. and Neitzel, G. P. (1998), ‘Instability of thermocapillary–buoyancy convection in shallow layers. part1. characterization of steady and oscillatory instabilities’, *J. Fluid Mech.* **359**, 143–164.

Romanò, F., Kannan, P. K. and Kuhlmann, H. C. (2019), ‘Finite-size Lagrangian coherent structures in a two-sided lid-driven cavity’, *Phys. Rev. Fluids* **4**, 024302 (18pp).

Romanò, F. and Kuhlmann, H. C. (2019), 'Finite-size coherent structures in thermocapillary liquid bridges', *Int. J. Microgravity Sci. Appl.* **36**, 360201 (17pp).

Romanò, F., Türkbay, T. and Kuhlmann, H. C. (2020), 'Lagrangian chaos in steady three-dimensional lid-driven cavity flow', *Chaos* **30**, 073121 (27pp).

Romanò, F., Wu, H. and Kuhlmann, H. C. (2019), 'A generic mechanism for finite-size coherent particle structures', *Int. J. Multiphase Flow* **111**, 42–52.

Rüssmann, H. (1970), 'Über invariante Kurven differenzierbarer Abbildung eines Kreisringes', *Nachr. Akad. Wiss. Göttingen Math. Phys. Kl.* pp. 67–105.

Salgado Sánchez, P., Ezquerro, J. M., Fernández, J. and Rodríguez, J. (2020), 'Thermocapillary effects during the melting of phase change materials in microgravity: Heat transport enhancement', *Int. J. Heat Mass Transf.* **163**, 120478 (13pp).

Schatz, M. F. and Neitzel, G. P. (2001), 'Experiments on thermocapillary instabilities', *Annu. Rev. Fluid Mech.* **33**, 93–127.

Schatz, M. F., VanHook, S. J., McCormick, W. D., Swift, J. B. and Swinney, H. L. (1995), 'Onset of surface-tension-driven Bénard convection', *Phys. Rev. Lett.* **75**, 1938–1941.

Schneider, W. (2013), Surfaces as non-autonomous thermodynamic systems, *in* M. Pilotelli and G. P. Beretta, eds, '12th Joint European Thermodynamics Conference', Snoopy, pp. 178–185.

Schneider, W. (2015), 'How to deal with negative surface heat capacities', *Eur. Phys. J. Special Topics* **224**, 447–458.

Schwabe, D., Möller, U. and Schneider, J. (1992), 'Instabilities of shallow dynamic thermocapillary liquid layers', *Phys. Fluids A* **4**, 2368–2381.

Schwabe, D., Tanaka, S., Mizev, A. and Kawamura, H. (2006), 'Particle accumulation structures in time-dependent thermocapillary flow in a liquid bridge under microgravity conditions', *Microgravity Sci. Technol.* **18**, 117–127.

Sefiane, K. (2010), 'On the formation of regular patterns from drying droplets and their potential use for bio-medical applications', *J. Bionic Eng.* **7**, S82–S93.

Sefiane, K., Moffat, J. R., Matar, O. K. and Craster, R. V. (2008), 'Self-excited hydrothermal waves in evaporating sessile drops', *Appl. Phys. Lett.* **93**, 074103 (3pp).

Sefiane, K., Steinchen, A. and Moffat, R. (2010), 'On hydrothermal waves observed during evaporation of sessile droplets', *Colloids Surf. A: Physicochem. Eng. Asp.* **365**, 95–108.

Semenov, S., Carle, F., Medale, M. and Brutin, D. (2017), 'Boundary conditions for a one-sided numerical model of evaporative instabilities in sessile drops of ethanol on heated substrates', *Phys. Rev. E* **96**, 063113 (15pp).

Shankar, P. N. and Deshpande, M. D. (2000), 'Fluid mechanics in the driven cavity', *Annu. Rev. Fluid Mech.* **32**, 93–136.

Shi, W.-Y., Tang, K.-Y., Ma, J.-N., Jia, Y.-W., Li, H.-M. and Feng, L. (2017), 'Marangoni convection instability in a sessile droplet with low volatility on heated substrate', *Int. J. Therm. Sci.* **117**, 274–286.

Smith, M. K. and Davis, S. H. (1983), 'Instabilities of dynamic thermocapillary liquid layers. Part 1. Convective instabilities', *J. Fluid Mech.* **132**, 119–144.

Speetjens, M., Metcalfe, G. and Rudman, M. (2021), 'Lagrangian transport and chaotic advection in three-dimensional laminar flows', *Appl. Mech. Rev.* **73**, 030801 (55pp).

Stojanović, M., Romanò, F. and Kuhlmann, H. C. (2022), 'Stability of thermocapillary flow in liquid bridges fully coupled to the gas phase', *J. Fluid Mech.* **949**, A5 (51pp).

Takakusagi, T. and Ueno, I. (2017), 'Flow patterns induced by the thermocapillary effect and resultant structures of suspended particles in a hanging droplet', *Langmuir* **33**, 13197–13206.

Takasaki, S., Ogawara, K. and Iida, S. (1994), 'A study on chaotic mixing in 2D cavity flows : Effects of Reynolds number and amplitude of lid velocity', *JSME Int. J. Ser. B* **37**, 237–241.

Virtanen, P., Gommers, R., Oliphant, T. E., Haberland, M., Reddy, T., Cournapeau, D., Burovski, E., Peterson, P., Weckesser, W., Bright, J., van der Walt, S. J., Brett, M., Wilson, J., Millman, K. J., Mayorov, N., Nelson, A. R. J., Jones, E., Kern, R., Larson, E., Carey, C. J., Polat, İ., Feng, Y., Moore, E. W., VanderPlas, J., Laxalde, D., Perktold, J., Cimrman, R., Henriksen, I., Quintero, E. A., Harris, C. R., Archibald, A. M., Ribeiro, A. H., Pedregosa, F., van Mulbregt, P. and SciPy 1.0 Contributors (2020), 'SciPy 1.0: Fundamental Algorithms for Scientific Computing in Python', *Nat. Methods* **17**, 261–272.

Vogel, M. J., Hirsa, A. H. and Lopez, J. M. (2003), 'Spatio-temporal dynamics of a periodically driven cavity flow', *J. Fluid Mech.* **478**, 197–226.

Wang, Q., Zhang, X., Zhang, Y. and Yi, Q. (2014), AUGEM: Automatically generate high performance dense linear algebra kernels on x86 CPUs, *in* W. Gropp and S. Matsuoka, eds, 'SC '13: Proceedings of the International Conference for High Performance Computing, Networking, Storage and Analysis', ACM, p. 25 (12pp).

Wanschura, M., Shevtsova, V. M., Kuhlmann, H. C. and Rath, H. J. (1995), 'Convective instability mechanisms in thermocapillary liquid bridges', *Phys. Fluids* **7**, 912–925.

Watanabe, T., Takakusagi, T., Ueno, I., Kawamura, H., Nishino, K., Ohnishi, M., Sakurai, M. and Matsumoto, S. (2018), 'Terrestrial and microgravity experiments on onset of oscillatory thermocapillary-driven convection in hanging droplets', *Int. J. Heat Mass Transf.* **123**, 945–956.

Wu, H., Romanò, F. and Kuhlmann, H. C. (2021), 'Attractors for the motion of a finite-size particle in a two-sided lid-driven cavity', *J. Fluid Mech.* **906**, A4 (50pp).

Xu, J.-J. and Davis, S. H. (1984), 'Convective thermocapillary instabilities in liquid bridges', *Phys. Fluids* **27**, 1102–1107.

Young, T. (1805), 'An essay on the cohesion of fluids', *Phil. Trans. Roy. Soc. London* **95**, 65.

Zang, D., Tarafdar, S., Tarasevich, Y. Y., Choudhury, M. D. and Dutta, T. (2019), 'Evaporation of a droplet: From physics to applications', *Phys. Rep.* **804**, 1–56.

Zhu, J., Holmedal, L. E., Wang, H. and Myrhaug, D. (2020), 'Vortex dynamics and flow patterns in a two-dimensional oscillatory lid-driven rectangular cavity', *Eur. J. Mech. B Fluids* **79**, 255–269.

Zhu, J.-L. and Shi, W.-Y. (2019), 'Longitudinal roll patterns of Marangoni instability in an easily volatile sessile droplet evaporating at constant contact angle mode', *Int. J. Heat Mass Transf.* **134**, 1283–1291.

Zhu, J.-L. and Shi, W.-Y. (2021), 'Hydrothermal waves in sessile droplets evaporating at a constant contact angle mode', *Int. J. Heat Mass Transf.* **172**, 121131 (13pp).